

AN ABSTRACT OF THE THESIS OF

John T. Ebner for the degree of Doctor of Philosophy in
Electrical and Computer Engineering presented on November 3, 1989.

Title: Growth, Fabrication and Modeling of Pseudomorphic Laser Diodes

Redacted for privacy

Abstract approved: _____

This thesis reports on the crystal growth, fabrication, modeling and performance of Graded Index-Separate Confinement Heterostructure laser diodes which contain pseudomorphic InGaAs as the active region material. Laser epitaxial layers were grown with different indium mole-fractions, and a constant InGaAs layer thickness of 10 nm, on both sides of the theoretical Matthews-Blakeslee limit for dislocation formation. Devices fabricated from these epitaxial layers demonstrated room temperature lasing for the 0.0, 0.10 and 0.20 indium mole-fractions, only spontaneous emission for the 0.30 mole-fraction and no emission at all for the 0.40 mole-fraction.

A model was constructed which calculates the spectral gain of quantum well laser diode epitaxial structures of arbitrary design, including the band perturbations due to the inherent strain in the pseudomorphic InGaAs. The transition energy of highest gain, calculated as a function of indium mole-fraction, matches that measured from the fabricated devices. Extension of the model to high indium concentration structures predicts that device operation at 1.3 micron wavelength should be achievable in this system.

Growth, Fabrication and Modeling of Pseudomorphic Laser Diodes

by
John Ebner

A THESIS
submitted to
Oregon State University

in partial fulfillment of
the degree requirements for the
degree of
Doctor of Philosophy

Completed November 3, 1989

Commencement June 1990

APPROVED:

Redacted for privacy

Professor of Electrical and Computer Engineering in charge of major

Redacted for privacy

Head of Department, Electrical and Computer Engineering

Redacted for privacy

Dean of the Graduate School

Date thesis is presented November 3, 1989

Typed by researcher for John Ebner

ACKNOWLEDGMENT

I would like to thank a number of people who have helped me along the path towards this degree. The friendship of those who have had to endure me on a daily basis, in particular, Leon Ungier and soon to be Doctors-Jenifer Lary and Hyung Mo Yoo, is cherished. The support of Dr. John Arthur which has allowed me to pursue my own interests is also recognized as is the time spent in discussion with Dr. Stephen Goodnick and Dr. Thomas Plant. The support, both financial and moral, of J. Prasad and Jeff Goll, of Textronix, is also gratefully acknowledged.

My ability to complete this work was in large part due to the patience and understanding of my family. My parents who were subject to my frustration long distance and to Amanda who was subject to it in person. Thank-you all for your help along the way.

TABLE OF CONTENTS

1. Introduction	1
2. Review of the Pertinent Literature	5
2.a. Laser Diode Operation	5
2.b. MBE Growth and Properties of Pseudomorphic InGaAs	9
2.c. Previous Related Work on Laser Diodes	26
3. Experimental Technique	29
3.a. Growth of the Laser Epitaxial Layers	29
3.b. Device Fabrication	39
3.c. Packaging and Test	47
4. Experimental Results	52
4.a. Measurements from the Epitaxial Layers	52
4.b. Measurements of Device Performance	52
5. Gain Spectra Model	64
5.a. Derivation of the Spectral Gain Expression	64
5.b. Design of the Program	76
6. Discussion	87
6.a. Characterization of the Epitaxial Layers	87
6.b. Device Performance	87
6.c. Comparison of Modeled to Fabricated Devices	97
6.d. Model Predictions	104
7. Summary, Conclusions and Suggestions	109
7.a. Summary	109
7.b. Conclusions	110
7.c. Suggestions	112
Bibliography	114
Appendix	
A. Gain Spectra Program	119

LIST OF FIGURES

		<u>Page</u>
2.1	Generic GRIN-SCH epitaxial layer structure.	8
2.2	Schematic of the surface lattice constant boundary condition forced upon a pseudomorphic film.	11
2.3	Critical thickness curve of InGaAs grown on GaAs.	14
2.4	Experimental verification of the critical thickness curve, from Reference [8].	15
2.5	Schematic band structure for an unstrained and strained material.	20
3.1	Diagram of the p-InGaAs GRIN-SCH epitaxial layers grown for this work.	30
3.2	Critical thickness curve with the indium concentrations and quantum well widths of the fabricated devices marked.	31
3.3	Simulated composition variation with distance for the 0.20 mole-fraction laser structure grown in this work.	35
3.4	Diagram of the epitaxial layer structures grown for this work including the substrate temperature history,	38
3.5	Reproductions of the mask set used in the fabrication of the laser diodes.	42 43
3.6	Cross-sectional diagram of the fabricated laser diode.	48
3.7	Photograph of the bonded devices.	50
3.8	Photograph of the mounted devices in the heatsink.	51
4.1	Diagram of the epitaxial structure grown to test the critical thickness relationship.	53
4.2	Photoluminescence spectra from the critical thickness test structure.	54
4.3	Photoluminescence spectra from the actual laser epitaxial layers after removal of the cap layer.	55
4.4	Current-voltage characteristic of the 0.0 mole-fraction indium laser diode.	56
4.5	Light output-current curve for typical 0.0, 0.1 and 0.2 mole-fraction indium devices.	57

LIST OF FIGURES

		<u>Page</u>
4.6	Spectral output from one of the 0.0 indium mole-fraction devices.	59
4.7	Spectral output from one of the 0.10 indium mole-fraction devices.	60
4.8	Spectral output from one of the 0.20 indium mole-fraction devices.	61
4.9	Spectral output from one of the 0.30 indium mole-fraction devices.	62
4.10	Far field pattern of the 0.0 mole-fraction indium laser various bias currents.	63
5.1	Constant energy surface of a quantum well sub-band.	68
5.2	Coordinate system defining an arbitrary \bar{K}	70
5.3	Cylindrical volume element used in the integration over K_{xy} .	73
5.4	Composition profile for the 0.20 mole-fraction indium GRIN-SCH laser.	78
5.5	Relative band alignments for the GaAs/InGaAs system.	81
5.6	Band potentials derived for a 100 Å, $\text{In}_{.2}\text{Ga}_{.8}\text{As}$ GRIN-SCH laser structure.	82
5.7	Envelope function of the first conduction sub-band.	83
5.8	Calculated gain spectra for a 100 Å $\text{In}_{.2}\text{Ga}_{.8}\text{As}$ GRIN-SCH laser diode.	85
6.1	Photographs of the spontaneous emission from the active region of one of the 0.10 mole-fraction devices (a), and one of the 0.20 mole-fraction devices (b).	91
6.2	Extracted net gain spectra as a function of photon energy for one of the 0.0 mole-fraction devices.	94
6.3	Extracted net gain spectra as a function of photon energy for one of the 0.10 mole-fraction devices.	95

LIST OF FIGURES

		<u>Page</u>
6.4	Extracted net gain spectra as a function of photon energy for one of the 0.20 mole-fraction devices.	96
6.5	Calculated material gain and measured net cavity gain for the 0.0 mole-fraction indium device.	99
6.6	Comparison of the calculated material transparency energy and the measured net cavity gain as a function of indium mole-fraction.	100
6.7	Sensitivity of the peak material gain photon energy with carrier density.	102
6.8	Sensitivity of the material transparency energy with quantum well width.	103
6.9	Critical thickness curve with the modeled quantum well values marked on it.	105
6.10	Material transparency wavelength for structures modeled along the critical thickness curve.	106
6.11	Transparency carrier density for structures modeled along the critical thickness curve.	107

LIST OF TABLES

		<u>Page</u>
2.1	Carrier masses of the heavy and light hole valence bands in the large strain limit.	24
2.2	Dipole moments for transitions from the conduction band to the various valence bands in pm-InGaAs.	25
3.1	Purity and vendor of the MBE source materials used.	32
3.2	Substrate material specifications.	33
6.1	Threshold currents of different laser diodes.	88

Growth, Fabrication and Modeling of Pseudomorphic Laser Diodes

1. Introduction

Semiconductor injection lasers are finding increasing application, from telephone communication systems to laser printers and compact disk players. This increase in utilization is driven by the small size, high quantum efficiency, minimal power supply requirement and high reliability of currently available devices. The improvements in these characteristics have come about through increased understanding of device operation, processing and epitaxial growth. In particular, advances in the knowledge of epitaxial growth processes and their application to the production of crystalline films optimized for laser diode devices have been key to this progress.

The two most prevalent material systems from which laser diodes are made are GaAs/AlGaAs and InGaAs/InP. The GaAs/AlGaAs system has an unique advantage which arises from the close match of lattice constants between the two parent binary compounds, viz., 5.966 angstroms for GaAs and 5.965 angstroms for AlAs. This lattice match condition ideally allows growth of an arbitrary thickness of material, throughout the whole ternary composition range, without the introduction of defects (such as dislocations) which would adversely affect device performance.

InGaAs films are not lattice matched with InP (the substrate on which they are typically grown for laser diode applications) over the whole range of indium to gallium mole-fraction. The lattice

constant of this alloy changes as the ratio of indium to gallium is varied. The crystal growth therefore is complicated by the necessity to produce only those compositions which have the same lattice constant as InP or device performance could be degraded. The ternary InGaAs composition which matches the InP substrate lattice constant is $\text{In}_{.53}\text{Ga}_{.47}\text{As}$. The indium mole-fraction of this film needs to be held to within 0.1% of the lattice match value to achieve optical quality material[1] which is extremely difficult to accomplish over reasonable substrate areas, viz., 1 cm².

Laser operation in the GaAs/AlGaAs system has been demonstrated from the GaAs band gap, 850 nm[2], to near the direct-to-indirect transition in the AlGaAs system, 690 nm[3]. This covers a range from the near infra-red into the red region of the visible spectrum. The availability of high quality material, due to the inherent lattice match in this system, makes this the most studied material system for diode lasers. InGaAs devices operate at wavelengths farther in the infra-red than those made in the GaAs/AlGaAs system, ranging from 1300 nm to 1600 nm[2]. This range overlaps the desired wavelengths of optical sources and detectors for fiber optic communications, 1550 nm and 1300 nm.

There is a gap between the wavelength regions in which devices made in these two material systems have demonstrated lasing (880 nm to 680 nm for GaAs/AlGaAs, and 1600 nm to 1300 nm for InGaAs/InP). It is in this region, 880 nm to 1300 nm, that the devices described in this thesis operate.

The strategy used to achieve diode laser operation in this wavelength window was to violate the constraint that the entire

epitaxial film be lattice matched to the substrate. It has been demonstrated that epitaxial films whose lattice constant does not match that of the substrate can be constructed with low defect density if they are extremely thin[4],[5]. Grown in this manner the film remains structurally coherent with the substrate; the lattice constant of the film adjusts in the plane of growth to match that of the substrate. This adjustment is accomplished by elastic deformation of the film. The substrate applies a stress to the film forcing it to distort, i.e., become strained, in response. Epitaxial layers of this type are called "coherently strained" or "pseudomorphic".

The addition of indium to the active region of an otherwise lattice matched GaAs/AlGaAs laser diode epitaxial layer could accomplish laser operation in the desired wavelength region. InAs has a smaller band gap (0.36 eV) than GaAs (1.41 eV) and the band gap of the ternary InGaAs varies monotonically between the two. Laser operation in the desired wavelength window is therefore possible by the incorporation of a low indium concentration InGaAs alloy as the active region of a GaAs/AlGaAs diode laser[6],[7]. InAs has a larger lattice constant (6.058 Å) than GaAs (5.653 Å) so pseudomorphic InGaAs grown on GaAs (pm-InGaAs) is elastically strained under an intense biaxial compressive stress, if it remains coherent with the substrate, i.e., dislocation free.

There are fundamental limits to the thickness which these films can be grown such that they remain coherent with the substrate. These constraints arise from the excess energy associated with the elastic deformation in the pseudomorphic film. In low indium mole-fraction InGaAs the limiting thickness is large enough such that the

films are useful for device applications. As an example, the maximum thickness that a 30% mole-fraction indium InGaAs film can be grown is approximately 10 nm[8]. This is a reasonable thickness for the active region of a diode laser and would yield emission at a wavelength close to 1000 nm. A detailed discussion of the limits to which pm-InGaAs layers can be grown on GaAs substrates is included in Chapter 2.

This thesis describes device modeling, crystal growth, construction and performance of diode lasers, grown on GaAs substrates by Molecular Beam Epitaxy (MBE), containing pm-InGaAs as the active media. A number of devices with differing indium mole-fractions in the active region, but otherwise identical, were grown, fabricated and tested as described in Chapters 3 and 4. The effect of exceeding the maximum indium concentration (critical concentration) allowable in a coherent film, at a fixed layer thickness, was investigated by intentionally growing layers over this limit. The spectral performance of the device structures fabricated was predicted via calculation of the gain spectra, as a function of carrier density, for various epitaxial layer designs as described in Chapter 5. The strain inherent in the pm-InGaAs has impact on the band structure of that material, which in turn alters the device performance. These perturbations are predicted to affect the laser wavelength and the threshold current. Comparison of the predicted and the actual device performance is included in Chapter 6.

2. Review of Pertinent Literature

The previous literature relevant to this work can be divided into three categories:

- a. Laser diode operation,
- b. MBE growth of pm-InGaAs and its properties,
- c. Previous related work on laser diodes.

The theoretical basis for laser diode operation is fairly well established and will be summarized. The specifics of the operation of the laser structure studied in this work will be described in detail. Pseudomorphic-InGaAs is a topic of current research interest as InGaAs/GaAs is a convenient system to study strained films. Current understanding of the growth of this material and its properties will be reviewed. The effect of strain on the performance of diode lasers is not well studied but is a topic of increasing interest as strained layer lasers show commercial application. Other literature describing studies of strain effects on laser diodes will also be described.

2.a. Laser Diode Operation

To achieve laser action in any material a population inversion needs to be created. To accomplish this in a semiconductor, energy is pumped into the system in such a way that the valence band is filled with holes and the conduction band is filled with electrons. The alteration in carrier density from equilibrium changes the strength of the interband optical interaction between the valence and conduction bands and photons whose energy is above that of the band gap. The optical absorption of the material (a measure of the interaction strength) near the band edge decreases as excess carrier density increases. Further increase in carrier density creates a

situation in which the optical absorption of the material, near in energy to the band edge, changes sign. The material then exhibits optical gain, instead of loss, at energies where the majority of the excess carriers thermalize. When population inversion is reached, the number of carriers in the bands is so large that the quasi-Fermi levels, which describe the electron and hole densities, are separated in energy by more than the band gap of the material. This is the Bernard-Durauffourg condition for population inversion in a semiconductor[9].

The excess carrier density required to invert the bands of a diode laser is extremely high, typically greater than 10^{18} carriers per cm^3 (both electrons and holes). The ability to achieve this excess carrier density is critically dependent upon the quality of the epitaxial material from which the junction is formed. The competitive non-radiative recombination pathways in the active region of the junction have to be minimized. If there are a large number of energy levels deep within the band gap, as could arise from improper crystal growth, then the carrier density in the active region could saturate (due to non-radiative recombination through these levels) before the bands are inverted. The III-V crystal growth technologies currently available have allowed the fabrication of laser epitaxial layers with negligible non-radiative recombination[10].

The ability to engineer epitaxial layers on a microscopic scale has been the key to improving laser diode performance to the high levels achieved to date. The double heterostructure (DH) laser employs two hetero-interfaces (abrupt interfaces between dissimilar

semiconductor materials) surrounding the active region to increase the carrier and optical confinement[2],[11]. This structure was the first laser design to operate for reasonable periods of time without cryogenic cooling[2]. The epitaxial layers for these first room temperature devices were grown by Liquid Phase Epitaxy (LPE). The maturation of crystal growth technologies such as MBE and MOCVD, which allow greater compositional control than LPE, have permitted more complicated epitaxial layer designs. One variant of the DH laser, the Graded Index-Separate Confinement Heterostructure (GRIN-SCH) laser, has been studied extensively.

The GRIN-SCH structure was proposed simultaneously by Tsang at A.T.&T. Bell Labs[12] and by Kameset, et. al., at Rockwell, Inc.[13] as a design optimized to yield low threshold current densities. Inherent in the GRIN-SCH structure is an index of refraction variation which increases the light confinement in the active region and a band gap discontinuity which separately confines the carriers. Figure 2.1 shows a diagram of a typical GRIN-SCH epitaxial layer structure. The carriers are localized in the narrow GaAs region at the center due to the lower energy of the GaAs conduction (valence) band states as compared to the AlGaAs conduction (valence) band states. This layer is often called a "quantum well" since the proximity of the larger band gap AlGaAs layers surrounding it perturb the energy levels of the electrons and holes in the GaAs due to quantum mechanical effects.

The compositionally graded AlGaAs layers form an optical waveguide which acts to localize the light to the quantum well. The degree to which the light is squeezed into the GaAs is measured by the optical confinement factor, Γ . Gamma in a GRIN-SCH laser is increased

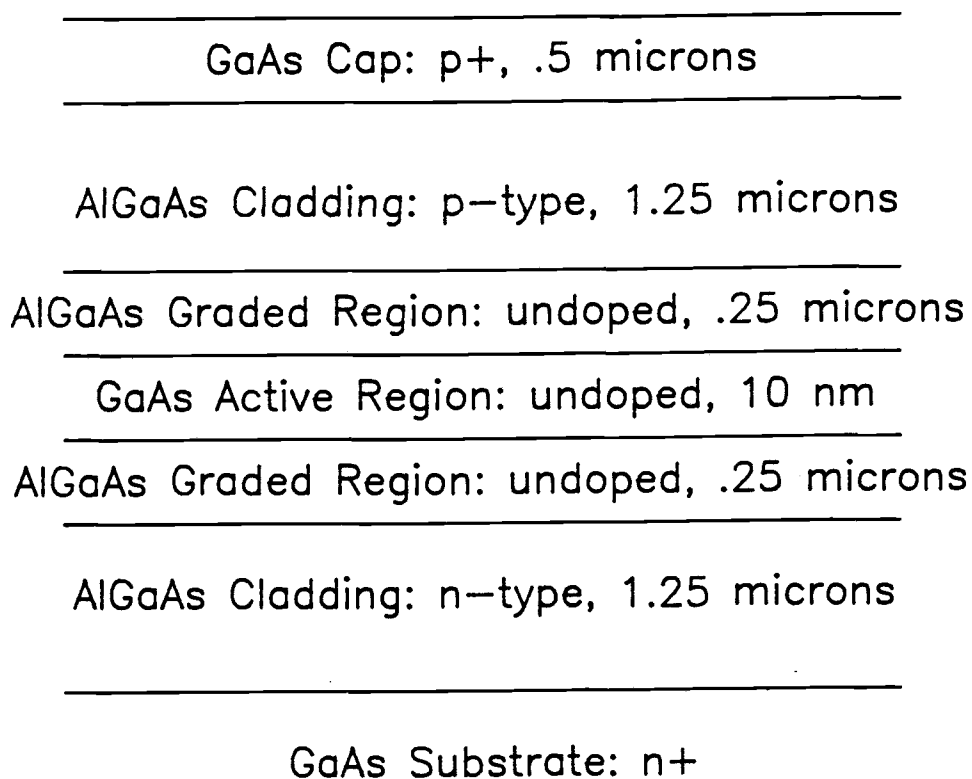


Figure 2.1: GRIN-SCH laser epitaxial layer structure. Light is confined by the waveguide formed by the graded layers while the carriers are confined by the quantum well. The layer thicknesses are typical values.

over that in a DH laser. The waveguide increases the light confinement in the active region and with it the interaction between the light and the carriers. This increases the modal gain of the device (defined as the fundamental gain of the material times the overlap of the carrier wavefunctions and photon density). This increase in the modal gain, along with other advantages which arise from quantum confinement of carriers in the narrow active region, decreases the threshold current density of the GRIN-SCH significantly below that of the DH laser design. GRIN-SCH laser epitaxial layers have been constructed into devices which yield threshold current densities lower than 50 A/cm²[14] while threshold current densities in DH lasers are typically 1000 A/cm²[2].

2.b. MBE Growth and Properties of Pseudomorphic InGaAs

The growth of InGaAs on GaAs is complicated by the difference in lattice constant that exists between the two materials. It has been shown that InGaAs can be grown coherently (with a one to one correspondence between bonds in the substrate and bonds in the film) on GaAs substrates if the thickness of the InGaAs is kept below a "critical thickness"[4],[15]. The condition of coherence between the substrate and the film is a prerequisite for the use of these films in laser diodes. Incoherence implies the formation of dislocations which are usually efficient non-radiative recombination centers[16] and hence reduce the light output.

The properties of pseudomorphic films are altered by the strain, which arises from the lattice constant difference between the film and the substrate, and the imposition of coherence at the interface. It is the intent of the following section to describe

problems associated with the growth of these strained films, as well as changes in the electronic and optical properties of these materials induced by the intrinsic strain.

At low indium concentrations the lattice constants of InGaAs and GaAs are virtually identical and the effects mentioned above are minimal. Likewise, at high indium concentrations the lattice constant difference is large (7% for InAs on GaAs) and the strain effects are large. Low indium concentration alloys do not have properties different enough from GaAs to warrant their use although they can be grown reasonably thick. High indium concentration alloys have properties dramatically different than GaAs but typically cannot be grown thick enough to be useful in a device. The intermediate region allows the growth of reasonable film thicknesses with properties significantly different than GaAs and this is the composition region explored for device applications[17],[18].

InGaAs, grown pseudomorphically on GaAs, is constrained such that its lattice constant in the plane of growth conforms to that of the surface of the substrate as shown schematically in Figure 2.2. This condition is identical to the application of biaxial compression to the InGaAs film; the stress is imposed internally by the substrate. Static equilibrium requires a balance of forces which results in an equivalent stress on the substrate imposed by the film. The thickness of the substrate is typically 400 to 500 microns compared to 0.01 microns for the film. This thickness difference results in an extremely small strain in the substrate (only that allowed by bowing of the substrate). In the analysis of pm-InGaAs grown on GaAs it is therefore commonly assumed that the only strain in the system is

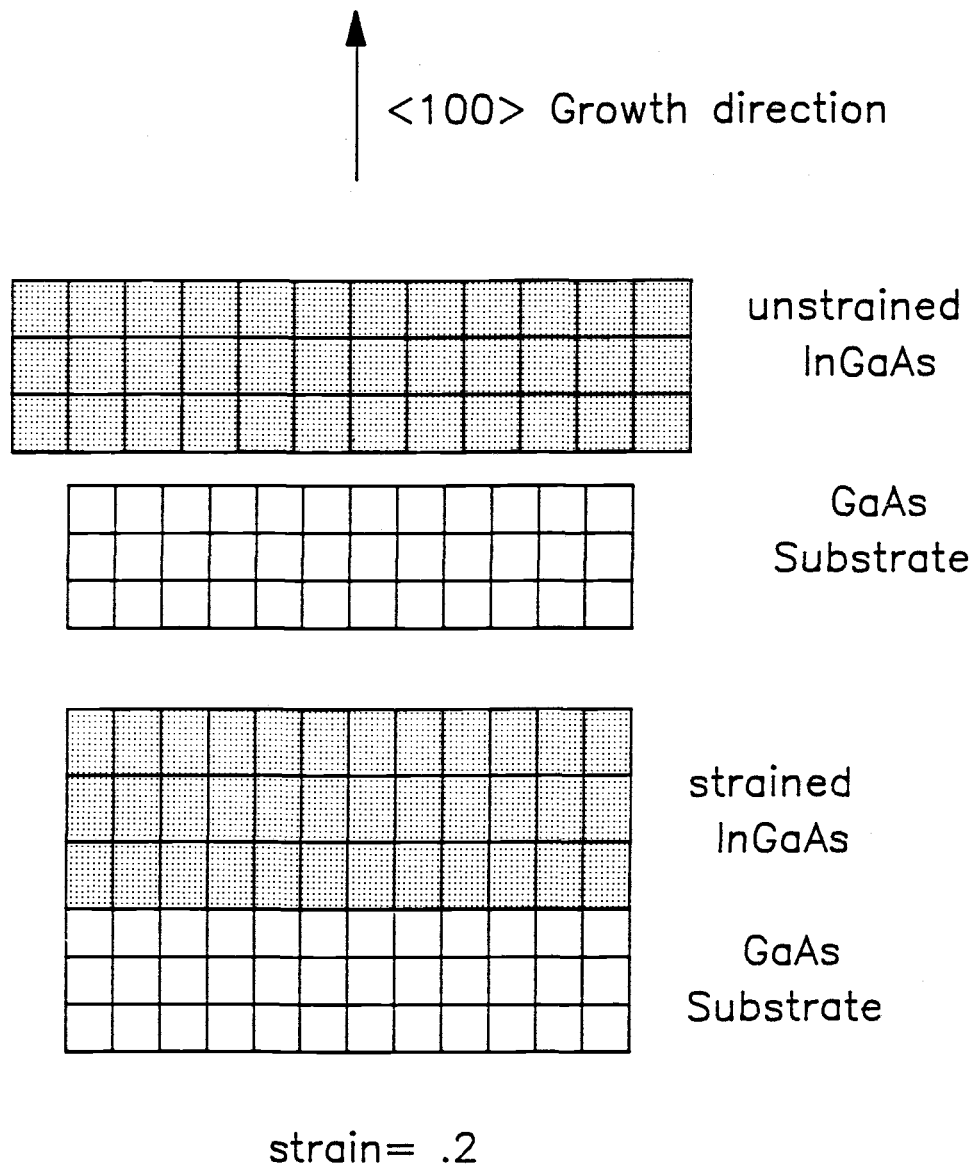


Figure 2.2: Schematic of the surface lattice constant boundary condition forced upon a pseudomorphic film, in side view. The upper diagram is representative of the free standing InGaAs and the lower diagram is representative of pm-InGaAs.

localized in the pm-InGaAs.

Biaxial compression of a film causes tetragonal distortion[19]. The lattice constant of the pseudomorphic film is constrained by the substrate in the two directions parallel with the substrate surface. The direction normal to the surface is unconstrained and the film expands in the this direction in response to the compression in the lateral directions. This expansion elongates the unit cell normal to the surface making it tetragonal rather than cubic. Alterations in the electronic properties of the film follow from changes in the physical shape of the unit cell. The distortion of the crystal structure breaks the symmetry of the crystal and the isotropy of the crystal properties. Changes in specific material properties important to laser performance will be discussed later in this section.

Strained films can be grown pseudomorphic with the substrate in only certain regions of composition and film thickness. As strained material is deposited forces associated with the elastic deformation of the film increase. At a certain thickness these forces reach a magnitude such that stress relief, by the formation of an array of edge dislocations at the hetero-interface, is energetically favored to occur. These dislocations are parallel to the hetero-interface and are called "misfit dislocations" [4],[5]. Misfit dislocations introduce midgap states, into the active layer, which act as non-radiative recombination centers degrading the performance of devices requiring high excess carrier densities, such as lasers.

The maximum thickness which a pseudomorphic film can be grown before the formation of misfit dislocations is called the critical

thickness. One calculation of this maximum thickness as a function of indium mole-fraction, for the InGaAs/GaAs system, is shown in Figure 2.3. This curve was based on a theory by Matthews and Blakeslee which calculates the lateral force on a threading dislocation crossing the strained layer. As the layer thickness is increased, the force on the dislocation is increased and its propensity to glide along the interface is likewise increased. At the critical thickness the threading dislocation glides significant distances along the interface forming the misfit dislocation. Other theoretical work based upon an energetic balance of the crystal energy of a coherently strained film, as compared to one in which the strain is relieved via a dislocation network[20], predicts similar, but slightly different, limits. There is experimental confirmation of both these theoretical relationships and work in this area is on going.

The Matthews-Blakeslee relationship has been confirmed by a number of different experimental methods[8],[21]. One method was to measure the photoluminescence line-width of quantum well structures grown at various indium mole-fractions and film thicknesses[21]. The linewidth of the emission is narrow when the interface is coherent, and broader when the interface is dislocated. This is due to the fact that strain in the sample is relieved inhomogeneously by the dislocations, resulting in spatial variation in the band gap. This increases the width of the band edge emission from the film. Experimental confirmation of the theoretical critical thickness is shown in Figure 2.4. The solid line is the Matthews-Blakeslee critical thickness curve. The large data points are from InGaAs films

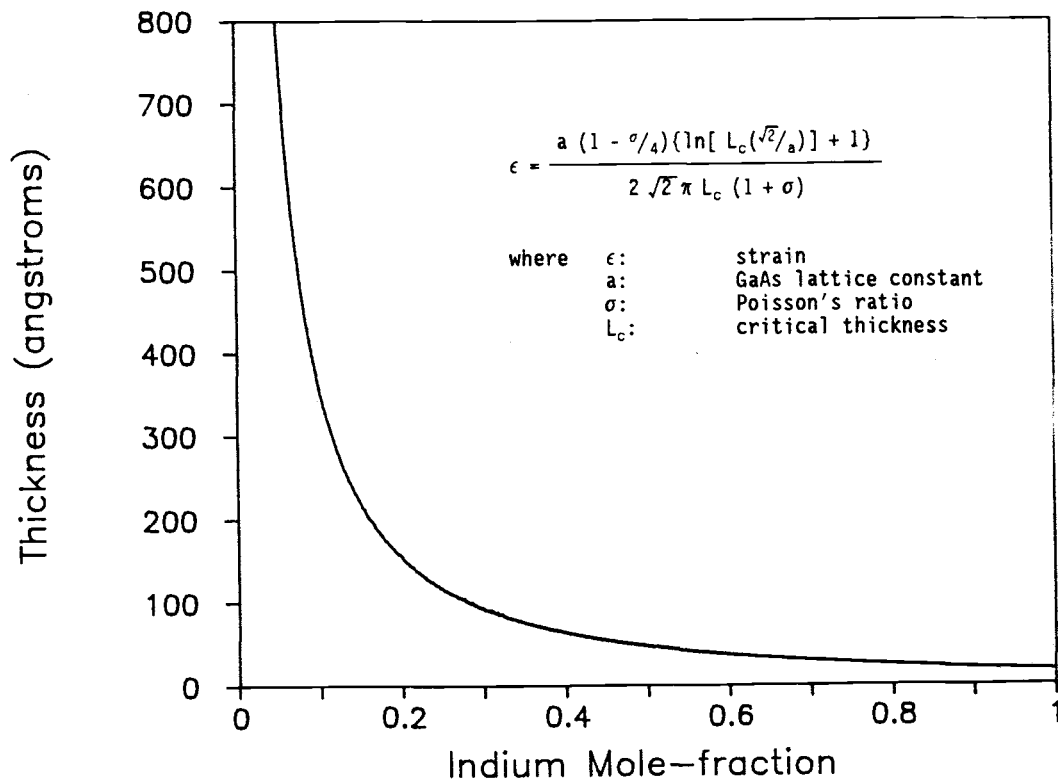


Figure 2.3: Critical thickness of InGaAs grown on GaAs as calculated via the theory of Matthews and Blakeslee. The equation from which the curve was extracted is shown in the inset.

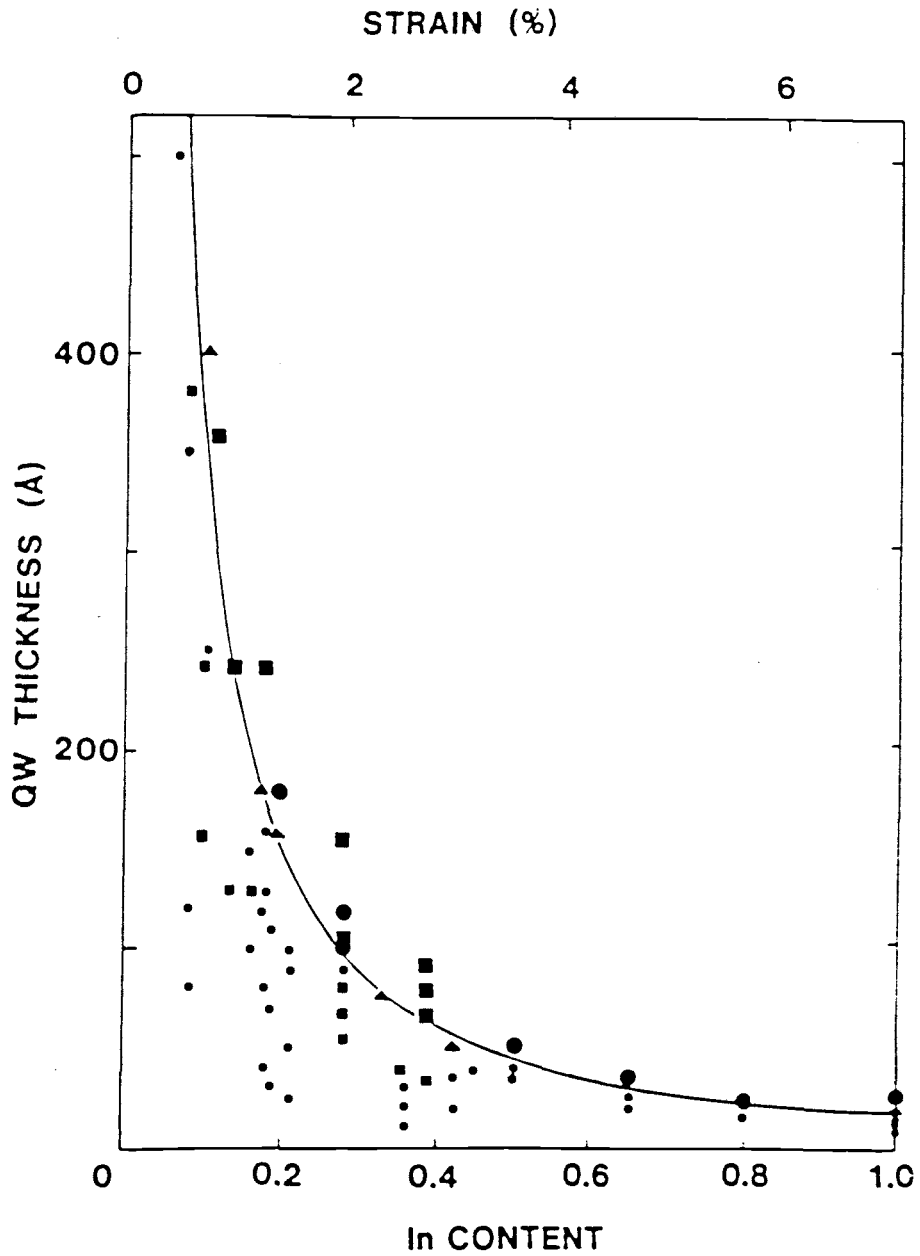


Figure 2.4: Experimental verification of the Matthews and Blakeslee critical thickness relationship via photoluminescence, from the work of Andersson[21].

grown on GaAs which displayed a large linewidth in low temperature photoluminescence (PL) and the small data points are from InGaAs films which displayed a narrow linewidth. The experimental match to the theory appears better than expected. There is uncertainty in the indium concentrations and well widths for the individual samples and the determination of narrow versus broad linewidth is subjective. None the less the agreement is good.

Optimization of the growth of pm-InGaAs as the active region of a laser diode has other complications. The substrate temperature is usually kept as high as possible during the growth of III,III-V ternary compounds such as InGaAs or AlGaAs. The high temperature is necessary in order to increase the diffusion of the more tightly bound Group III metal on the semiconductor surface during growth. If the surface mobility of this species is too low, the film will incorporate a high number of native defects. These native defects often give rise to mid-gap states and a high non-radiative recombination rate[22]. Material such as this would be unacceptable for the cladding regions of a laser diode as it would provide a mechanism for non-radiative carrier loss. An upper limit on substrate temperature during growth arises from re-evaporation of the weaker bound Group III metal. In the case of the growth of AlGaAs, gallium is the weaker bound species. For typical MBE growth conditions (arsenic stabilized surface, 1.0 micron/hour growth rate, Group III element flux limited) significant re-evaporation of gallium from the surface occurs at substrate temperatures in excess of 620° C. The temperature at which no gallium incorporates into the film under these conditions is approximately 710° C[23]. These temperatures are not invariant but functions of

arsenic overpressure and the magnitude of the metal fluxes. The quoted numbers are for an aluminum mole-fraction of around 0.30.

The $\text{Al}_{.5}\text{Ga}_{.5}\text{As}$ cladding layers in a GRIN-SCH laser are typically grown at a substrate temperature of 690°C [22]. At this temperature the amount of gallium which incorporates into the film is approximately 85% of the incident flux[23] (assuming all the incident flux initially adsorbes to the surface), i.e., 15% of the adsorbed gallium desorbes instead of incorporating into the crystal. An increase in substrate temperature would result in higher quality material, in terms of native defect density, however, there is a larger uncertainty in the film composition, due to the uncertainty in the measurement of the substrate temperature during growth, since the gallium desorption rate is a strong function of temperature.

The growth of InGaAs has similar constraints in terms of substrate temperature. In this case the more tightly bound Group III metal is gallium and the desorption of indium limits the maximum substrate temperature. InGaAs growth is typically done at a temperature of approximately 530°C , at which the desorption flux is 15% of the incident indium flux[24].

The complication in the growth of pm-InGaAs GRIN-SCH lasers arises from the difference between the temperature regimes for the growth of the different ternaries, AlGaAs and InGaAs. There is no overlap in the temperature windows in which these materials individually would be grown. An intermediate temperature of 600°C could be chosen but a significant number of deep levels would be incorporated in the AlGaAs and the indium concentration in the InGaAs would be extremely hard to control.

An alternative technique to deal with these disparate temperature regimes involves interrupting growth at the InGaAs/AlGaAs interface to change the substrate temperature. This is done by stopping the flux of the Group III metals to the surface but maintaining that of the Group V element. The incident Group V element flux inhibits the decomposition of crystal and should ideally allow the resumption of growth at a later time without affecting the quality of the epitaxial layer. This would be true if the background gas level in the system was non-existent and the Group V element flux was absolutely pure. Neither of these is true in reality. The time required to change the substrate temperature between the two optimal temperatures for the growth of InGaAs and AlGaAs is about 3 minutes due to the thermal mass of the wafer mount. In this time there is the possibility of the incorporation of impurities which might give rise to a higher non-radiative recombination rate. This could create a carrier loss mechanism worse than that associated with the low temperature growth of AlGaAs .

Pseudomorphic InGaAs has electrical and optical properties significantly different from those of unstrained InGaAs of the same composition. The perturbation on band structure due to strain has been investigated intensively in many different semiconductors[25], [26],[27]. It is the intent of this section to review the effects on the properties of the active region material due to the strain associated with biaxial compression.

There are three major strain perturbations to band structure which could affect laser performance:

1. Shifts of the fundamental band gap,

2. Changes in the masses of the various bands,
3. Perturbation of the optical transition matrix element.

The effect each of these has on the band structure, and consequently laser operation, will be discussed separately.

To understand the effects of strain on laser diode operation the E-K dispersion relation appropriate for the pm-InGaAs laser active region needs to be calculated accurately. Generation of this relation is complicated by effects, such as the spin-orbit[28] interaction, which make the energies of the various bands inter-related. The laser gain model, which will be outlined in Chapter 5, assumes a simple, parabolic description of the band structure. In the context of this simple model the band parameters of interest are: the energy positions of the bands, the carrier masses in the various directions, and the fundamental interaction strength. Each of these can be approximated separately without doing a complete band structure calculation around $K=0$.

The energy shifts of the bands at $K=0$ can be calculated from knowledge of the strain magnitude (a function of the indium concentration) and the appropriate band deformation potentials. Figure 2.5 shows a schematic band diagram, for an unstrained and a strained material, which outlines the band structure shifts. The conventions used in this thesis to describe the various directions in the semiconductor and the different valence bands are as follows:

z direction: {100} direction of epitaxial layer growth, also the direction of the electric field vector associated with the transverse magnetic (TM) polarization.

x or y directions: {100} directions along the crystal surface, also the direction of the electric field vector associated with the transverse electric (TE) polarization.

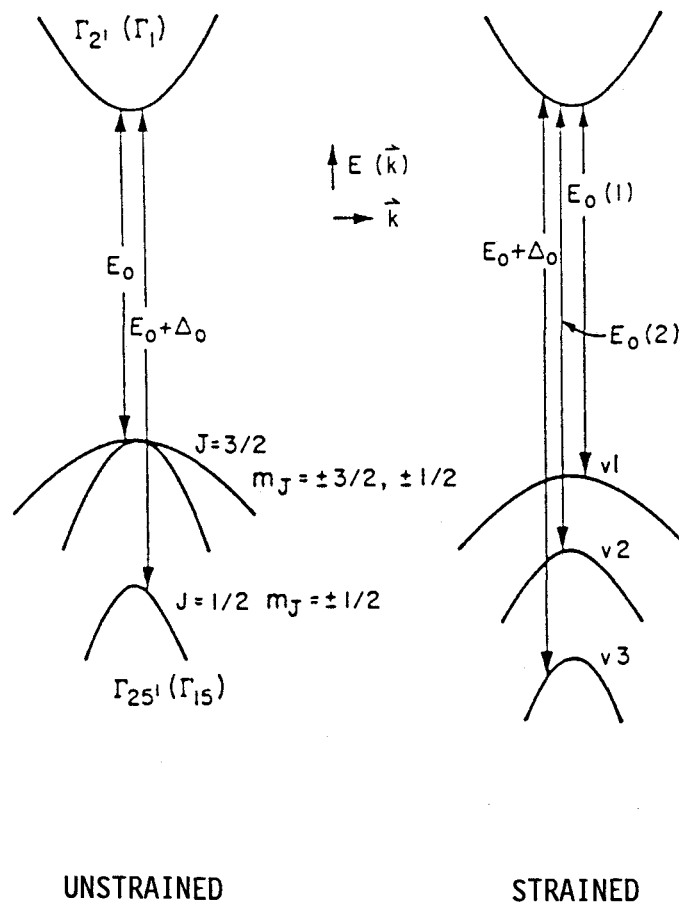


Figure 2.5: Schematic band structure for an unstrained and strained material. For the case of biaxial compression v_1 is the heavy hole band and v_2 is the light hole band, from the work of Pollak and Cardona[27].

"heavy hole" band: the $|3/2, 3/2\rangle$ valence band.

"light hole" band: the $|3/2, 1/2\rangle$ valence band.

The strain associated with biaxial compression can be decomposed into the superposition of hydrostatic and shear strain. The effect of each of these on the band energies is calculated separately. Hydrostatic compression widens the band gap but does not reduce symmetry as it acts equally in all three directions. Shear strain splits the valence band degeneracy. The net shifts in the band edge positions associated with these effects are [29], [25], [19]

$$\Delta E_o(1) = \left[-2a \left[\frac{C_{11} - C_{12}}{C_{11}} \right] + b \left[\frac{C_{11} + 2C_{12}}{C_{11}} \right] \right] \epsilon \quad (2.1a)$$

$$\Delta E_o(2) = \left[-2a \left[\frac{C_{11} - C_{12}}{C_{11}} \right] - b \left[\frac{C_{11} + 2C_{12}}{C_{11}} \right] \right] \epsilon \quad (2.1b)$$

where $E_o(1)$: heavy hole band
 $E_o(2)$: light hole band
 a : hydrostatic deformation potential
 b : shear deformation potential
 C_{ij} : elastic stiffness tensor components
 ϵ : strain

The strain is related to the InGaAs and the GaAs lattice constants via the relationship:

$$\epsilon = \frac{\Delta a}{a_{\text{InGaAs}}} \quad (2.2)$$

where Δa : $a_{\text{InGaAs}} - a_{\text{GaAs}}$
 a_{InGaAs} : unstrained InGaAs lattice constant
 a_{GaAs} : GaAs lattice constant

The strain tensor components for biaxial compression are

$$\epsilon_{xx} = \epsilon_{yy} = -\epsilon, \quad \epsilon_{zz} = \frac{2C_{12}}{C_{11}} \epsilon, \quad \epsilon_{xy} = \epsilon_{yz} = \epsilon_{zx} = 0 \quad (2.3)$$

The elastic constants are also dependent on the indium concentration which makes the energy shifts a non-linear function of indium mole-fraction.

The position of the spin-split band is also perturbed by the strain. This is of small consequence to laser operation as the spin-orbit splitting is large enough to eliminate any measurable effect on the spectral gain due to transitions to this band. A non-linear correction to the strain induced energy shift can also be calculated for the light hole band[25] but this is generally small compared to the linear shift.

Carrier mass changes associated with strain have been the subject of much investigation; in particular the effect uniaxial stress has on band properties has been studied intensively [25],[26],[27]. This work can be applied directly to intrinsically strained pseudomorphic materials because uniaxial stress applied in the z direction is analogous to biaxial stress in the x and y directions. For example, uniaxial tension in the [100] direction gives rise to an identical strain tensor as biaxial compression in the [010] and [001] directions.

The carrier mass variation of the various valence bands under

$$E_{3/2}(\bar{k}) = (A + 1/2B) |\bar{k}_{x,y}|^2 + (A - B) |\bar{k}_z|^2 + \epsilon_{shr} \quad (2.4a)$$

$$E_{1/2}(\bar{k}) = (A - 1/2B) |\bar{k}_{x,y}|^2 + (A + B) |\bar{k}_z|^2 - \epsilon_{shr} \quad (2.4b)$$

where A, B : inverse mass parameters of the unstrained material
 $\bar{k}_{x,y}$: in-plane wave vector
 \bar{k}_z : growth direction wave vector
 ϵ_{shr} : valence band splitting due to shear strain

uniaxial stress has been studied via cyclotron resonance[25],[26]. The expressions given in Equation 2.4 have been derived to describe the band dispersion relationships in the limit of large strain[25]. Definition of the large strain limit varies depending upon the magnitudes of the energies of interest in the valence band compared to the magnitude of the band splitting due to the shear strain. If the shear strain splitting is much larger than the energies of interest in the valence band then the bands can be assumed to be non-interacting at all energies of interest, and therefore in the large strain limit. If this is not the case the large strain limit assumption is invalid and the bands are interacting and therefore highly non-parabolic. In the large strain limit each valence band is described by ellipsoidal constant energy surfaces, one for each of the $J=3/2$ bands previously degenerate at $K=0$ [25].

The mass anisotropy in each of the valence bands, induced by the strain, can be approximated from the above equations. The mass in the z direction is necessary for calculation of the ground state energies of each of the valence sub-bands. The masses in the x and y directions are needed to calculate the two dimensional density of

states of each sub-band. The effective masses of the various valence bands, in the large strain limit, are given in Table 2.1. The carrier mass of the heavy hole band is much lighter in the x and y directions than in the z direction.

	x,y	z
Heavy Hole	$(A+1/2B)^{-1}$	$(A-B)^{-1}$
Light Hole	$(A-1/2B)^{-1}$	$(A+B)^{-1}$

Table 2.1: Carrier masses of the heavy and light hole valence bands, in various directions, in the large strain limit[25].

The third way that strain could influence the performance of a laser diode is by mixing the atomic wavefunctions which describe the valence band states. The strength of the interaction between a photon field and the semiconductor bands is given by the electric dipole moment of the transition (this is described in detail in Chapter 5). The dipole moment is determined, in part, by the wavefunctions of the electron and hole. The Bloch part of these wavefunctions is given by the Kane atomic wavefunctions for the various bands[28]. Strain perturbs the dipole moment by altering the nature of these Kane wavefunctions.

The resultant wavefunctions, mixed by strain in the [100] direction, have been calculated by Pollak and Cardona[27] and are

$$u_{hh} = \left| \begin{matrix} 3/2, & 3/2 \end{matrix} \right\rangle_{100} \quad (2.5a)$$

$$u_{lh} = \left| \begin{matrix} 3/2, & 1/2 \end{matrix} \right\rangle_{100} + 1/\sqrt{2} \alpha_0 \left| \begin{matrix} 1/2, & 1/2 \end{matrix} \right\rangle_{100} \quad (2.5b)$$

$$u_{so} = \left| \begin{matrix} 1/2, & 1/2 \end{matrix} \right\rangle_{100} - 1/\sqrt{2} \alpha_0 \left| \begin{matrix} 3/2, & 1/2 \end{matrix} \right\rangle_{100} \quad (2.5c)$$

where $\alpha_0 = (\text{valence band splitting/spin-orbit splitting})$

shown in Equation 2.5. The heavy hole wavefunction is unchanged by the strain so the transition dipole moment associated with this band is identical to that of unstrained material. The light hole band is mixed by interaction with the spin-orbit split band and the resultant dipole moment is a function of the magnitude of the strain. The dipole moments for TE and TM polarizations in pm-InGaAs are given in Table 2.2. The TE mode dipole moments are those of interest for most

	Heavy Hole	Light Hole
TE	$\frac{1}{2}P^2$	$(\frac{1}{6})(1-2\alpha_0)P^2$
TM	0	$(\frac{2}{3})(1+\alpha_0)P^2$

Table 2.2: The dipole moments for transitions from the conduction band to the various valence bands in pm-InGaAs for TE and TM polarizations[27].

laser applications as TE modes dominate in Fabry-Perot lasers due to the higher facet reflectivity of this polarization[30]. The heavy hole transition strength is unchanged from that of unstrained material while the light hole dipole moment is reduced by a factor of $(\frac{1}{3})\alpha_0 P^2$ where and P is the momentum matrix element connecting the valence band and the conduction band).

The alteration of the dipole moment associated with biaxial compression is small for laser diodes operating in the TE polarization. The heavy hole band forms the band-edge and its moment is unaffected by the strain. The light hole band moment is reduced somewhat with strain but this band is shifted away from the band edge with the addition of small mole-fractions of indium such that it does not significantly affect the gain. The changes in dipole moment due

to the strain were therefore neglected in the calculation of the spectral gain described in Chapter 5. If the active regions were under biaxial tension rather than biaxial compression, as could occur in the growth of InGaAs/InP epitaxial layers, then the changes in dipole moment would not be negligible as the light hole band would then constitute the band edge.

2.c. Previous Related Work on Laser Diodes

The work previously published on laser diodes is vast. Among this literature are a few topics which have direct bearing on the work presented in this thesis. These topics are: modeling the spectral gain of diode lasers, the effect of strain on laser performance, and previous work on the use of pm-InGaAs as the active region of a diode laser.

Gain spectra for laser diodes have been calculated for a variety of different epitaxial layer structures: DH[2],MQW[31],[32] and GRIN-SCH[33],[34]. Since current devices are typically constructed with undoped active regions, band to band processes are assumed dominant (rather than conduction band-impurity transitions as in earlier devices with doped active regions[2]). The details of the derivation of the gain spectra expression, for GRIN-SCH structures, are given in Chapter 5. This derivation follows closely that of Asada, *et. al.*[33] and Chinn, *et. al.*,[34].

A number of researchers have investigated the effect strain has on the performance on laser diodes. The earliest work in this area was a study of polarization changes in laser diode output due to the application of mechanical stress[35],[36]. It was found in this work that the polarization of the laser output could be switched

between TE and TM by the application of compressive stress to the top, (100), surface of the diode. This polarization change was explained in terms of the effect strain had on the band structure of the active region. In particular, how strain affected the wavefunction of an acceptor state (the devices studied in this work were DH lasers with p-type doped active regions), and the impact of this on the relative magnitude of the TE and TM dipole moments.

A theoretical analysis of the effects that strain related band structure perturbations have on the performance of lasers with undoped active regions was done by Dutta[37]. In this work, expressions for the material gain for the TE and TM polarizations, interacting with the carriers via band to band transitions, were derived. These expressions dealt with the mass shifts associated with the splitting of the valence band degeneracy, as discussed above, but neglected changes in the dipole moment due to mixing of the light hole Bloch functions (as would arise from interaction between the light hole band and the spin-split band). The model developed was only applicable to DH lasers since quantum confinement effects on the gain spectra were not taken into account.

The model implemented in this thesis is a synthesis of the work of Asada, et.al.[33] on quantum well lasers and the modeling of Dutta[37] dealing with strain effects on DH laser operation.

It has been predicted by Yablonovitch and Kane[38] that a reduction in the valence band mass (such as would occur via the use of material under biaxial compression as the active region of a laser diode) would reduce the steady state carrier density at which the Bernard-Duraffoung condition for lasing would be met. This reduction

was predicted to come from the fact that the quasi-Fermi energies for the bands increase faster in energy, as carrier density is increased, in a band with a lower density of states (as would result from a lower mass). Quantitative prediction of the degree to which the strain perturbation to the carrier masses should reduce the threshold carrier density in pm-InGaAs lasers is given in Chapter 5.

A number of other researchers have investigated the use of pm-InGaAs as the active region material in laser diodes[6],[7],[39]. These papers describe the performance of singular devices without dealing with specific problems in the growth of the epitaxial layers or the effect of strain on the device performance. Devices described in this work demonstrated lasing out to 1.0 micron wavelength but the threshold current densities reported seem limited by extrinsic effects (such as non-radiative recombination). The crystal growth problems associated with this epitaxial layer structure have recently been overcome by both MOCVD[40],[41] and MBE[42] and devices displaying low threshold current densities and room temperature continuous wave (CW) operation have been demonstrated. It is unclear though if the strain induced enhancement in the threshold current predicted by Yablonovitch and Kane was seen in these devices[43].

3. Experimental Technique

The experimental work in this thesis involved the construction of a series of pm-InGaAs GRIN-SCH lasers with various indium concentrations. The effort required to achieve this was directed into three major areas:

- a. Growth of the epitaxial crystal layers,
- b. Fabrication of the devices,
- c. Packaging and test.

The details of each of these topics will be discussed separately.

3.a. Growth of Laser Epitaxial Layers

The growth of good laser diode epitaxial material involves a number of difficult choices concerning growth conditions. Many of these decisions can benefit from reference to the literature but experimentation is required to establish the correspondence between published growth conditions and those specific to a particular MBE system. The pm-InGaAs growths described below culminated an effort to produce good laser material which involved the growth of over 20 different laser epitaxial layers and numerous calibration samples. The pm-InGaAs laser layers described here were all grown in the period of one week to insure that the quality of the material was unchanged.

The laser epitaxial layer structure studied was that shown in Figure 3.1. The indium concentrations in the InGaAs layers were 0%, 10%, 20%, 30%, and 40%. The quantum well width was 10 nm. The critical indium concentration for a 10 nm thick film is 28%; the concentrations produced were intentionally designed to bracket this critical point as shown in Figure 3.2

The target compositions and thicknesses and doping of the

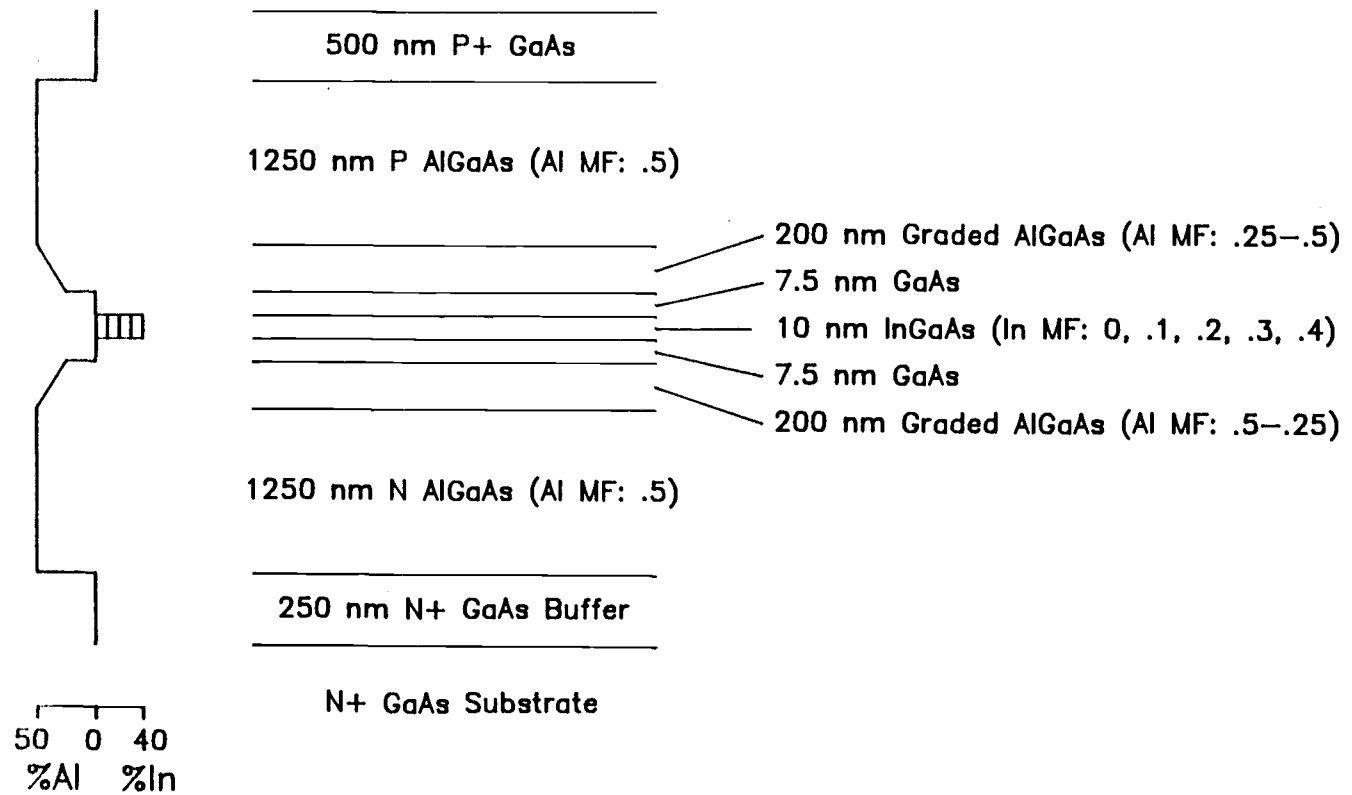


Figure 3.1: A diagram of the pm-InGaAs GRIN-SCH epitaxial layer structures grown in this work.

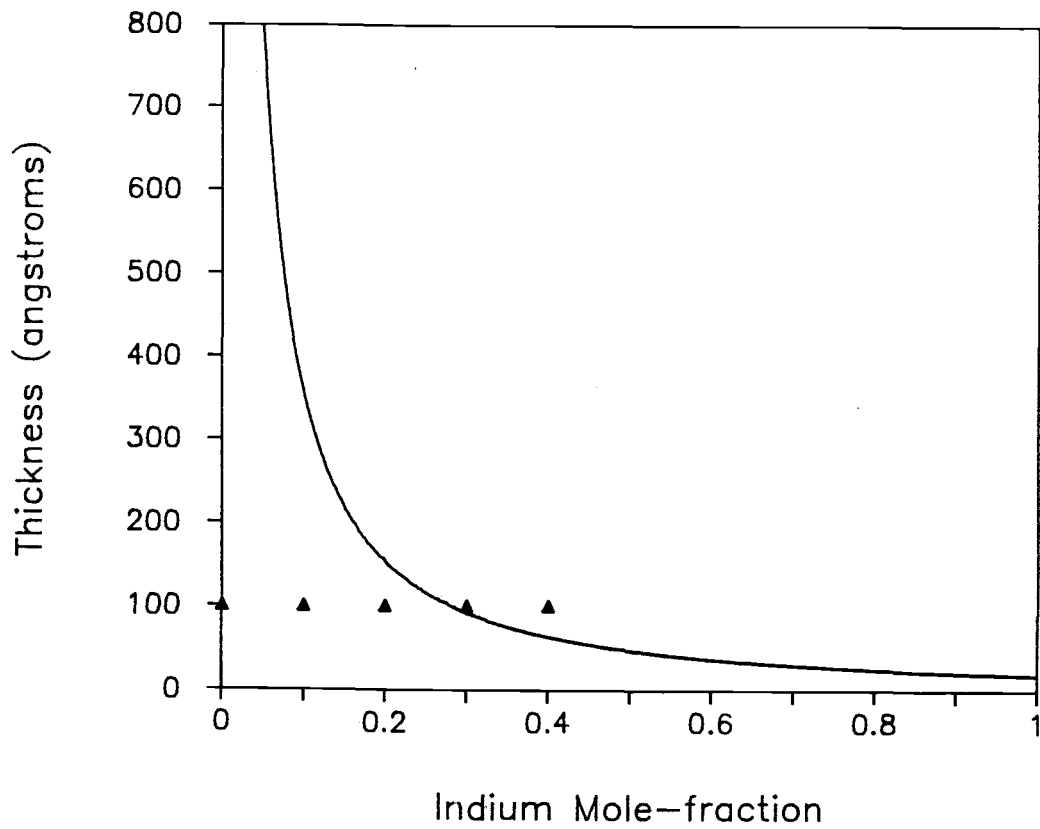


Figure 3.2: Critical thickness curve (solid line) and the indium concentrations and quantum well widths of the fabricated devices (triangles).

layers in this structure were obtained from the literature. Two papers in particular were used extensively: one describing an empirical study of AlGaAs/GaAs GRIN-SCH structures by Tsang[12] and the other describing a pm-InGaAs laser diode structure grown by MOCVD by Fischer, *et. al.*, [40].

The laser epitaxial layers were grown in a Perkin-Elmer 425B MBE system. The system consisted of two chambers: analysis and growth. The analysis chamber was equipped with a heated outgassing stage and a Phi 545 Scanning Auger Microscope. The growth chamber contained Reflection High Energy Electron Diffraction (RHEED) and a UTI 100C Quadrupole Mass Spectrometer (QMS) as well as source ovens. The source elements available in the system were gallium, aluminum, indium, arsenic, silicon and beryllium. The highest purity source material available was used, as shown in Table 3.1. The silicon was a piece of high purity polycrystalline material which SEH-America used as the raw material for pulling silicon single crystal ingots.

Element	Vendor	Purity
gallium	Alcan Electronic Materials	99.999999%
aluminum	Alfa Chemical Co.	99.9999+%
indium	Alfa Chemical Co.	99.9999%
arsenic	Furokawa Inc.	99.999999%
silicon	SEH-America, Inc.	unknown
beryllium	Atomergic Chemical Co.	99.9999%

Table 3.1: Purity and vendor of the MBE source materials used.

All the fluxes were generated thermally. The arsenic source was a solid boule from which arsenic, in the form of As_4 , was sublimed and subsequently thermally cracked to As_2 . Silicon and beryllium were available as dopants, n-type and p-type, respectively.

The substrate material used in the epitaxial growth was purchased from American Crystal Technology and MA/COM Laser Diode. Material from both vendors had similar specifications, as shown in Table 3.2. The polished surface of both vendors material showed visible diffuse scatter when illuminated by an intense microscope

orientation:	{100} $\pm .2^\circ$
free carrier concentration:	$2.0-5.0 \times 10^{18}$ electrons/cm ³
etch pit density:	< 400/cm ²
single side polished	

Table 3.2: Substrate material specifications.

light. This indicated that the polish was not perfect but the material was deemed acceptable.

The substrates were prepared, previous to growth, via standard procedure: sequential, room temperature, static, baths of Trichloroethane (TCA), Acetone, Methanol and de-ionized (DI) water, 2 minutes each. A chemical etch in a solution of 5% Choline in water was then done, static, at room temperature for 1 hour. The substrates were rinsed for 15 minutes in running DI water, spun dry and attached to molybdenum blocks.

The substrates were indium bonded to molybdenum holders for transport in the MBE system rather than mounted solder free. This method was chosen due to the excessive amount of slip observed in samples which used the solderless mounts, as well as the irregularity in the shape of Horizontal Bridgeman (HB) grown substrate material.

Previous to the growth of each structure the fluxes of the Group III metals were calibrated on a separate substrate. The compositions for which calibration was done were: Al_{0.5}Ga_{0.5}As,

$\text{Al}_{.25}\text{Ga}_{.75}\text{As}$ (the endpoints of the graded regions) and GaAs. The desired growth rate for each of these was 1 mono-layer/second (one mono-layer is one gallium atomic layer and one arsenic atomic layer, equal to 0.283 nm). Intermediate compositions in the graded region were obtained by allowing the oven controller to interpolate linearly both the gallium and aluminum oven temperatures between the calibrated endpoints. The growth rate was assumed to remain close to 1 monolayer/second during this interpolation and the ramp time determined accordingly. Numerical simulation of this procedure, excluding thermal lag effects in the ovens, yielded almost linear composition variation between $\text{Al}_{.5}\text{Ga}_{.5}\text{As}$ and $\text{Al}_{.25}\text{Ga}_{.75}\text{As}$ but a layer thickness of 196 nm instead of the desired 200 nm. The results of this simulation are shown in Figure 3.3. The program to accomplish this is part of the laser diode model, subroutine 'compgen', listed in the appendix.

The oven calibration was done by measuring the temporal oscillations in the RHEED pattern subsequent to opening the Group III element (gallium or aluminum) oven shutter. These oscillations have been shown to correspond to the deposition of one monolayer of material[53]. The oscillations were measured with the RHEED electron beam incident in a $\langle 100 \rangle$ direction on the substrate surface, at the bright point on the screen where two Kikuchi lines cross the specular streak. Spatial selection of this spot was accomplished by placing an optic fiber bundle against the RHEED window. A photomultiplier (PMT) was used to convert the light from the RHEED phosphor screen into an electrical signal which was then stored in a digital oscilloscope. The period of the oscillations was obtained by measuring the peak

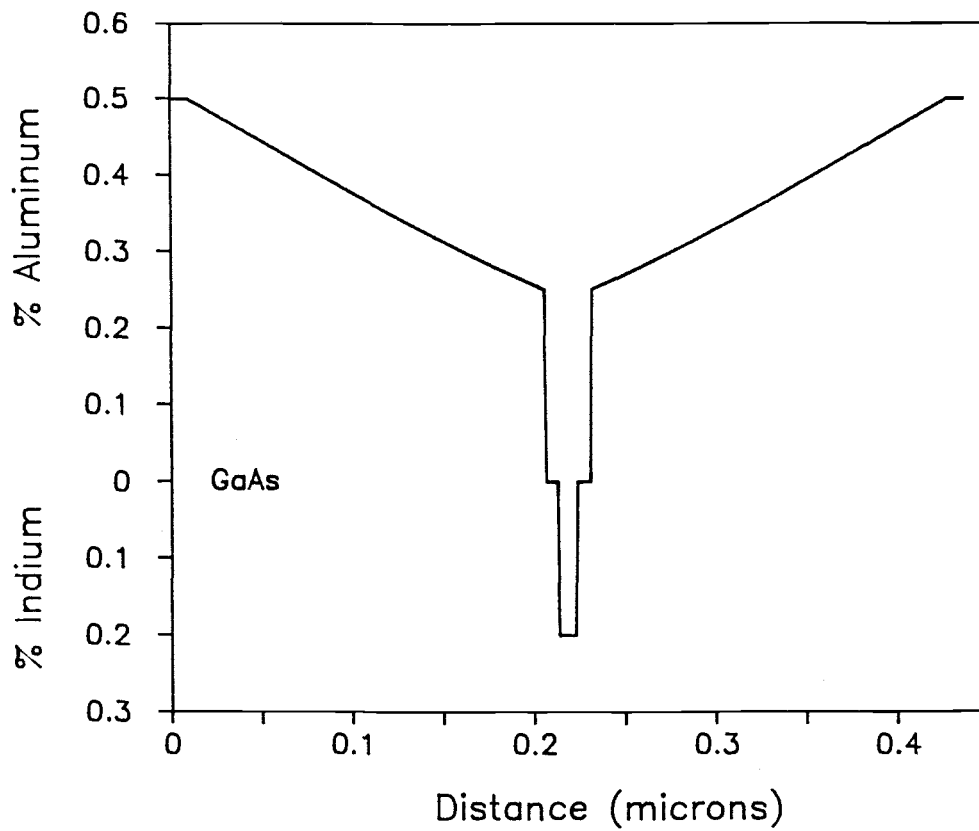


Figure 3.3: Simulated composition variation with distance for the 0.20 mole-fraction indium structure grown in this work.

spacing against the oscilloscope graticule.

Determination of the appropriate flux to grow a particular film composition was complicated by the need to grow the majority of the laser structure at high substrate temperature. The amount of gallium which desorbs from the growing surface is a function of substrate temperature, arsenic overpressure and aluminum flux at the high substrate temperature necessary for the growth of high quality $\text{Al}_{.5}\text{Ga}_{.5}\text{As}$ [22]. Calibration using RHEED oscillations is only feasible at growth temperatures below 600°C . Above this temperature the magnitude of the temporal oscillations is too small for reliable calibration. This problem is dealt with by calibrating the gallium oven flux, at low substrate temperature, to a flux which is calculated using an assumed net incorporation rate for gallium, at the higher growth temperature, of 85%. The value of 85% was derived from our own empirical studies of films grown under conditions similar to those of the laser growth and is supported by other evidence in the literature[23],[56]. The net incorporation rate of aluminum is assumed to be unity at all growth temperatures.

After calibration, the molybdenum block holding the laser substrate material was placed into the growth chamber and heated to desorb the native oxide. The oxide desorption temperature was assumed to be 585°C and the emittance setting of the optical pyrometer was adjusted at the time at which the RHEED pattern changed from diffuse to ordered such that the pyrometer read this value. In this way temporal variation in the thickness of the arsenic coating on the pyrometer window and variation in the emissivity between molybdenum blocks, was corrected for. The pyrometer used to monitor the

temperature of these samples was an IRCON Model 6000 which measures spectral emission in a wavelength range at which the GaAs substrate is transparent. The temperatures measured were therefore the block temperatures, not the actual substrate temperatures, and are representative of the substrate temperature only when there was intimate contact between the block and the substrate.

The layers described in Figure 3.1 were grown with the following temperature profiles. The growth temperature of the $\text{Al}_{.5}\text{Ga}_{.5}\text{As}$ cladding layers was 690°C . The temperature was gradually decreased to 670°C during the growth of the graded AlGaAs layers. In the growth of the 0% indium active regions the substrate temperature was kept at 670°C for the GaAs growth and the temperature profile was reversed for the growth of the rest of the structure. During the growth of the indium containing structures the same temperature profile was utilized up to the end of the graded region. At that point 7.5 nm of GaAs was deposited and the growth interrupted. The temperature was then dropped to 530°C and the InGaAs was grown. After closure of the indium shutter the substrate heater was turned up to the highest safe operating current (14 amps) and 7.5 nm of GaAs was grown. The rest of the structure was then grown immediately without stopping growth at the terminus of the second GaAs layer. The substrate temperature at the beginning of the second AlGaAs graded layer growth was 590°C and it was approximately 2 minutes before the temperature rose to the desired temperature of 670°C .

This temperature profile is outlined in Figure 3.4. The low growth temperature of this AlGaAs interface is thought to be a source of carrier loss in the laser structure, due to non-radiative

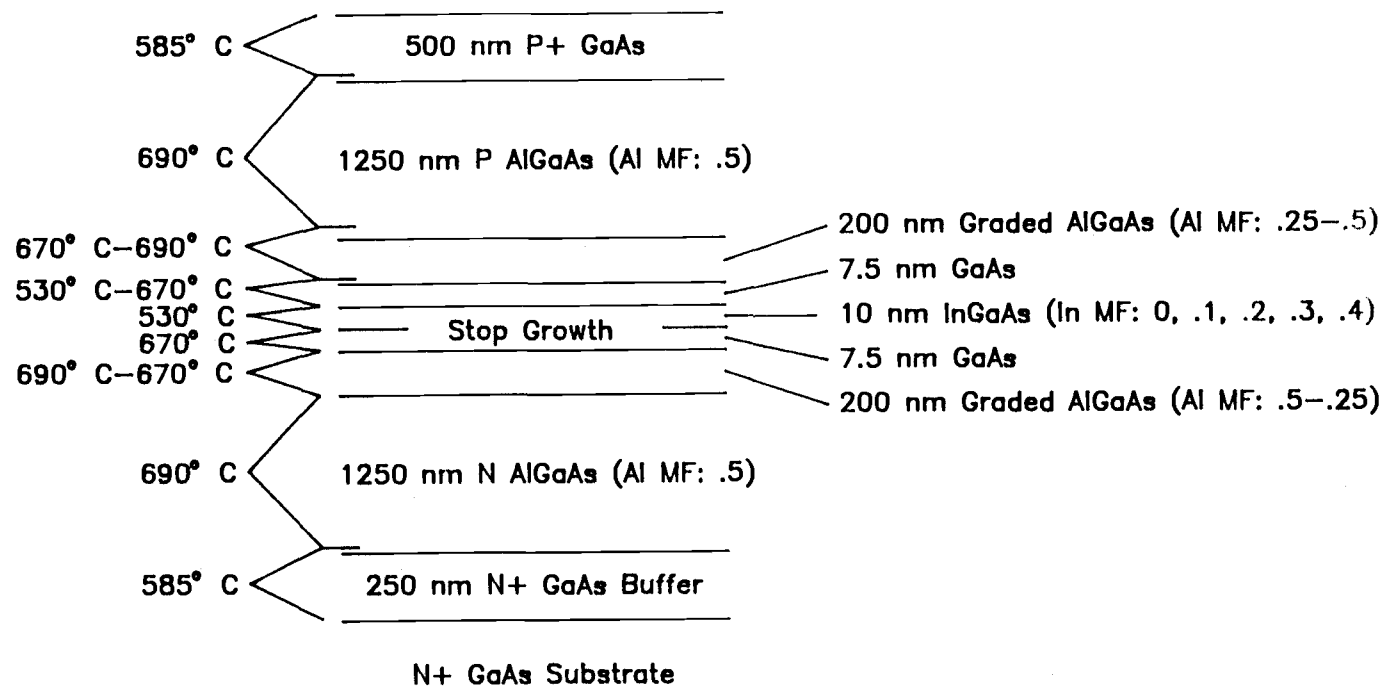


Figure 3.4: A diagram of the pseudomorphic InGaAs structures grown in this work, including the growth temperatures of the individual layers.

recombination, as will be discussed in Chapter 6.

The morphology of the epitaxial layers was good, in general. There were the omnipresent particulate related defects as the preparation of the samples was not done in dust free conditions but none of the directional waveness which characterizes AlGaAs which is grown at too low a substrate temperature[54]. In places where indium had noticeably evaporated from the backside of the substrate there was a long range waveness, the origin of which is unknown. In all growths there was enough good material to attempt 3 or 4 process runs.

3.b. Device Fabrication

The process developed to construct lasers from the epitaxial material consisted of 6 photo-lithographic steps. The complexity of the process was due to the fact that both ohmic contacts were made to the top side of the die, which is desirable when attempting to construct devices which operate at high pulse rate as it allows a reduction in device capacitance[55]. A process for the construction of discrete lasers could have been accomplished in as few as two mask levels if backside contact to the substrate was used.

The process equipment used in fabrication of the laser diodes was fixtured for two inch wafers but the mask was designed to cover only a 8 mm x 8 mm square area (and would produce 96 lasers if the yield was perfect). To avoid waste of precious epitaxial material the laser epitaxial wafers were scribed and cleaved into 1 cm squares, the edges aligned to the {110} cleavage planes. Up to four of these pieces could be processed simultaneously by indium soldering them to a two inch, circular, molybdenum plate. This allowed in-process pieces to be handled easily and was compatible with the fixturing of all the

process equipment.

To cleave the 1 cm^2 pieces, from the wafer, an edge scribe was done and the sample bent over a humped surface. An edge scribe, rather than a full scribe, was done because the piece needs to have edges which are as close to the $\{110\}$ cleavage planes as possible and the crystal will break along a full scribe line even if it was significantly off of the cleavage plane. The requirement that the sample be cleaved as closely to the $\langle 110 \rangle$ direction as possible arises from the fact that the first mask level needed to be aligned as closely as possible to a $\langle 110 \rangle$ direction so that the cleaved mirrors were perpendicular to the active region stripe.

The etching characteristics of the different $\{111\}$ faces of GaAs dictates that the the mask had to be aligned such that the stripes were parallel to the $(0\bar{1}1)$ plane or the chemical etches would produce undercut sidewalls which could cause breaks in the metalization. The use of HB grown material made the distinction between the $(0\bar{1}1)$ and the $(01\bar{1})$ difficult to determine as there were no flats on the wafer. The etch sidewalls of the first mesa were viewed in a light microscope subsequent to the first mask step and the sample was discarded if the first mask level was misoriented 90° .

The process steps to construct the lasers were as follows:

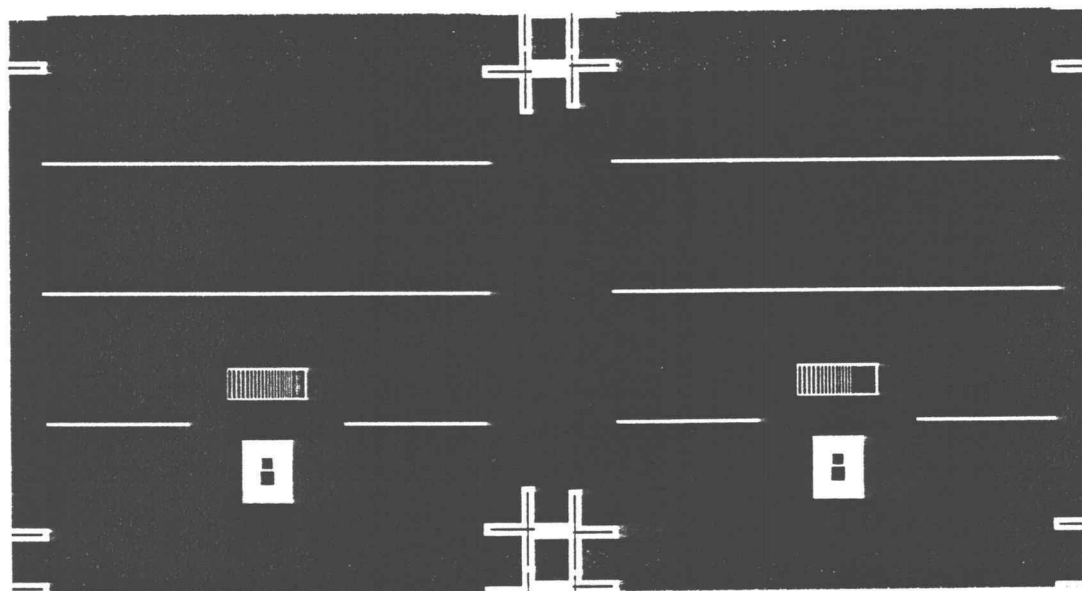
1. cap layer etch,
2. etch down to N^+ substrate,
3. n-type contact lift-off,
4. p-type contact lift-off,
5. deposition of SiO_2 ,
6. contact anneal,
7. via etch through the SiO_2 ,
8. bonding pad lift-off,
9. facet cleaving.

All the etching was accomplished with wet chemical methods. The ohmic contacts and bonding pads were formed by vacuum evaporation of the appropriate metallurgies. The SiO_2 was deposited via DC sputter deposition from a quartz target. All the lithographic procedures in this process used AZ-1518 positive resist. Lift-off was done using a procedure which involved a chlorobenzene soak, adapted to our laboratory by Dr. Hyung Mo Yoo. Details concerning the basic process steps and equipment operation are described in the OSU Advanced Materials Laboratory Guidebook.

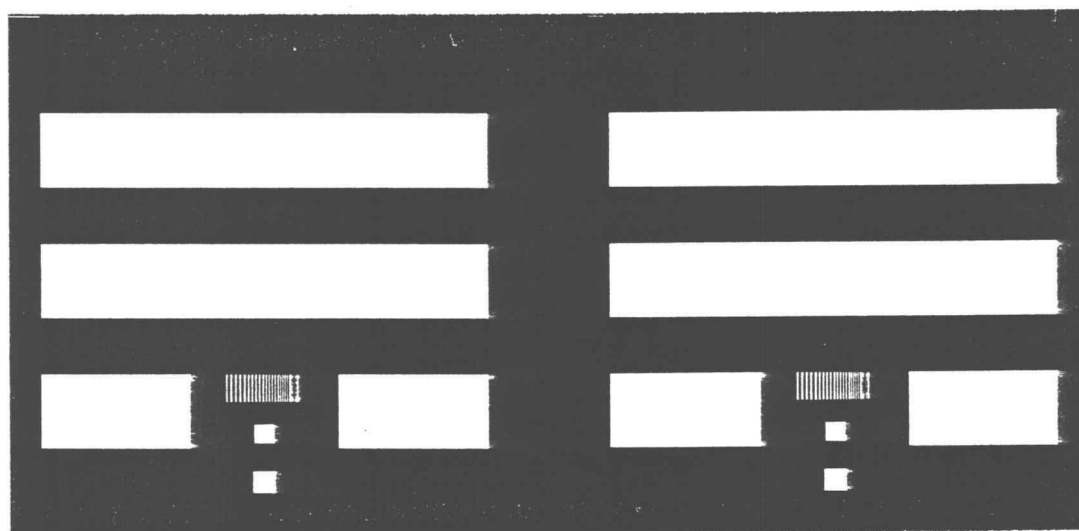
Reproductions of all the mask levels are shown in Figure 3.5. There were only four masks constructed to accomplish the six lithographic steps. The same mask was used repeatedly in the contact lift-off and via etch steps.

The first mask delineated a pattern which allowed the removal of the cap layer everywhere except for 10 micron wide stripes. This defined the active regions of the lasers as the higher contact resistance associated with regions where the cap had been removed blocked current flow through these paths. It was extremely important that the first mask be aligned perpendicular to the cleavage plane of the crystal or the Fabry-Perot resonator would be unstable, as mentioned previously.

The solution used to etch the GaAs cap layer was 10:1, citric acid solution (50% by wt. in H_2O): H_2O_2 . This etchant was found to have two useful properties: it was anisotropic in respect to etching various crystal planes and it etched p-type GaAs approximately 25 times faster than p-type $\text{Al}_{.5}\text{Ga}_{.5}\text{As}$. The etch rate on {100} planes was approximately 1 micron per minute. The etch rate on {111}A planes

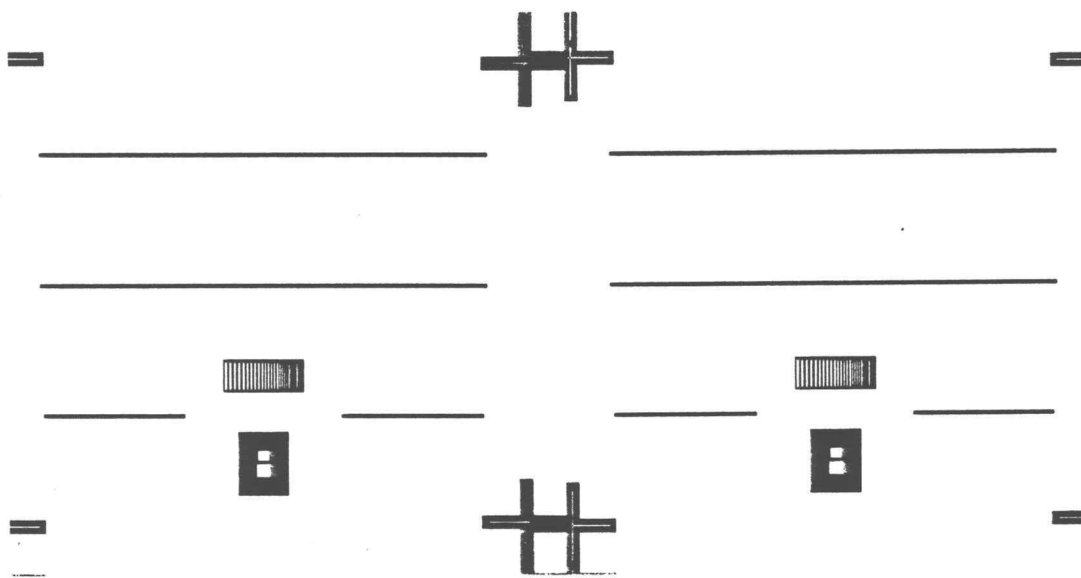


Mask 1

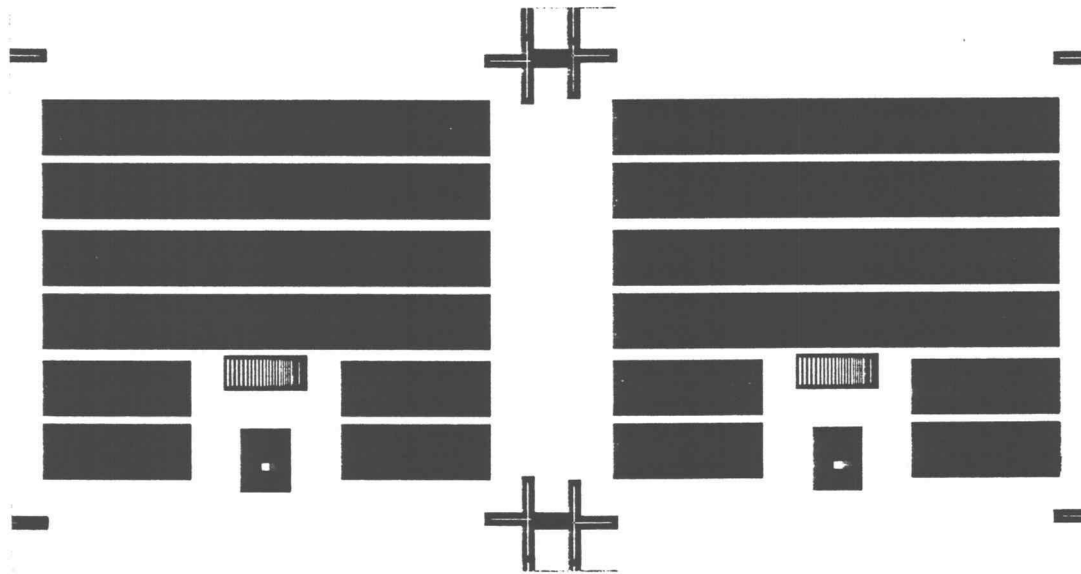


Mask 2

Figure 3.5: Reproductions of the masks used to construct the laser diodes built in this work. The dark areas correspond to where the resist would be open.



Mask 3



Mask 4

Figure 3.5: continued

was slower by about 5 times. The resultant sidewall profile was sloped at a 55° angle which eased the problem of metalization off of the mesa. The etch stopped precisely on the cap layer-cladding layer interface with little over-etching.

The second mask step exposed the regions where the epitaxial layer was removed to expose the substrate so that the n-type contact could be made. The solution used to accomplish this was $\text{H}_3\text{PO}_4:\text{H}_2\text{O}_2:\text{H}_2\text{O}$ mixed in a ratio of 1:9:1. This solution etched both AlGaAs and GaAs, stopping on the $\{111\}$ A planes of the p-type $\text{Al}_{.5}\text{Ga}_{.5}\text{As}$ and the $\{311\}$ A planes of the n-type $\text{Al}_{.5}\text{Ga}_{.5}\text{As}$. The resultant mesa profile, although kinked, also allowed metal to be evaporated over it without breakage.

The procedure for performing the etches involved repeated etch and stylus profilometer measurement of the etch depth until the desired total depth was achieved. This procedure was necessary due to the high variability in etch rates found with the same etchant solution. This variability was thought to arise from chemical aging, variation in etch temperatures and differing initial surface condition, e.g., oxidized versus oxide free.

The third step used mask 3 to define the n-type ohmic contact region. This contact was made to the N^+ substrate which was exposed in mask step 2. The contact geometry was a 10 micron wide stripe which extended the length of the device. The stripe was located 40 microns from the edge of the mesa formed in mask step 2. After completion of the lift-off lithographic steps the sample was immediately placed in the evaporator. When a system pressure of 10^{-6} Torr. was achieved the n-type ohmic contact metallurgy, 10 nm

nickel, 120 nm gold- germanium eutectic, 150 nm gold, was evaporated sequentially. This was done without exposing the sample to air between the deposition of the different metals.

The fourth step again used mask 3 to pattern the p-type contact metallurgy. The mask was aligned to the 10 micron mesa previously defined in mask step 1. The metallurgy used to form the p-type contacts was 10 nm gold, 50 nm zinc, 150 nm gold, evaporated sequentially. The first gold layer provided a surface to which the zinc would stick and the final gold layer acted as an encapsulant.

The fifth step was the sputter deposition of 100 nm of SiO_2 . The SiO_2 served as an encapsulant to prevent arsenic loss and surface oxidation during the contact anneal and also provided an electrically isolated surface on to which the bonding pads were evaporated. The breakdown voltage of this oxide was measured at 4 MV/cm, adequate for isolation of the bonding pads.

The sixth step was the contact anneal. This was done in a tube furnace at 420° C, in air. Forming gas was assumed unnecessary as the surface was completely encapsulated by SiO_2 . The anneal time was 5 minutes, in the tube. The p-type and n-type contacts were annealed simultaneously.

The seventh step was the etch of the SiO_2 from above the contacts. Mask 3 was exposed twice on the same resist, once over each contact. The SiO_2 was chemically etched in a solution of hydrofluoric acid buffered with ammonium fluoride (BHF). Care was taken not to overetch the SiO_2 as $\text{Al}_{0.5}\text{Ga}_{0.5}\text{As}$, which was directly beneath, also etches in this solution. Underetching was also undesirable as a thin oxide layer would result in poor electrical connection between the

contact metal and the bonding pads.

The final mask step was the lift-off of the bonding pads. Mask 4 was used to form the pattern. The thicknesses and metals used were 10 nm of titanium and 250 nm of gold. The function of the titanium was to increase the adhesion of the gold to the SiO_2 . It was thermally evaporated from a molybdenum boat.

After the completion of the lithographic steps the samples were removed from the molybdenum disk. Residual indium was removed from the backside of each by an etch in concentrated hydrochloric acid (HCl). The formation of the mirrors was done by breaking the sample along the {110} cleavage planes, perpendicular to the orientation of the stripe define by the first lithographic step. The samples needed to be thinned to 75 microns to get good cleaved surfaces. This was done by individually waxing each sample, face-down, to a stainless steel puck and lapping off the backside with a 600 grit Silicon Carbide (SiC) slurry. The last 25 microns of the backside polish was done via a chemical polish, 2% bromine in methanol, on filter paper. The chemical polish was done to remove the damage created by the mechanical lapping.

In both the mechanical and chemical polishing steps it was extremely important to ensure that the sample retained its flatness. This was accomplished by periodically measuring the height of the sample/puck combination using a .0001" accurate dial gauge. Measurements were taken on all four corners of the sample and additional pressure during subsequent lapping was applied to the highest point in order to regain flatness.

Once the sample was thinned to the appropriate thickness it

was rinsed thoroughly in methanol and DI water. It was removed from the puck by warming the combination on a hot-plate, applying fresh wax around it, and sliding it off onto a piece of filter paper. The wax was then removed via sequential soaks in TCA, acetone, methanol and DI water and the sample then gently blown dry. At this point extreme care in the handling of the sample was exercised as its thinness made it extremely fragile.

The sample was adhered, face up, to a piece of "frisking" (low tack) paper to hold it during scribing. The frisking paper was then held in a vacuum chuck and the scribing done under a low power binocular microscope. Edge scribes were made in the excess 1 mm of material which surrounded the devices, 300 microns apart. A piece of wax paper was then placed over the scribed sample to hold it firmly and it was bent over the appropriate curvature table edge. If all the steps were done properly the result was clean, straight, cleaved bars with contact stripe running continuously between and perpendicular to the two facets. The bars were then cleaved in the opposite direction to form shorter bars of three lasers. These were gently picked off of the frisking paper with tweezers, being careful not to damage the cleaved facets. A cross-sectional diagram of a finished devices is shown in Figure 3.6.

3.c. Packaging and Test

Each of the bars of three lasers was inspected and those with good facets were mounted, via silver epoxy, to T0-5 headers. The headers had previously been milled such that they had an abrupt edge on one side and the laser die was mounted so that one facet faced out over the edge to minimize unwanted optical reflection. All three

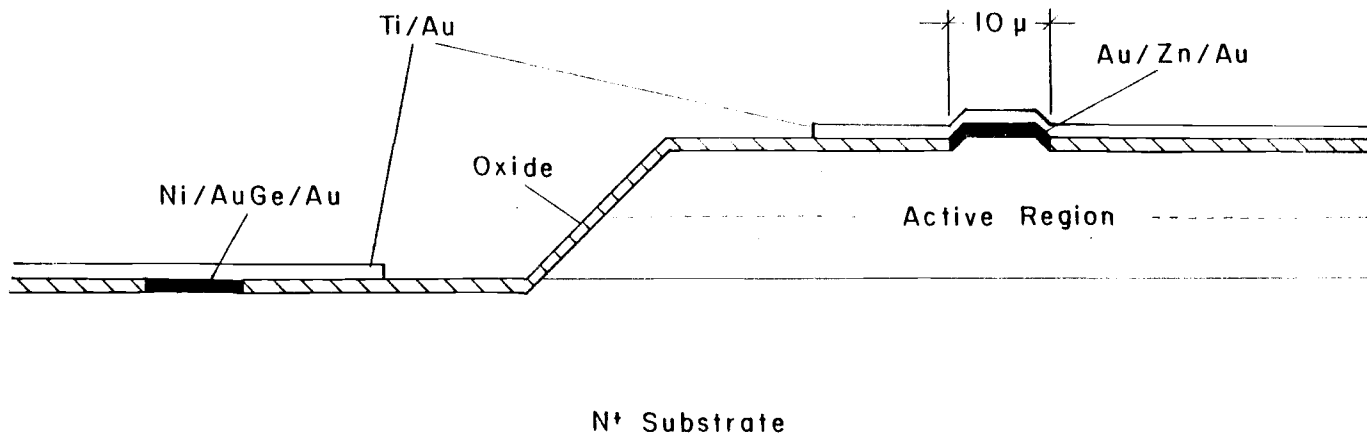


Figure 3.6: Cross-sectional diagram of the fabricated laser diodes.

devices were then wire bonded to separate pins. A photograph of the bonded package is shown in Figure 3.7.

The packaged devices were mounted on copper heat sinks which contained a lens to collimate the laser output. The heatsinks were mountable on standard optical bench equipment or in a Air Products LH-110 open cycle refrigerator. A photograph of the heat sink, with devices mounted in it, is shown in Figure 3.8.

Electrical and optical measurements were done on the devices. The electrical measurements, e.g., current-voltage (I-V) characteristics, were taken using a curve tracer and others using standard instrumentation. The optical measurements taken were light-current curves (L-I) and spectral measurements of the laser output above and below threshold. The L-I curves were measured either continuous wave (CW) or pulsed depending upon the threshold current of the particular device. If the threshold current of the diode under test was less than 40 ma then CW operation was possible, if not then the device was operated in a pulsed mode. All the measurements reported were taken at room temperature without cooling the heat sink.

The spectral measurements were taken using a 0.5 m Jarrel-Ash grating monochromator as the dispersive element and an S-1 photocathode PMT as the detector. In the case of CW operation the PMT output was measured directly with a ammeter, in pulsed operation a Princeton Applied Research 162-Boxcar Averager was used to extract the signal. In both cases the spectral output was recorded on a chart recorder.

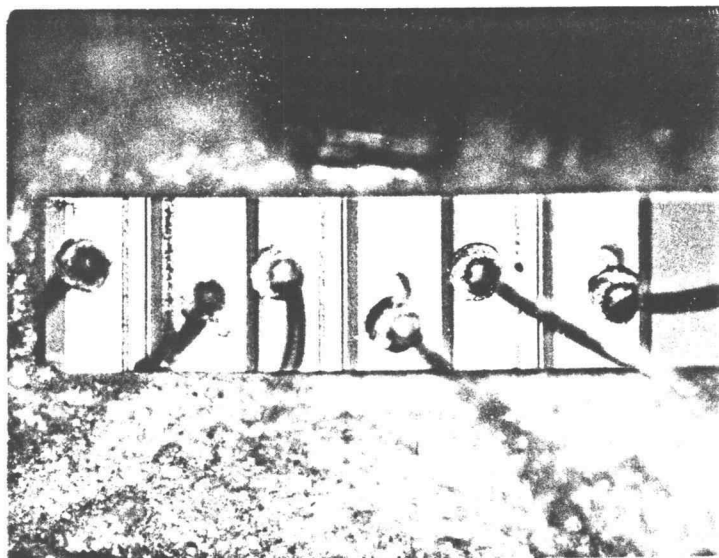


Figure 3.7: Photograph of the bonded devices, top view.

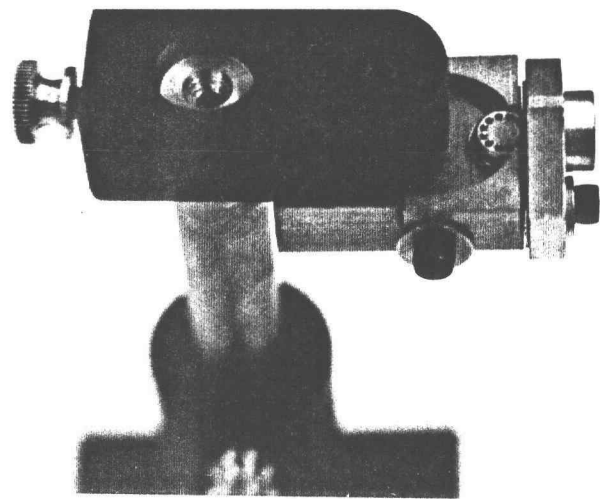


Figure 3.8: Photograph of the mounted devices in the heatsink.

4. Experimental Results

4.a. Measurements from the Epitaxial Layers

Photoluminescence was used to examine the epitaxial material prior to the fabrication of the devices. Along with the actual laser layers, a test structure was grown to confirm the critical thickness relationship at a InGaAs layer thickness of 10 nm. The indium concentrations grown in this structure were chosen to match those of the laser epitaxial layers. The test structure design is shown in Figure 4.1. Photoluminescence at 15° K was done on this structure and the spectra shown in Figure 4.2 was obtained.

Photoluminescence spectra from the actual laser epitaxial layers are shown in Figure 4.3. These spectra are normalized to the 0.0 mole-fraction indium peak. The P⁺ cap layer had to be removed from the samples otherwise the PL spectra showed only a bright GaAs peak.

4.b. Measurements of Device Performance

The voltage-current characteristic from the 0.0 mole-fraction indium laser is shown in Figure 4.4. Diodes from all five epitaxial layer structures displayed similar I-V curves. The device series resistance, measured off of the I-V curve at high forward bias voltage (around 30 mA), varied between 4 to 10 ohms, even between devices in one process run. Devices from all the different epitaxial layers displayed a similar series resistance spread. Lasers with good facets and low series resistance were chosen to be mounted and bonded.

Light output-current curves were measured from devices fabricated from the 0.0, 0.10 and 0.20 indium mole-fraction epitaxial layers. These curves are shown in Figure 4.5.

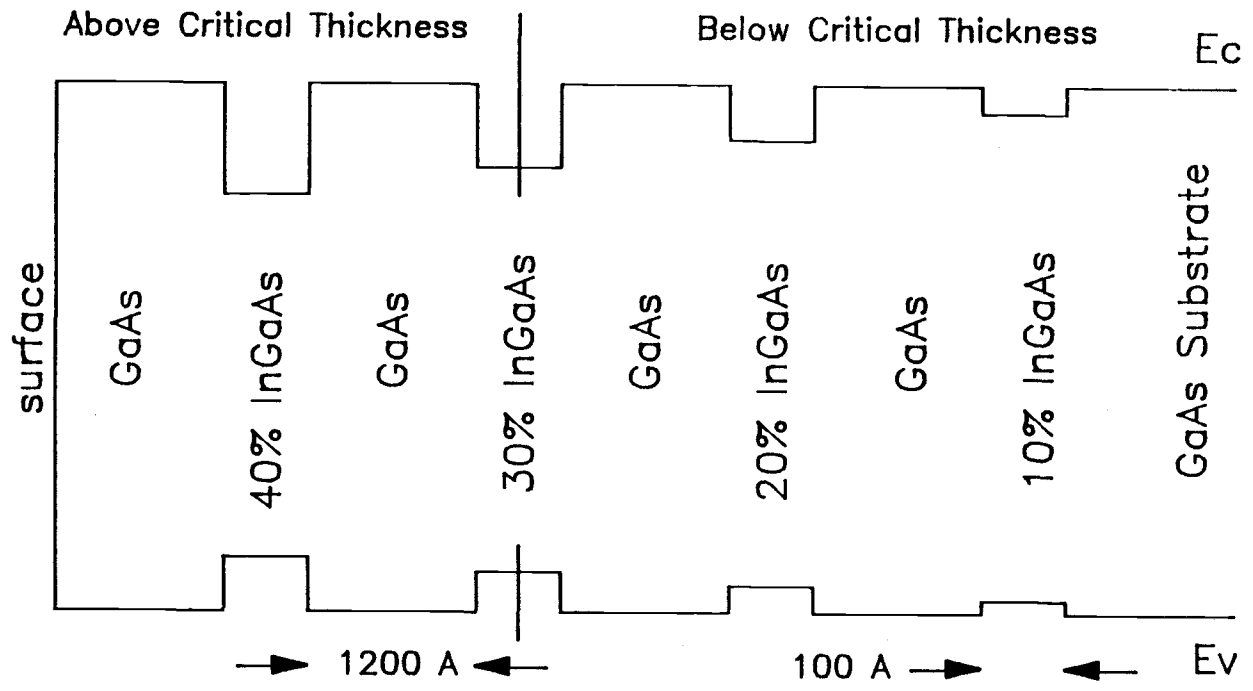


Figure 4.1: Epitaxial structure grown to test the critical thickness relation associated with the growth of 10 nm of InGaAs on GaAs.

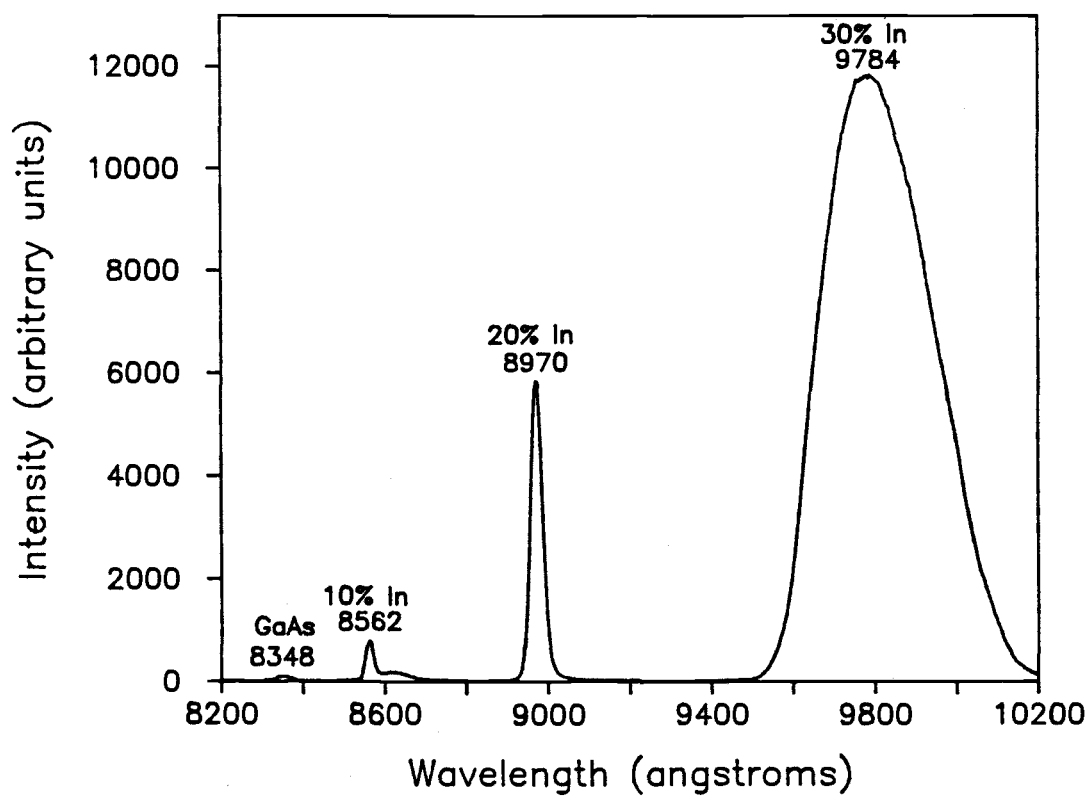


Figure 4.2: Photoluminescence spectra from the critical thickness test structure. The 0.40 mole-fraction quantum well peak is at a wavelength outside the detector sensitivity.

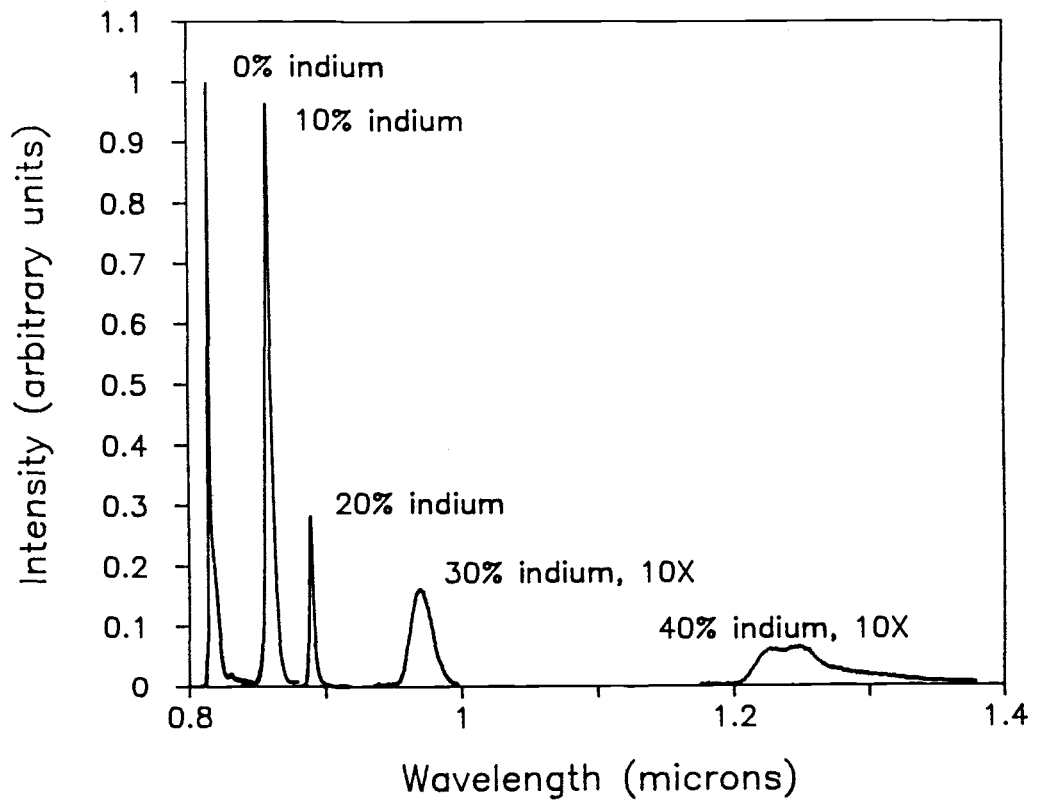


Figure 4.3: Photoluminescence spectra from the actual laser epitaxial layers after removal of the cap layer.

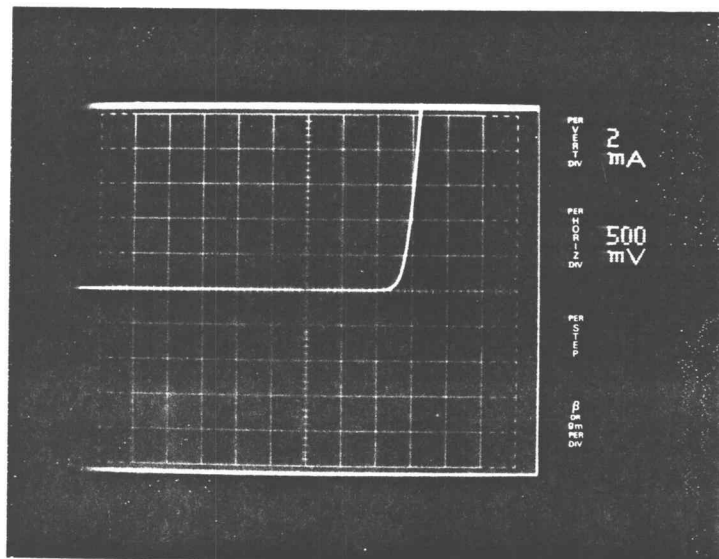


Figure 4.4: Current-voltage characteristic from the 0.0 mole-fraction indium laser diode. Devices from all the epitaxial layer structures showed similar I-V characteristics.

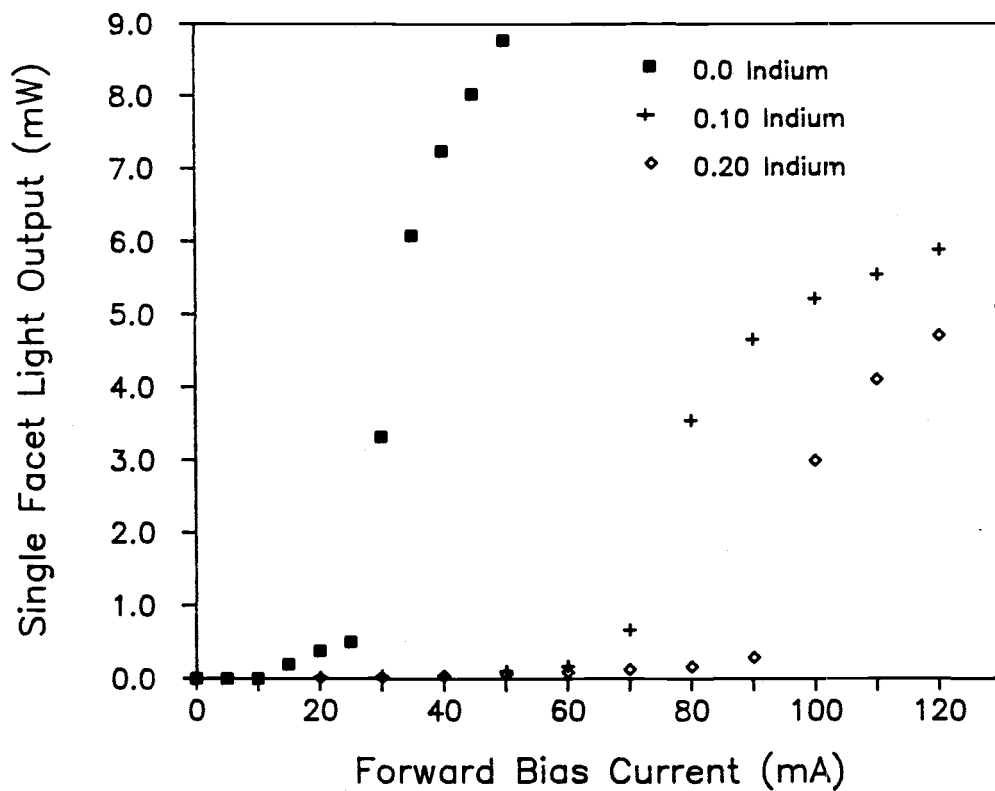


Figure 4.5: Light output-current curves for typical devices constructed from the 0.0, 0.10 and 0.20 mole-fraction epitaxial layer structures.

The spectral output from the 0.0, 0.10, 0.20 and 0.30 mole-fraction indium devices is shown in Figure 4.6 to Figure 4.9, respectively. The 0.40 indium mole-fraction devices displayed I-V characteristics similar to the other mole-fraction indium devices but no luminescence was observed. The far field pattern of the 0.0 mole-fraction device, operating at various forward bias currents, is shown in Figure 4.10. The patterns were measured by backlighting a sheet of paper with emission from the diode and photographing the front, with a 35 mm camera, using infra-red sensitive film

0%

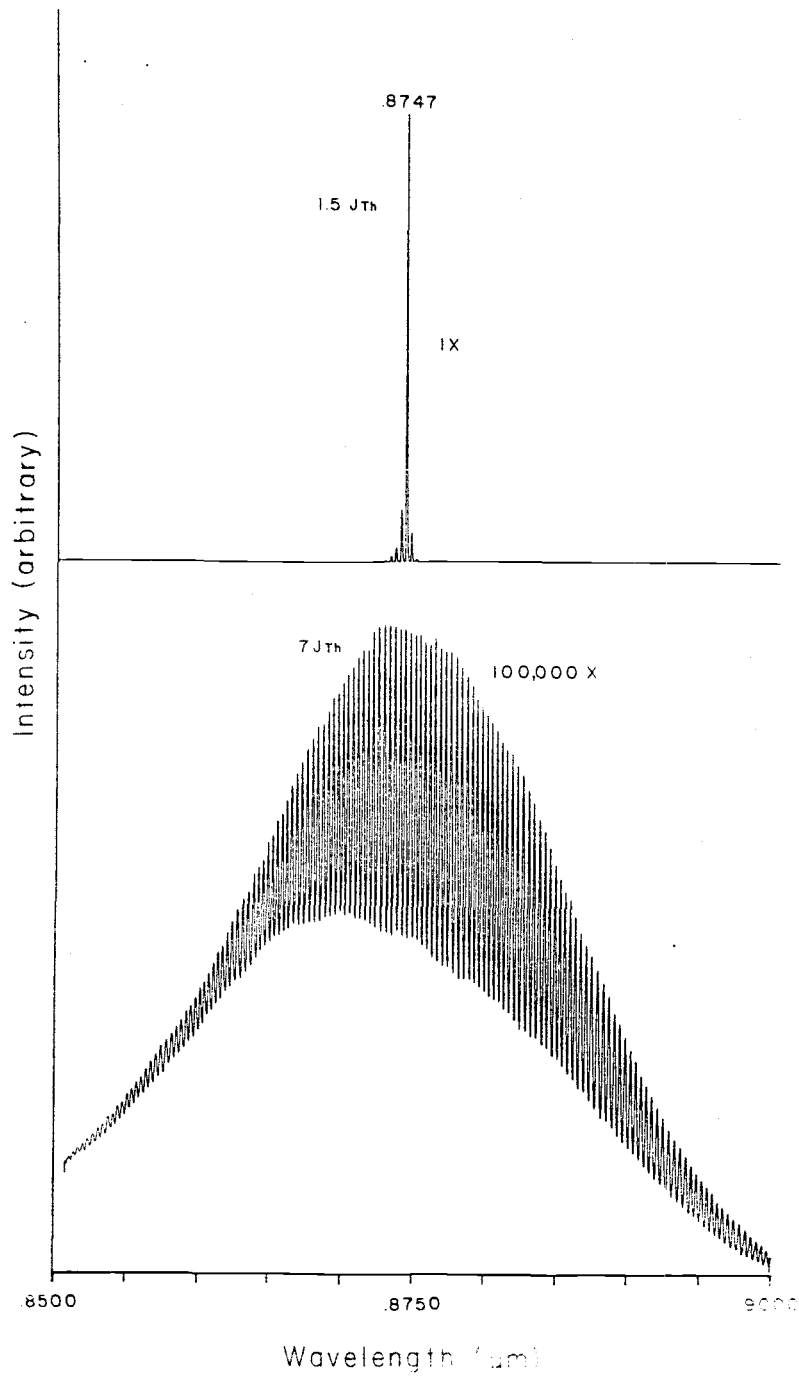


Figure 4.6: Spectral output below and above threshold from a device fabricated from the the 0.0 indium mole-fraction epitaxial layer.

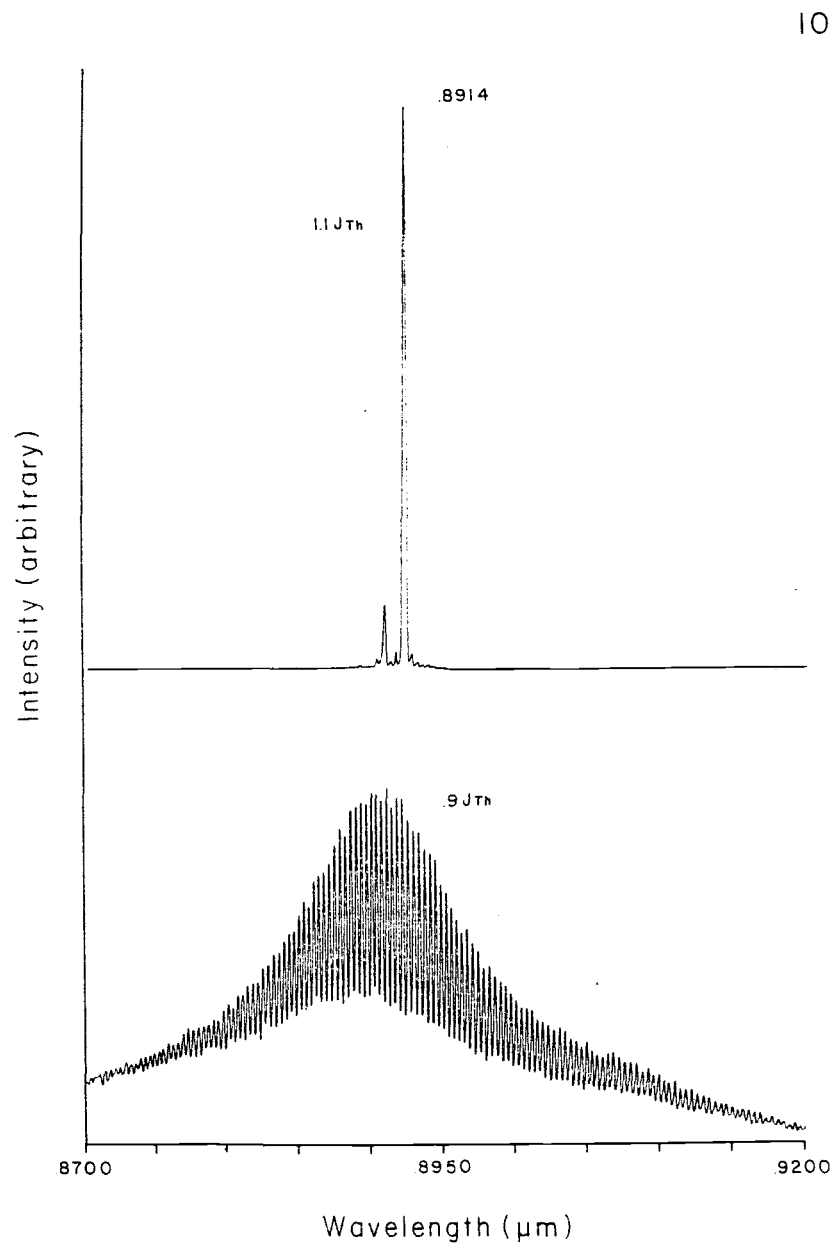


Figure 4.7: Spectral output below and above threshold from a device fabricated from the the 0.10 indium mole-fraction epitaxial layer.

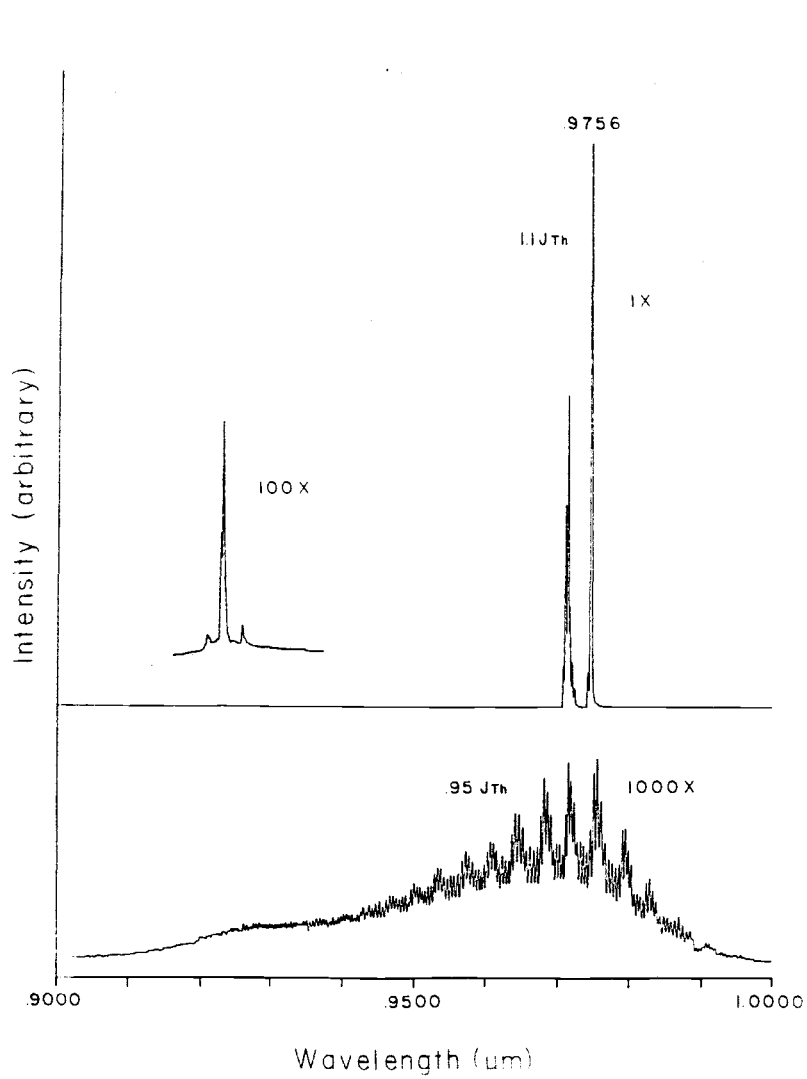


Figure 4.8: Spectral output below and above threshold from a device fabricated from the 0.20 indium mole-fraction epitaxial layer.

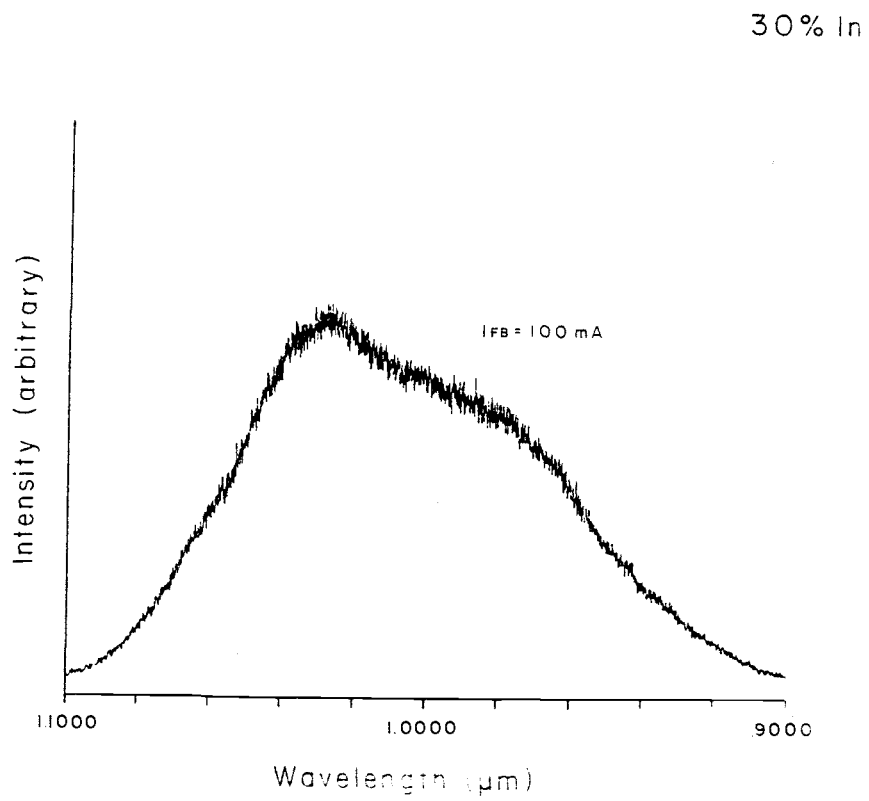
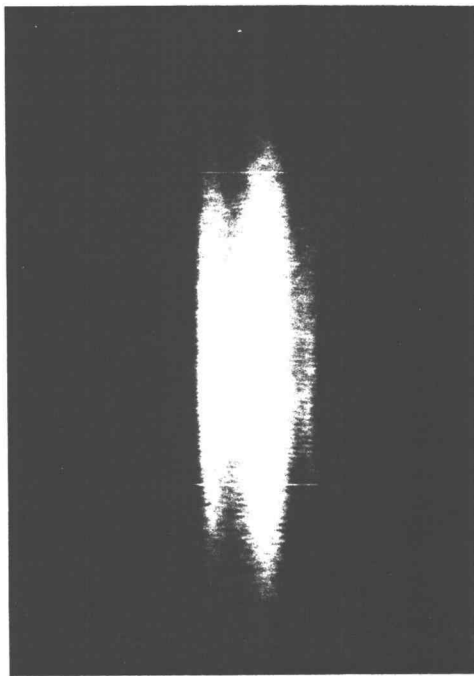
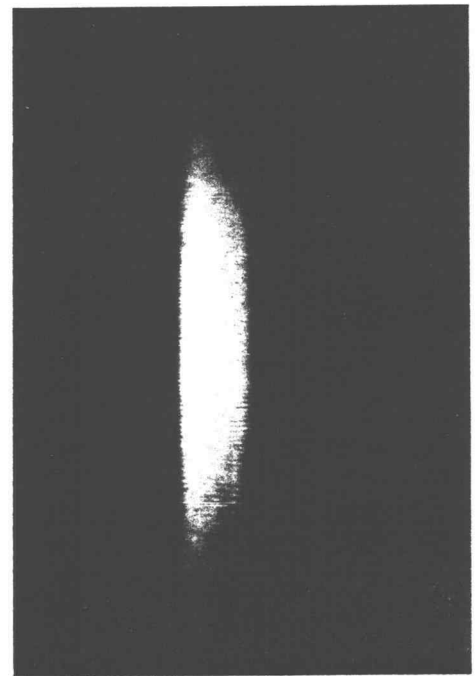


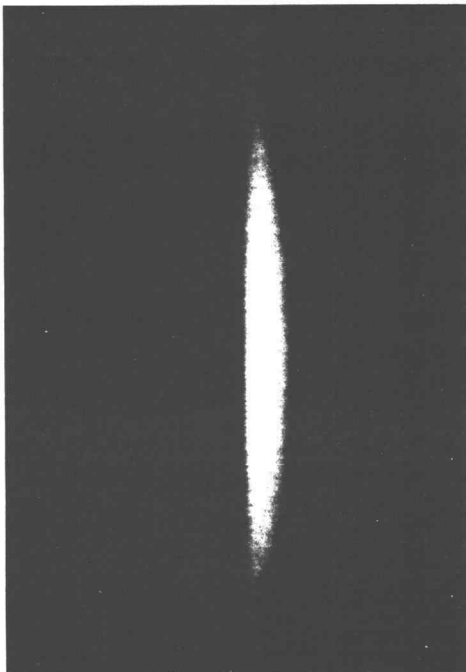
Figure 4.9 Spectral output from a device fabricated from the 0.30 indium mole-fraction epitaxial layer.



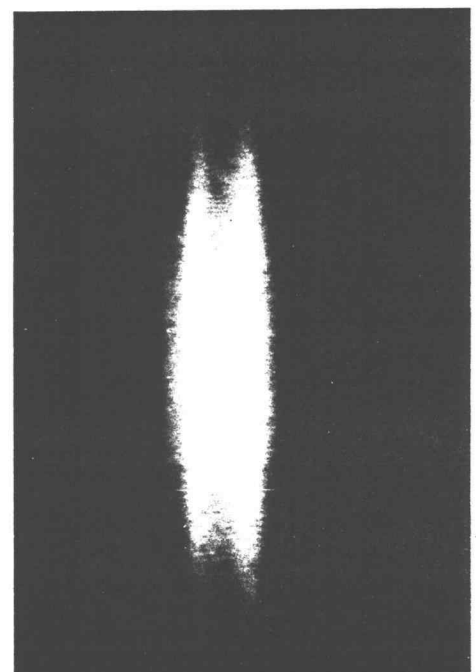
50 mA



70 mA



90 mA



120 mA

Figure 4.10: Photographs of the far field pattern of a 0.0 indium mole-fraction laser as various forward bias currents.

5. Gain Spectra Model

A model for the calculation of the spectral gain of pm-InGaAs diode lasers was constructed. This model included the strain perturbations to the band structure, of importance to laser operation, discussed in Chapter 2. The following is a detailed derivation of the expression used to calculate the spectral gain, and an outline of the program written to execute the calculation. The Fortran source code for the gain spectra model is listed in the appendix.

5.a. Derivation of the Spectral Gain Expression

The derivation of the expression for spectral gain follows closely that given in Reference [2] Chapter 3 modified to include the quantum and strain effects described previously. The interaction Hamiltonian between the light and the electronic sub-band structure is assumed to be in the dipole limit and use was made of Fermi's Golden Rule to calculate the transition matrix element which characterizes the strength of the interaction.

The first step starts with a rate equation analysis in which the interaction between light and the solid is described in terms of the Einstein absorption coefficient, B_{12} . Calculation of B_{12} involves evaluation of the transition matrix element. This is done in equations 5.3-5.15. Subsequently, all the transitions within the Brillouin zone which yield the same energy are summed together, equations 5.16-5.18, and the final result is given in Equation 5.19.

The calculation of spectral gain is exactly analogous to the calculation of spectral absorption $\alpha(\hbar\omega_{12})$ as gain is the negative of absorption. The calculation of $\alpha(\hbar\omega_{12})$ starts with the equation for absorption in a two level system as shown in Equation 5.1.

$$\alpha(\hbar\omega_{12}) = B_{12} (f_1 - f_2) n_g (c_0)^{-1} \quad (5.1)$$

where B_{12} : Einstein absorption coefficient
 f_1 : occupancy of the first state
 f_2 : occupancy of the second state
 n_g : group index of refraction
 c_0 : speed of light in vacuum

The semiconductor bands are modeled as the superposition of closely spaced discrete levels, this allows the expression in Equation 5.1 to be summed over all the transitions in the semiconductor which yield the correct transition energy, as shown in Equation 5.2. The transition matrix element is embodied in B_{12} , the Einstein absorption coefficient, which needs to be evaluated for the particular case of strained quantum well sub-bands. This is done via a rate equation analysis[2], the result of which is shown in Equation 5.3.

$$\alpha(\hbar\omega_{12}) = \sum_{c,v} B_{12} (f_v - f_c) n_g (c_0)^{-1} \delta(E_{c,v} - \hbar\omega_{12}) \quad (5.2)$$

where f_v : occupancy of the valence band states
 f_c : occupancy of the conduction band states

M_{cv} is related to the transition dipole moment, R_{cv} , by Equation 5.4 where R_{cv} is defined in Equation 5.5. R_{cv} can be evaluated if the initial and final state wavefunctions are known. The form of the wavefunctions used is shown in Equation 5.6. Each quantum well state is defined by an envelope function in the z direction and plane wave in the x and y directions times a Bloch function as given by Kane[28].

$$B_{12} = \frac{\pi q^2 \hbar}{m_0^2 \epsilon_0 n_g^2 \hbar \omega} \langle | M_{cn,vm} |^2 \rangle \quad (5.3)$$

where $\langle \rangle$: average over constant energy surface
 $M_{cn,vm}$: transition matrix element
 q : electronic charge
 m_0 : electron rest mass
 ϵ_0 : permittivity of free space
 \hbar : reduced Planck's constant
 ω : frequency of the light

$$M_{cn,vm} = \bar{R}_{cn,vm} \cdot \hat{e}_\nu \quad (5.4)$$

where $\bar{R}_{cn,vm}$: transition dipole moment
 \hat{e}_ν : photon electric field direction

$$\bar{R}_{cn,vm} = \int \Psi_{vn}^*(r) (-i\hbar\nabla) \Psi_{cm}(r) dr \quad (5.5)$$

where Ψ_{vn} : valence band wavefunction
 Ψ_{cm} : conduction band wavefunction

$$\Psi_{B,n,k(x,y)} = u_B(\bar{k}) \exp \left[i\bar{k}_{(x,y)} \cdot \bar{r}_{(x,y)} \right] \Phi_{B,n}(z) \quad (5.6)$$

where B : band (conduction, heavy hole or light hole)
 u_B : Bloch function associated with band B
 $\bar{k}_{(x,y)}$: in-plane wave vector
 $\bar{r}_{(x,y)}$: in-plane direction
 $\Phi_{B,n}(z)$: envelope function in the z direction

$$\begin{aligned}\bar{R}_{cn,vm} &= \delta_{kc(x,y),kv(x,y)} \left[\int \Phi_{c,n}(z) \Phi_{v,m}(z) dz \right] \bar{R}_{bulk} \\ &= \delta_{kc(x,y),kv(x,y)} C_{n,m} \bar{R}_{bulk}\end{aligned}\quad (5.7)$$

where \bar{R}_{bulk} : bulk material dipole moment

$$B_{12} = \frac{\pi q^2 \hbar}{m_0^2 \epsilon_0 n_g^2 \hbar \omega} \langle | (\delta_{kc(x,y),kv(x,y)} C_{n,m} \bar{R}_{bulk}) \cdot \hat{e}_y |^2 \rangle \quad (5.8)$$

Using the wavefunctions described in Equation 5.6, R_{cv} can be shown to be of the form given in Equation 5.7. Combining Equations 5.3-5.7 B_{12} is given by Equation 5.8.

At a later step in the derivation contributions to the absorption from all the transitions which yield the same energy will be summed together. All these transitions have different \bar{K} and therefore the strength of the interaction from each is different. To ease the evaluation of this sum the average of the projected dipole moment is taken over surfaces of constant transition energy. This partially removes the dipole moment dependence upon the angle of the \bar{K} of the transition and allows contributions from all the transition pairs of constant energy to be summed together with equal weight. Constant energy surfaces in quantum well sub-bands can be represented by circles, centered around the K_z axis, which lie on the planes of selected states allowed by the quantum confinement. One of these contours is diagrammed in Figure 5.1.

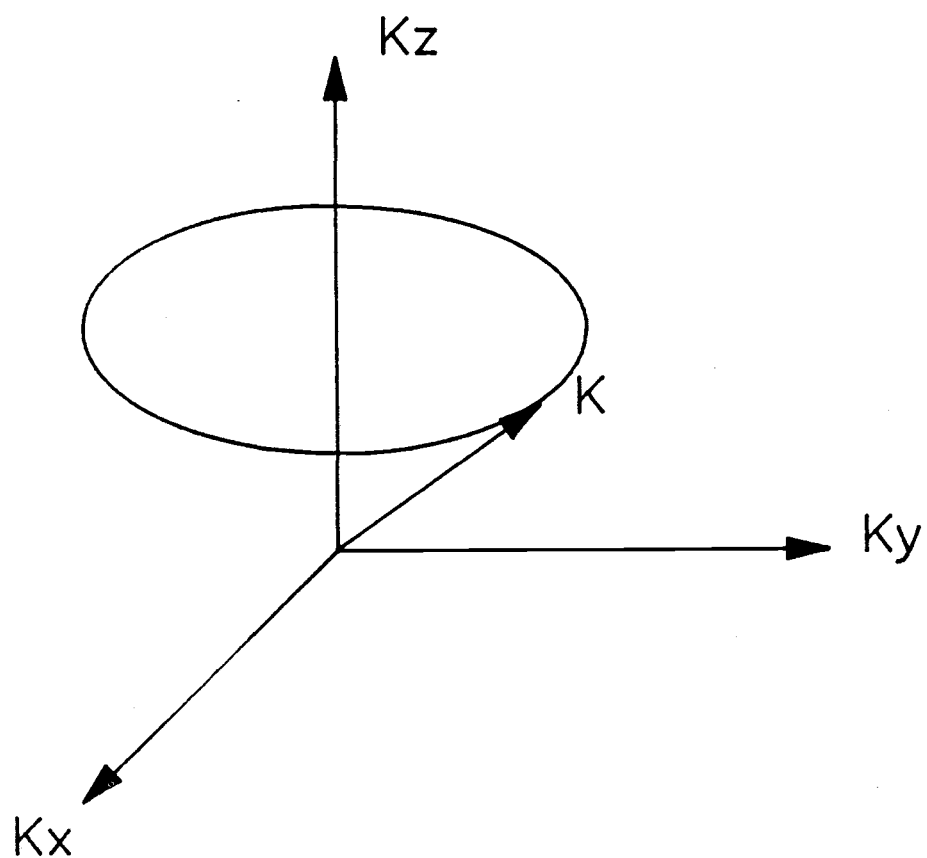


Figure 5.1: Constant energy surface of a quantum well sub-band. The circle lies on one of the planes of allowed states.

R_{bulk} is the dipole moment associated with bulk material and can be calculated from the Bloch part of the wavefunction. The Bloch functions for the various bands at $K=0$, as given by Kane[28], have the form given in Equation 5.9. The wavefunctions associated with an

$$\begin{aligned}
 \text{conduction: } & | S' \rangle \\
 \text{heavy hole: } & \sqrt{(1/2)} | X'+iY' \rangle \\
 \text{light hole: } & \sqrt{(1/6)} | X'-iY' \rangle + \sqrt{(4/3)} | Z' \rangle
 \end{aligned} \tag{5.9}$$

$$\begin{array}{l}
 | S' \rangle \\
 | X'+iY' \rangle \\
 | X'-iY' \rangle \\
 | Z' \rangle
 \end{array}
 =
 \begin{array}{c}
 \left| \begin{array}{cccc}
 1 & 0 & 0 & 0 \\
 0 & \cos\theta\cos\phi & \cos\theta\sin\phi & -\sin\theta \\
 0 & -\sin\theta & \cos\phi & 0 \\
 0 & \sin\theta\cos\phi & \sin\theta\sin\phi & \cos\theta
 \end{array} \right.
 \begin{array}{l}
 | S \rangle \\
 | X+iY \rangle \\
 | X-iY \rangle \\
 | Z \rangle
 \end{array}
 \end{array} \tag{5.10}$$

arbitrary \bar{K} (primed) are formed from those defined in respect to the crystal coordinate system (unprimed) by Equation 5.10. The coordinate system used to define θ and ϕ is diagrammed in Figure 5.2. The z direction is the direction of the photon electric field for TM polarization and the x direction is the photon electric field direction for TE polarization.

The TE projection of the heavy hole wavefunction, for a state with arbitrary K direction, is given in Equation 5.11. The average of this projection around the constant energy circle is shown in Equation 5.12. Evaluation of this integral and the analogous one for the light hole projection in the TE direction, yields Equation 5.13.

$$| X'+iY' \rangle_x = (\cos\theta\sin\phi + i\cos\theta) | X \rangle \tag{5.11}$$

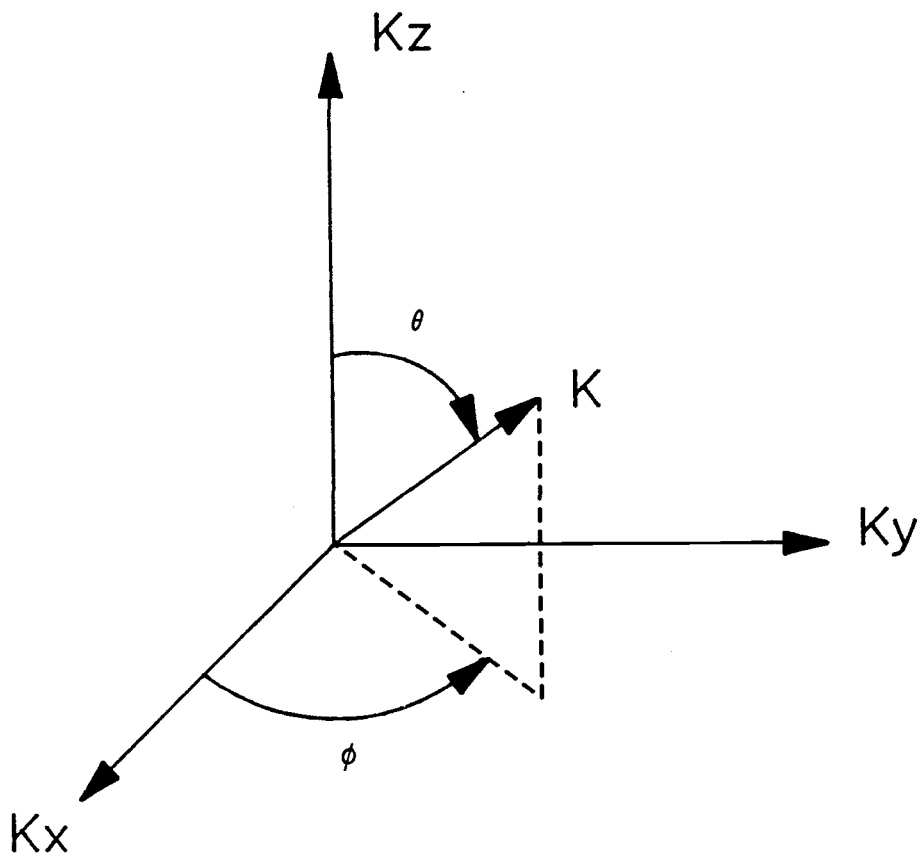


Figure 5.2: The coordinate system defining an arbitrary \bar{K} .

$$\frac{R^2}{2\pi} \int_0^{2\pi} (\cos^2\theta \sin^2\phi + \cos^2\phi) d\phi \quad (5.12)$$

where R : magnitude of \bar{R}_{bulk}

$$\text{Heavy hole:} \quad \frac{1}{2} R^2 (\cos^2\theta + 1) \quad (5.13a)$$

$$\text{Light hole:} \quad \frac{1}{6} R^2 (4\sin\theta\cos\theta + 5 - 3\cos^2\theta) \quad (5.13b)$$

The trigonometric terms in Equations 5.13a and 5.13b are called the anisotropy of the transition A_{nm} and impart a significant energy dependence to the transition strength. R is the bulk material transition dipole moment which is related to measured material parameters by Equation 5.14[28].

$$R^2 = \frac{m_0^2 E_g (E_g + \Delta)}{4 m_e (E_g + (\frac{2}{3})\Delta)} \quad (5.14)$$

where E_g : material band-gap
 Δ : spin-orbit splitting
 m_e : conduction band effective mass

For materials such as GaAs in which the band gap is fairly wide and, therefore, the band mixing as a function of \bar{K} weak, it is a reasonable assumption that the bulk dipole moment calculated at $K=0$ is a good approximation to the bulk matrix element for \bar{K} around $K=0$ [44]. This implies that the bulk matrix element can be assumed energy independent.

Applying Equations 5.9-5.14 to Equation 5.8 yields the final expression for B_{12} .

$$B_{12} = \frac{\pi q^2 \hbar}{m_0^2 \epsilon_0 n_g^2 \hbar \omega} \delta_{kc(x,y),kv(x,y)} C_{n,m}^2 R^2 A_{nm} \quad (5.15)$$

The expression for spectral absorption, including the terms introduced in Equations 5.3-5.15 is:

$$\alpha(\hbar\omega_{cv}) = \sum_K \frac{\pi q^2 \hbar}{m_0^2 \epsilon_0 n_g^2 \hbar \omega} \delta_{kc(x,y),kv(x,y)} C_{n,m}^2 R^2 A_{nm} (f_v - f_c) n_g \times (c_0)^{-1} \delta(E_{c,v} - \hbar\omega_{12}) \quad (5.16)$$

The summation over the Brillouin Zone is most easily evaluated by converting it to a summation (over sub-band index) of integrals in K_{xy} . Since the constant energy surfaces associated with quantum well sub-bands are circular this is most easily done in cylindrical coordinates. The cylindrical volume element is defined in Figure 5.3. The summation is only done over positive K_z as the envelope function defining the localization uses the boundary condition that it is zero at the edges of the sample[45].

The result of this procedure is shown in Equation 5.17. The indices of the summation are over all the allowed sub-bands. A separate summation is done over each of the valence bands. This expression is difficult to evaluate since the integral is over K_{xy} but the expression is calculated over the transition energy, $\hbar\omega_{12}$. The expression given in Equation 5.17 is converted to an integral in energy to circumvent this problem. This expression is given in

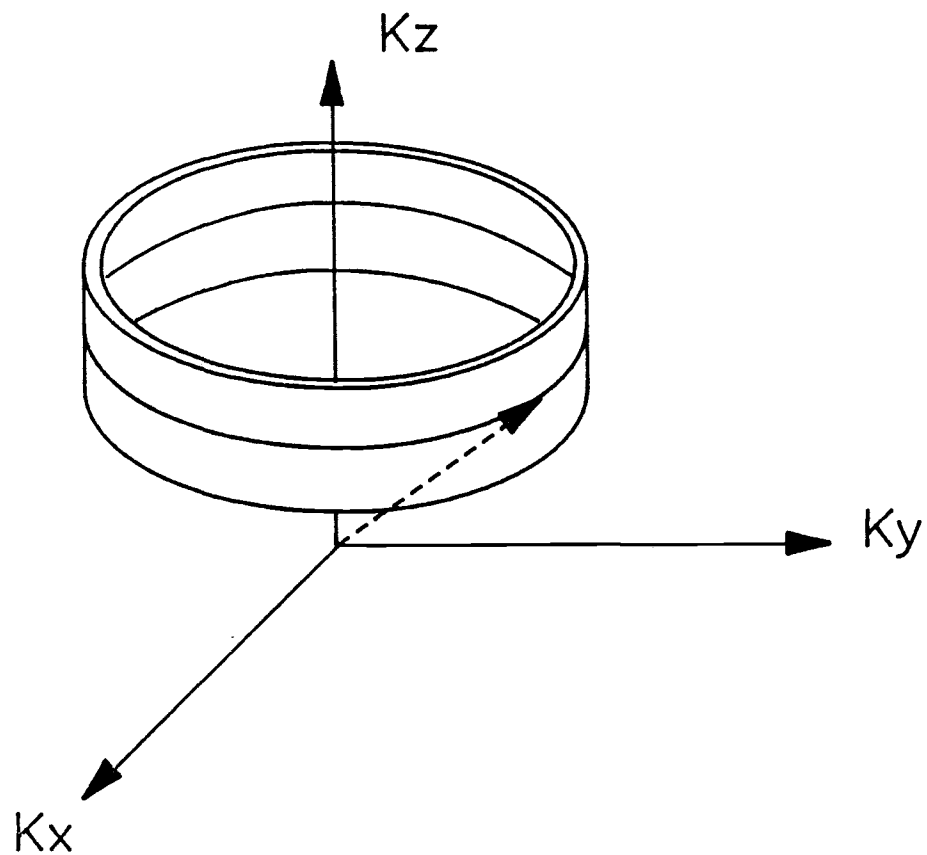


Figure 5.3: The cylindrical volume element used in the integration over K_{xy} . The cylinder occupies a volume half the distance between the sheets of states associated with the adjacent sub-bands.

$$\alpha(\hbar\omega_{cv}) = \sum_{hh, lh} \sum_{n, m} \int \frac{\pi q^2 \hbar}{m_0^2 \epsilon_0 n_g^2 \hbar \omega} \delta_{kc(x,y), kv(x,y)} C_{n,m}^2 R^2 A_{nm} (f_v - f_c) \times n_g (c_0)^{-1} \delta(E_{c,v} - \hbar\omega_{12}) \frac{\bar{k}_{(x,y)}}{\pi L_{z,eff}} d\bar{k}_{(x,y)} \quad (5.17)$$

where $L_{z,eff}$: effective well width

Equation 5.18. The integral is easily evaluated since there is only one K_{xy} which is a simultaneous solution of both the energy and momentum selection delta functions. Equation 5.18 then simplifies to Equation 5.19 which was the one numerically evaluated in the

$$\alpha(\hbar\omega_{cv}) = \frac{\pi q^2}{m_0^2 \epsilon_0 n_g \hbar c E} \sum_{hh, lh} \sum_{n, m} m_{r, nm} \int \delta_{kc(x,y), kv(x,y)} C_{n,m}^2 \times R^2 A_{nm} (L_{z,eff})^{-1} (f_v - f_c) (c_0)^{-1} \delta(E_{c,v} - \hbar\omega_{12}) dE_{nm} \quad (5.18)$$

where $m_{r, nm}$: reduced mass of the transition
 E : energy of the transition
 E_{nm} : energy in the bands

$$\alpha(\hbar\omega_{cv}) = \frac{q R^2}{m_0^2 \epsilon_0 n_g c_0 E \hbar} \sum_{hh, lh} \sum_n m_{r, n} A_n(E') \left[f_v(E'') - f_c(E''') \right] \times (L_{eff, n})^{-1} \quad (5.19)$$

where E' : energy up the conduction band
 E'' : energy up the conduction band - $E_{Fermi, c}$
 E''' : energy up the valence band - $E_{Fermi, v}$

calculation of the gain spectra. The effective width of the quantum well, $L_{z,eff}$, was left within the summation in Equation 5.19. This term is evaluated separately for each sub-band level and is slightly larger than the metallurgical well width due to evanescent tails of the envelope functions which extend into the cladding layers.

This expression is only strictly valid for transitions which have the same sub-band quantum number, in the infinite quantum well limit. This is due to the fact that the anisotropy of the transition, A_{nm} , is defined by the total \bar{K} of the transition pair. In the case of a finite well or in transitions between bands of different sub-band quantum number, the electron and hole state may differ significantly in K_z . This makes evaluation of A_{nm} impossible as it was defined in this model and $L_{z,eff}$ different for conduction band states and valence band states with the same sub-band index. The differences in K_z between conduction and valence sub-bands which have the same sub-band quantum number are assumed small enough in the case of the finite well such that this expression is still valid. This in effect constrains us to evaluate only those transitions for which $n=m$, which is reasonable as the overlap integral between the envelope functions of states in which n does not equal m would be small.

Strain effects did not alter the above derivation from that of an unstrained quantum well. The strain effects introduced into the numerical model were the first order rigid shifts in the band positions[19], and alteration of the the band edge effective masses calculated in the large strain limit[25]. Mixing of the light hole with the spin split states would affect the matrix element associated with light hole transitions but this is assumed unimportant as the

light hole sub-bands split down from the band edge quickly as the indium mole-fraction is increased.

The assumption of a parabolic dispersion relationship in the valence band is weak, especially for low indium mole-fraction structures. The band mixing associated with the quantum confinement alone makes the valence sub-bands highly non-parabolic, and inclusion of these effects into gain spectra models tends to increase the predicted excitation necessary to achieve threshold[63]. Dispersion relationships for strained quantum well structures have recently been published[64],[65] and a more accurate assessment of the spectral gain could be extracted from these relationships at the expense of having to sum contributions from all points in the Brillouin zone numerically.

5.b. Design of the Program

The Fortran program developed for this calculation was modeled after the work of Chinn, et. al.[34], and has the following form:

- a. Calculation of the material composition variation with distance,
- b. Extraction of the conduction band potential from the composition variation,
- c. Calculation of the conduction sub-band energies from the conduction band potential,
- d. Extraction of the heavy hole potential from the composition variation,
- e. Calculation of the heavy hole sub-band energies from the heavy hole potential,
- f. Extraction of the light hole band potential from the composition variation,
- g. Calculation of the light hole sub-band energies from the light hole potential,

- h. Calculation of the quasi-Fermi level positions for the conduction and valence bands for the assumed carrier densities,
- i. Calculation of the infinite scattering time gain spectrum using c, e, g, and h,
- j. Convolution of the infinite scattering time gain spectrum with an assumed Lorentzian function.

The material composition variation with distance was calculated by simulating the temperature profiles which the MBE source ovens were programmed to follow. The calibration data from one of the growth runs was used to associate the oven fluxes to the oven temperatures. The fluxes were assumed to vary exponentially with temperature between the calibrated temperatures. The oven temperature profile was then simulated at the desired spatial resolution and the composition profile extracted from the calculated oven temperatures. The composition profile calculated in this way is shown in Figure 5.4. This composition profile was then used to determine the potentials which confine the electrons and holes in the laser.

The potential confining the electrons in the conduction band or the holes in the valence band is a superposition of the band edge profile, the built-in field of the p-n junction, the applied bias and the Hartree contribution associated with the high excess carrier density. In the model it was assumed that the built-in potential was canceled by the applied bias. Also the number of electrons and holes in the active region is the same, and their envelope functions are similar so the Hartree potential is assumed small. This leaves only the band edge potential, at flat band, confining the carriers.

The band edge potential can be extracted from the composition

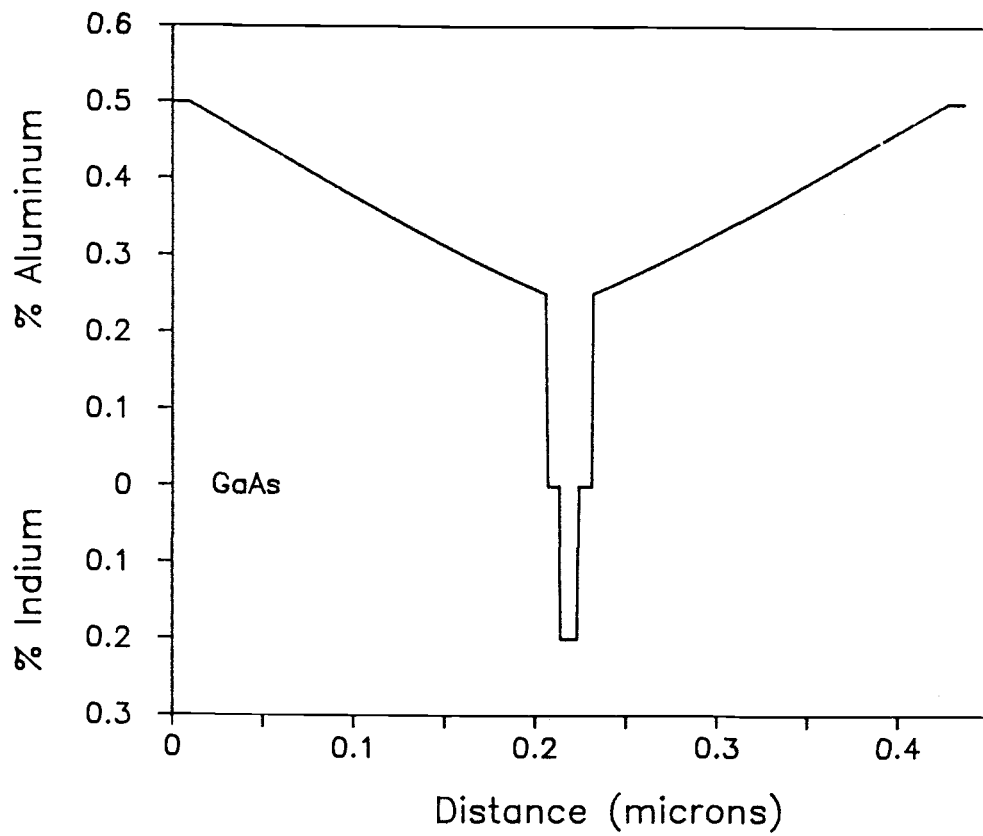


Figure 5.4: The modeled composition profile for the 0.20 indium mole-fraction GRIN-SCH laser calculated from the calibration data.

variation if two things are known: the band gap variation with composition, and the relative band alignments. The band gap variation with composition for both $\text{Al}_x\text{Ga}_{1-x}\text{As}$ [46] and unstrained $\text{In}_y\text{Ga}_{1-y}\text{As}$ [47] are given in Equations 5.20a and 5.20b. The relative band alignments for the GaAs/AlGaAs heterojunction system are fairly well established. The valence band offset, Q_v , is 67% of the band gap difference between the constituent materials[48]. The conduction band offset, Q_c , is $1-Q_v$. The potential was calculated by applying Equation 5.21, on a point by point basis to the composition file.

The band alignment in the InGaAs/GaAs system is not as well characterized as that of the GaAs/AlGaAs system. The influence that strain has on the band alignments is also not well known. The value for band offset used in this work was derived by Menendez, *et al.*, [49]. This work yielded $Q_c=0.4dE_{gh}$ (E_{gh} is the heavy hole band

$$E_{g,\text{AlGaAs}}(x) = E_{g,\text{GaAs}} + 1.237 x \quad (5.20a)$$

$$E_{g,\text{InGaAs}}(y) = E_{g,\text{GaAs}} - 1.47 y + .375 y^2 \quad (5.20b)$$

where

x:	aluminum mole-fraction
y:	indium mole-fraction
$E_{g,\text{GaAs}}$:	GaAs band-gap (1.424 eV @ 300° K)
$E_{g,\text{AlGaAs}}$:	direct AlGaAs band-gap
$E_{g,\text{InGaAs}}$:	InGaAs band-gap

$$V(z) = Q_B (E_{g,\text{AlGaAs}} - E_{g,\text{GaAs}}) \quad (5.21)$$

where

$V(z)$:	band potential
Q_B :	band offset

gap) but other researchers have reported values as high as $Q_c=0.85$ [50],[51]. Luckily the gain spectra position is not sensitive to the band offset used, the spectra for 0.20 mole-fraction indium shifts only 6 meV if $Q_c=0.85dE_{gh}$ is used instead of $Q_c=0.4dE_{gh}$.

The alignment of the bands for a given indium concentration was done by calculating the position of the heavy and light hole bands in respect to the conduction band edge, including the hydrostatic and shear deformation contributions described in Chapter 2. This fixed the relative position of the conduction band edges and with them the relative positions of the valence bands. The band alignments as a function of indium concentration calculated using this method are shown in Figure 5.5.

The spatial potential variation for each of the bands (conduction, heavy hole or light hole) was extracted by application of the above procedure to the spatial composition variation. The result of this procedure for a 100 Å, $In_{.2}Ga_{.8}As$, quantum well is shown in Figure 5.6.

The energy positions of the sub-bands are found by solving the one dimensional time independent Schroedinger equation, using the appropriate band edge potential. The solutions were found iteratively using the "Numerov" method[52]. This method calculates the envelope functions as well as the sub-band energies. The envelope functions of the first conduction sub-band, for the potential shown in Figure 5.6, is shown in Figure 5.7. The specified number of sub-band energies for all three bands were calculated using this method.

Once the sub-band energies were known, the quasi-Fermi levels associated with the particular carrier densities were calculated.

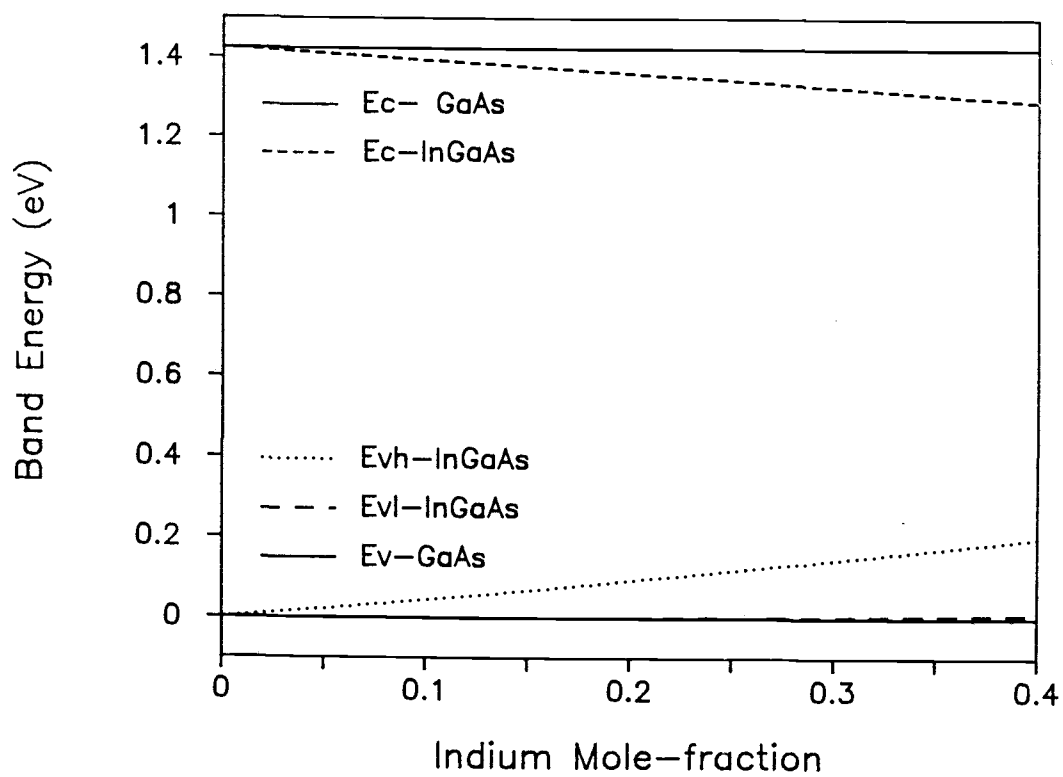


Figure 5.5: The relative band alignments for the GaAs/InGaAs system calculated using $Q_c = .4dE_{gh}$.

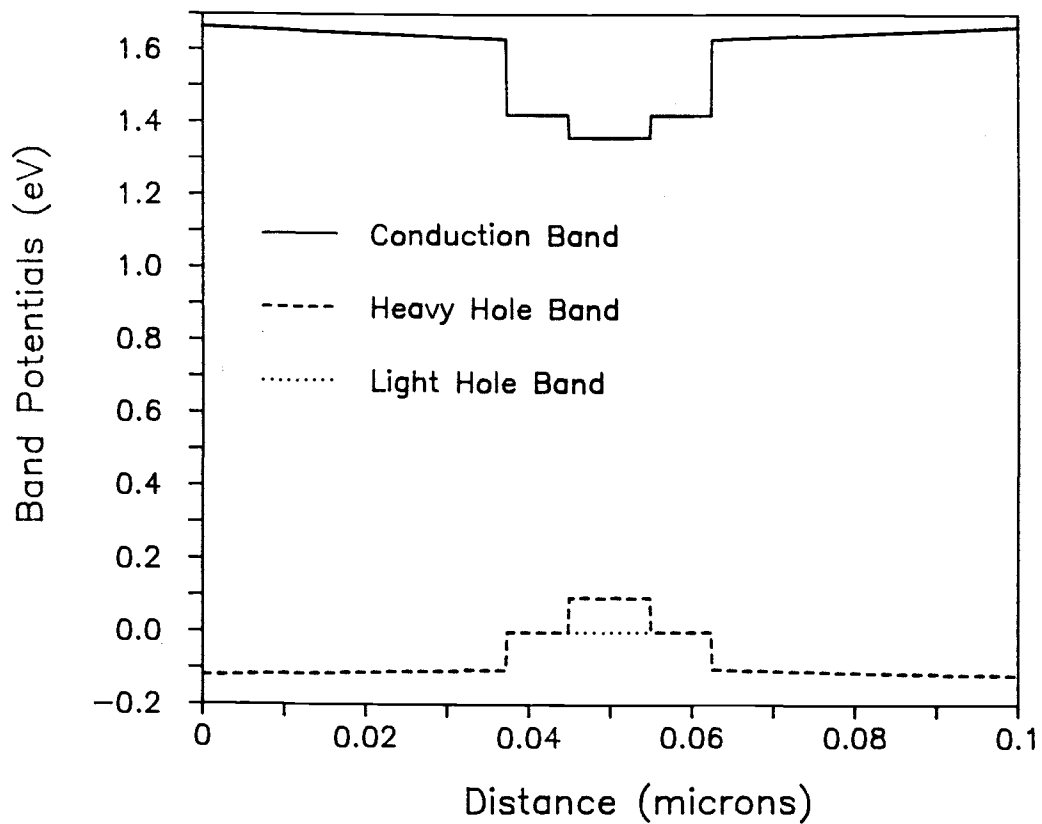


Figure 5.6: The band potentials derived for a 100 Å, In₂Ga_{0.8}As GRIN-SCH laser structure.

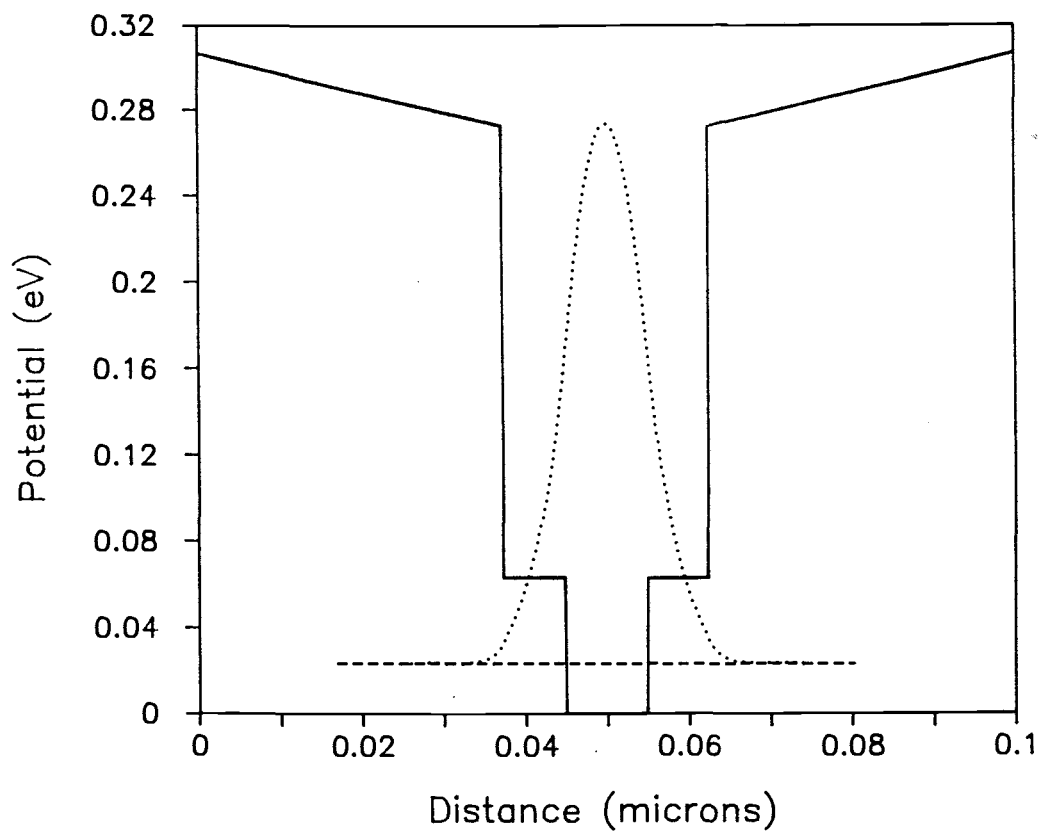


Figure 5.7: The envelope function (dots) of the first conduction sub-band associated with the potential shown in Figure 5.6. The solid line is the band potential and the dashed line is the relative energy level position in respect to the potential.

$$n = \sum_j K T \rho_j \ln \left[1 + \exp \left[(E_f - E_j) / K T \right] \right] \quad (5.22)$$

where

n:	carrier density (electrons or holes)
K:	Boltzmann's constant
T:	temperature in Kelvin
ρ_j :	two dimensional density of states
E_f :	Fermi energy
E_j :	ground state energy of sub-band j
j:	sub-band index

This calculation was done by assuming a two dimensional sheet carrier density (equal numbers of electrons and holes) and numerically solving Equation 5.22. Evaluation of the spectral absorption was then accomplished by indexing through each sub-band pair (conduction-valence), summing the result of Equation 5.19 at all the transition energies of interest. Figure 5.8 shows the result of this procedure for the 100 Å, $\text{In}_{0.2}\text{Ga}_{0.8}\text{As}$ laser structure shown in Figure 5.8.

The sharp step in the spectra shown in Figure 5.8 is associated with the onset of contribution to the gain(loss) from higher energy sub-band transition pairs. Gain spectra at three sheet carrier densities are shown in Figure 5.8. At the lowest of the three carrier densities the material exhibits loss at all wavelengths above the band edge. At higher carrier density the gain changes sign in a small wavelength region; this is the material transparency carrier density. At still higher carrier densities the width of the material gain region and the magnitude of the peak gain both increase. A device will lase when the gain is high enough to offset the round trip loss in the cavity. These losses are device length dependent, but

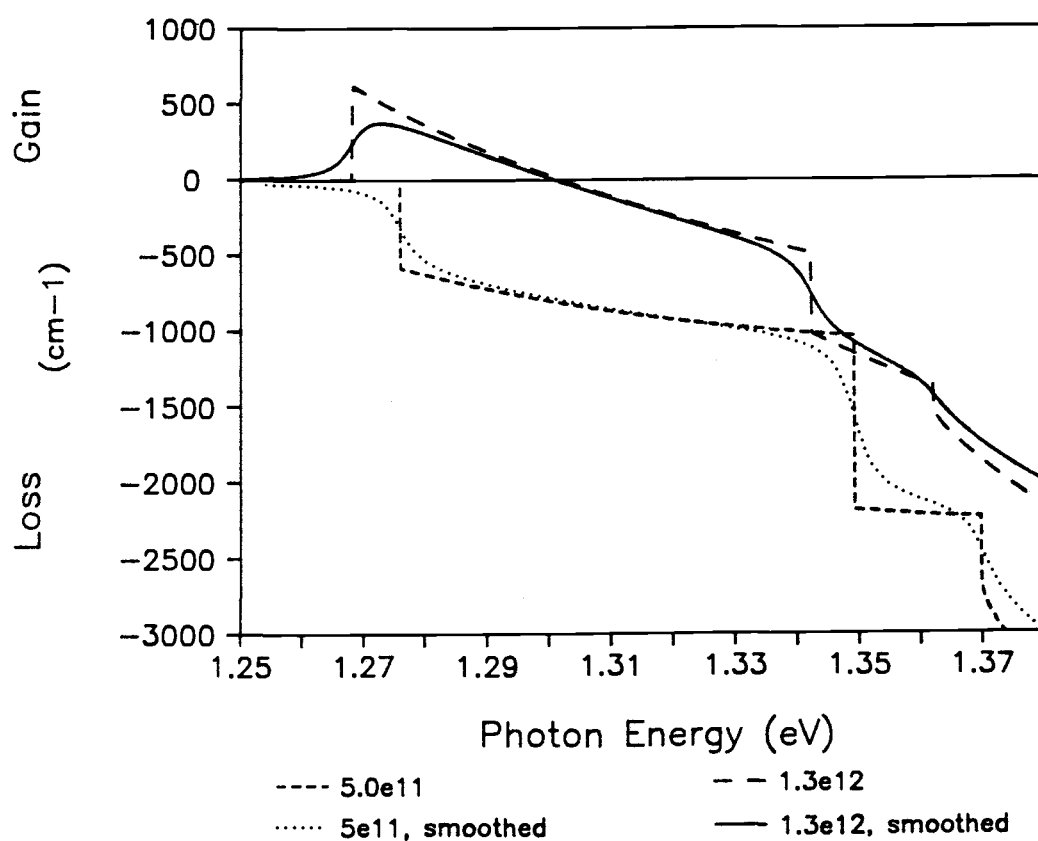


Figure 5.8: Calculated gain spectra for a 100 Å In₂Ga_{0.8}As GRIN-SCH laser diode. Calculated gain spectra at two sheet carrier densities (in units of cm⁻²), both with and without smoothing, are shown.

typically a material gain of 1000 cm^{-1} is sufficient for a 300 micron long device.

The sharp features shown in Figure 5.8 are not typically seen in measured gain spectra but rather a smooth variation in gain is observed[33]. The smoothing of the spectra is caused by scattering which imparts an uncertainty in the energy of a transition pair at a given \bar{k} . This is dealt with in the gain model by convolving the sharp spectra with a Lorentzian function, characterized by a scattering time typically associated with intercarrier scattering processes[33]. The form of the Lorentzian function used is given in Equation 5.23. The

$$\alpha_{\text{sm}}(\hbar\omega) = \int_0^{\infty} \alpha(\hbar\omega) \frac{(\hbar/\tau_{\text{sc}})}{(E_{\text{cv}} - \hbar\omega)^2 + (\hbar/\tau_{\text{sc}})^2} dE_{\text{cv}} \quad (5.23)$$

where τ_{sc} : scattering time
 E_{cv} : dummy variable for integration
 $\alpha_{\text{sm}}(\hbar\omega)$: smoothed absorption spectra

characteristic time used in the convolutions shown in Figure 5.8 was 250 fs. The intercarrier scattering time is best described as a function of carrier density, rather than a constant, but the appropriate relationship is unclear, so a carrier density invariant scattering time was used in all the simulation runs.

6. Discussion

6.a. Characterization of the Epitaxial Layers

The PL spectra from the test structure, Figure 4.2, shows that the critical concentration, for a layer thickness of 10 nm, is between 0.20 and 0.30 mole-fraction indium. This conclusion is drawn from the dramatic increase in emission line width of the 0.30 indium mole-fraction quantum well over that of the others. The relative brightness of the 0.30 indium mole-fraction peak is due to its proximity to the surface. It is closer to the surface than the others and therefore pumped much harder by the excitation laser than are the other ones.

The PL spectra from the actual laser epitaxial layers, Figure 4.3, show that the transition between narrow line width and broad line width also occurs between the 0.20 and 0.30 mole-fraction indium structures. The critical indium concentration at 10 nm, according to Matthews and Blakeslee is 0.28. Given the difficulties in the growth of these indium compounds there is considerable uncertainty in the final indium concentration[24]. These results confirm the Matthews-Blakeslee relationship, within the uncertainty with which the quantum well width and composition are known.

6.b. Device Performance

The 0.0, 0.10 and 0.20 mole-fraction indium devices achieved laser operation at room temperature. Of these only the 0.0 indium mole-fraction device could be operated continuous wave (CW). The 0.10 and 0.20 mole-fraction indium devices only operated in a pulse mode. The threshold current of a typical device from each of the device types was measured by extrapolation of the optical power-current (L-I)

Indium mole-fraction	I_{th} (mA)	J_{th} (mA/cm ²)
0.0	24	820
.10	68	2300
.20	88	3800

Table 6.1 Threshold currents and current densities of typical laser diodes.

curve in the lasing region back to $L=0$. This yields threshold current and threshold current densities as shown in Table 6.1. The higher threshold current density of the lasers containing indium in the active region is the reason the 0.10 and 0.20 indium mole fraction devices could only be operated pulsed at room temperature.

The increase in threshold current density has a number of possible explanations. The indium containing epitaxial layers were grown with a growth interruption in the active region while the GaAs/AlGaAs structure was not, as described in Chapter 3. The forward bias current required to achieve threshold in the laser is, in part, determined by the magnitude of the non-radiative recombination. Recombination through interface states which arose due to suspending growth would increase the non-radiative carrier loss. The stop growth procedure used also made it such that the AlGaAs cladding, on the surface side of the active region, was grown at low temperature, approximately 590° C. Growth of low temperature AlGaAs adjacent to the active region of a laser diode has previously been shown to give rise to increased threshold current density in GaAs/AlGaAs laser diodes.

The second possible explanation for this increase in threshold current density is that the addition of indium, even for thicknesses

under the critical thickness for the given mole-fraction indium, could cause an increase in the defect or dislocation density in active region. This would have the same effect as an increased surface recombination rate, as misfit dislocations have been reported to be active non-radiative recombination centers[16].

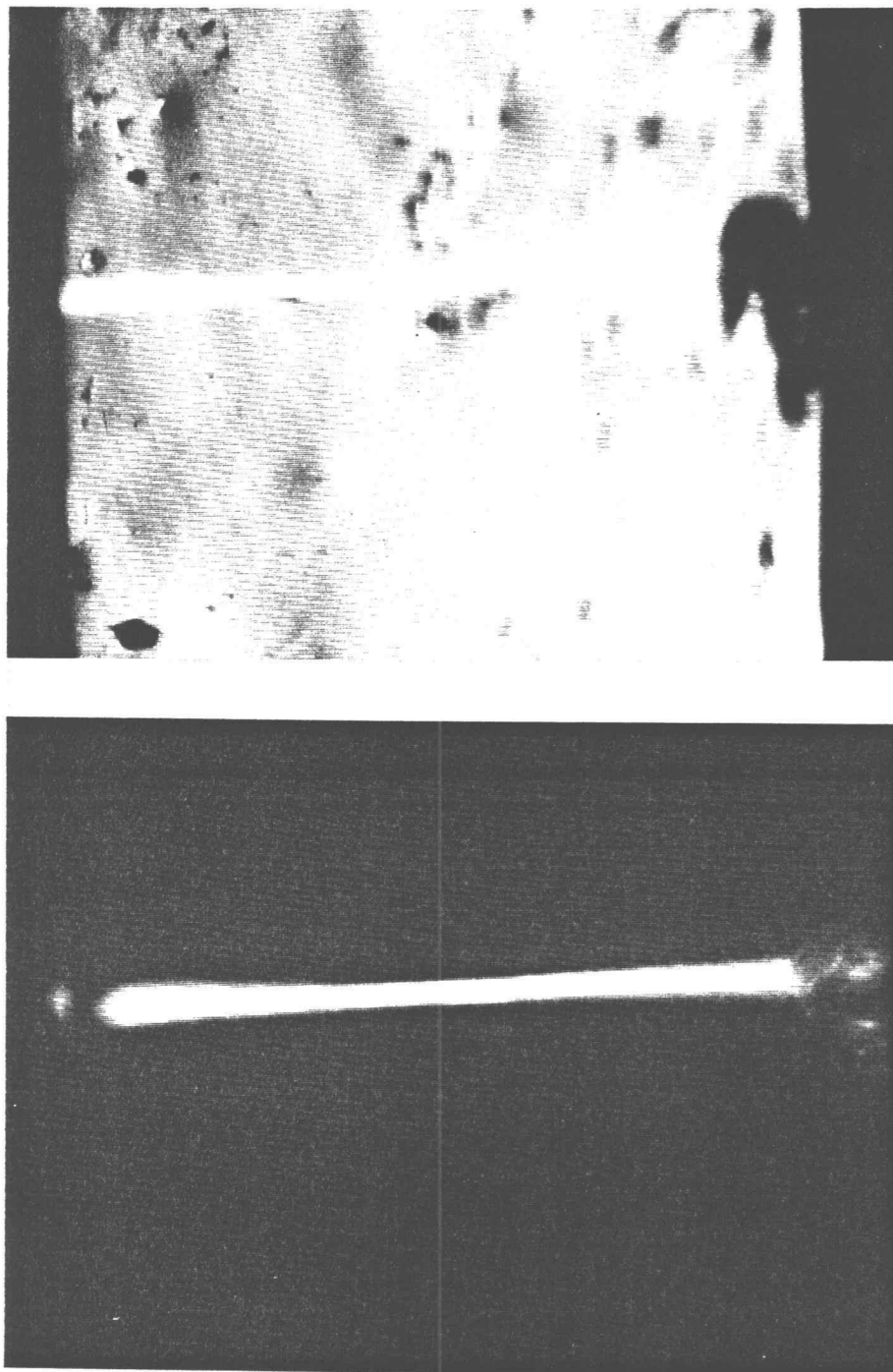
A third possible explanation arises from recent work by Sheih, et. al., [57]. This work described the performance of devices, similar to the .20 mole-fraction indium laser fabricated in this work, investigated as a function of active region width. The devices they measured showed an unexpected decrease in the threshold current, of identical length devices, as the stripe width was increased (from 150 mA for a 5 micron stripe width to 80 mA for a 50 micron stripe width). This anomalous behavior (GaAs/AlGaAs lasers show an increase in threshold current with stripe width) was proposed to arise from a high lateral optical loss in the device, the relative impact of which decreased with increasing stripe width. This increase in lateral optical loss was thought to arise from a higher lateral diffusivity in the InGaAs devices over that of the GaAs devices.

The increase in threshold current density, with the addition of indium to the active region of the laser, in the devices described in this thesis, could have arisen via any, or a combination of all of the above affects. An increase in the threshold current density due to the stop growth in the active region would have affected all the indium containing devices similarly. If this were the only effect the threshold current densities of the 0.10 and 0.20 mole-fraction indium lasers should have been the same, higher than the 0.0 mole-fraction indium device. The differences in the threshold current densities

measured for the 0.10 and 0.20 indium mole-fraction lasers can either be explained by an increase in the lateral optical loss[57] between the two indium mole-fraction devices or through differences in the non-radiative recombination, possibly through misfit dislocations.

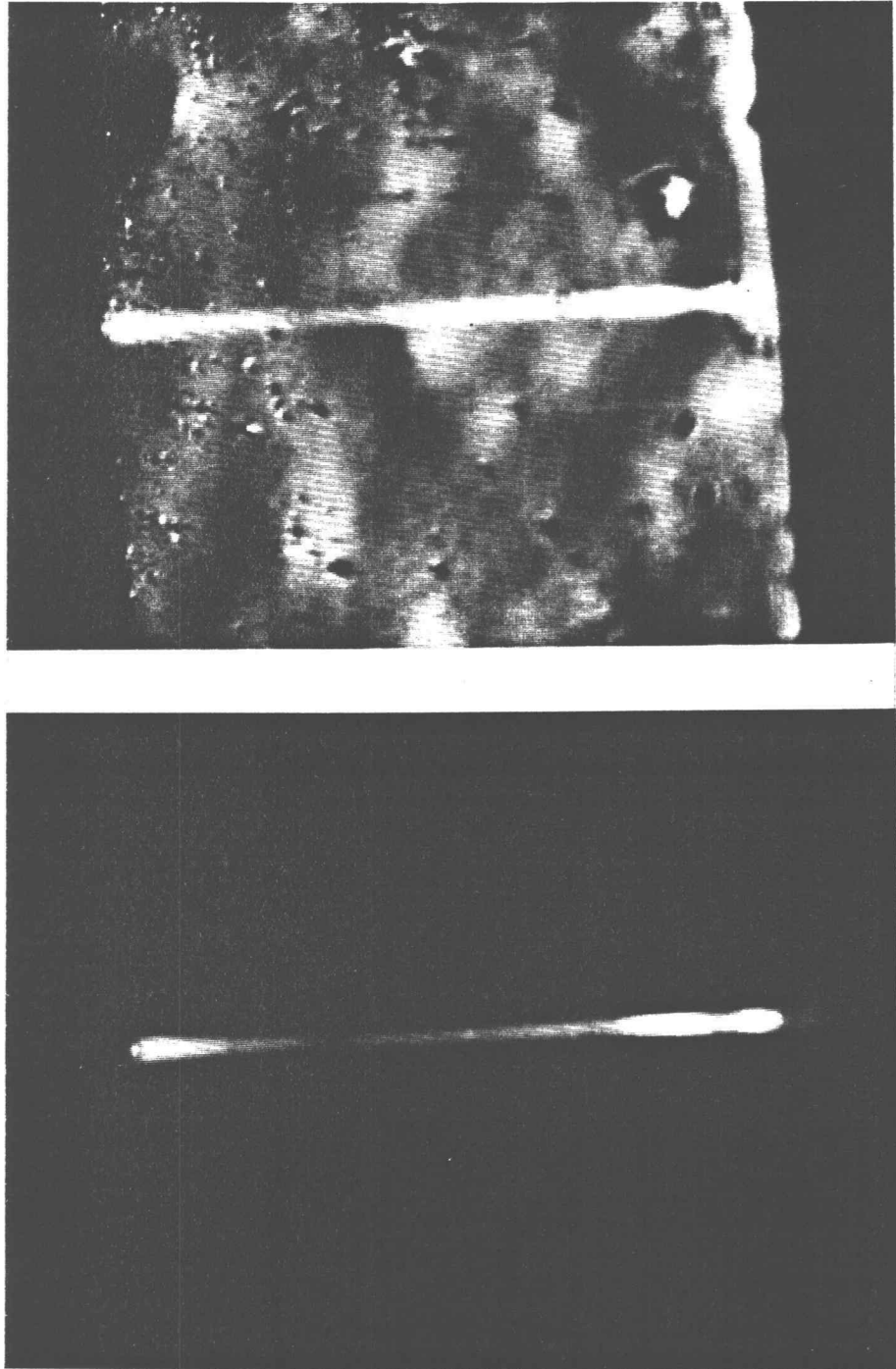
Misfit dislocations in the active region of a laser would affect the emission from the device by acting as a local carrier sink, due to their high non-radiative recombination rate. The effect on the spontaneous emission of the laser is to produce "dark lines" along the laser stripe due to the lower carrier density, within a diffusion length from the dislocation. Images of the spontaneous emission from fabricated devices containing 0.10 and 0.20 indium mole-fraction in the active region are shown in Figure 6.1. These images were obtained by packaging the devices upside-down and imaging the light emission through the substrate. It is fortuitous that the emission from the active region of the indium containing devices is at a lower energy than the GaAs substrate band gap and therefore not absorbed. The spontaneous emission along the stripe was imaged through a light microscope and detected via a solid-state silicon television camera, sensitive out to 1.1 microns wavelength.

The emission from the 0.20 indium mole-fraction device shows definite evidence of inhomogeneity in the spontaneous emission along the stripe. The 0.10 indium mole-fraction device is homogeneous. The non-uniformity in the 0.20 indium mole-fraction device could be caused either by non-uniform current flow (which in turn might be caused by variation in the contact resistance along the stripe) or by the presence of dislocations. Either of these effects would increase the threshold current density of the 0.20 over the 0.10 indium mole-



0.10 mole-fraction device.

Figure 6.1: Photographs of the spontaneous emission along the active region of the 0.10 mole-fraction indium, a., and 0.20 mole-fraction indium, b., devices.



0.20 mole-fraction device.

fraction device.

The spectral output of the different lasers was shown in Figure 4.6 to Figure 4.8. The sharp structure in the sub-threshold spectra of all the lasers are the longitudinal modes of the Fabry-Perot cavity. The sub-threshold spectra of the 0.20 indium mole-fraction laser, shown in Figure 4.8, shows an anomalous modulation to the longitudinal mode amplitude. This additional modulation is thought to be due to the dark line structures seen in the spontaneous emission of other devices from the same epitaxial growth. A perturbation to the index of refraction along the length of the cavity, as could occur at a dislocation, could create a standing wave which would interfere with the Fabry-Perot resonance. Different devices have been observed with different anomalous modulation periods, which could arise from different positions of the index perturbation in the cavity.

The Fabry-Perot resonances in the sub-threshold modulation can be used to extract the net gain of the laser as a function of wavelength[58]. This was done for the 0.0, 0.10 and 0.20 indium mole-fraction lasers and the results shown are in Figure 6.2 to Figure 6.4, respectively. The expression for net cavity gain as a function of the longitudinal mode peaks and valleys is given by the Equation 6.1. The cavity gain for the 0.0 and 0.10 mole-fraction indium devices is extracted at three forward bias currents. These spectra show the evolution of the gain from fairly flat at low bias current to peaked at threshold. At biases higher than threshold, the spectra are difficult to measure as there are orders of magnitude intensity differences between the Fabry-Perot resonances and anti-resonances.

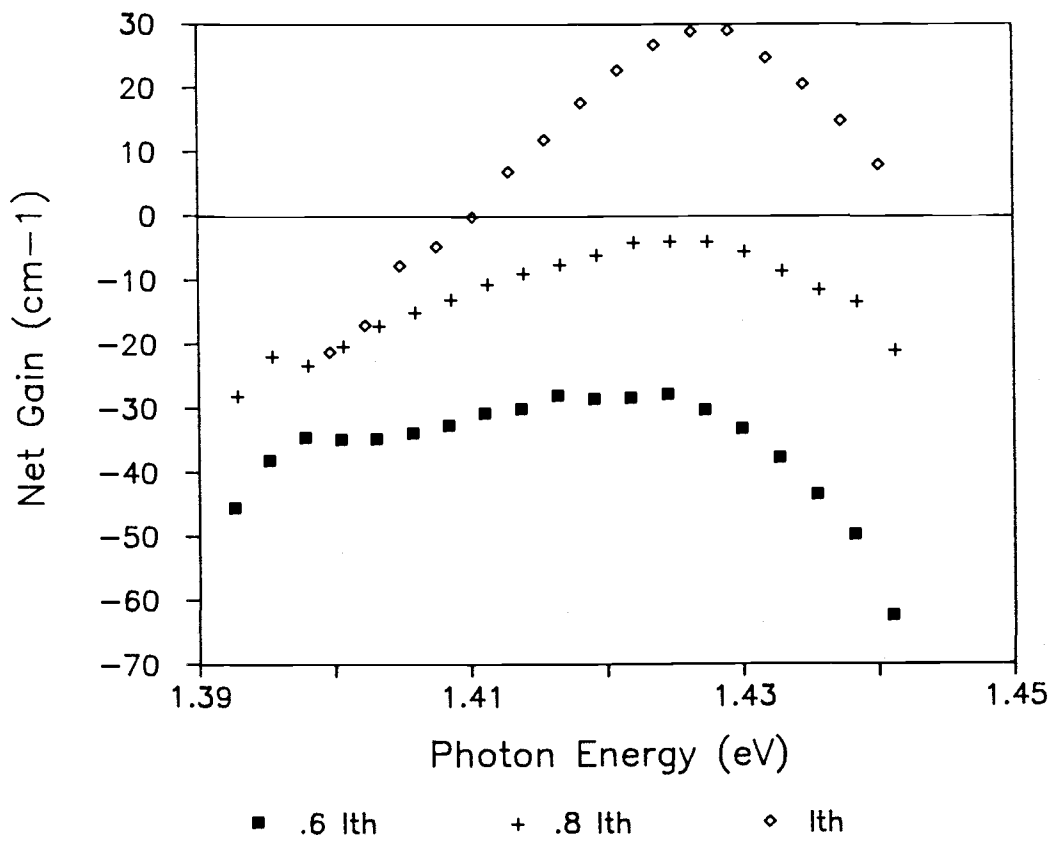


Figure 6.2: Extracted gain spectra as a function of photon energy for the 0.0 indium mole-fraction laser at various forward bias currents.

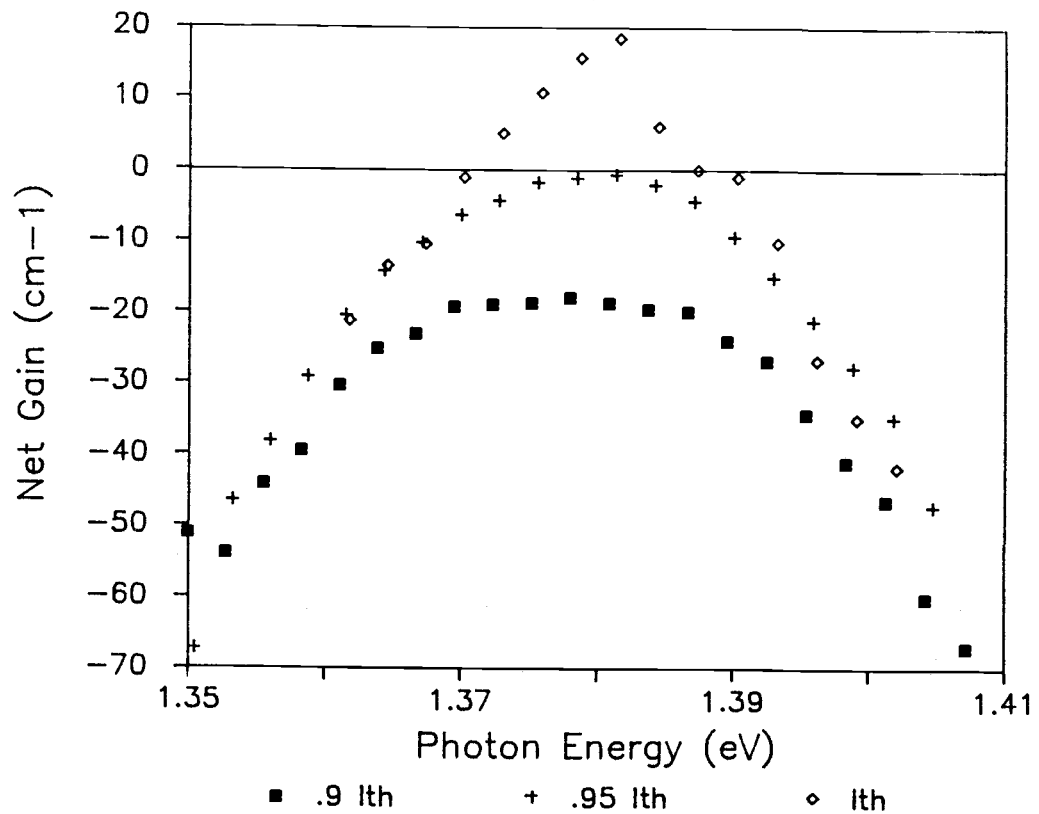


Figure 6.3: Extracted gain spectra as a function of photon energy for the 0.10 indium mole-fraction laser at various forward bias currents.

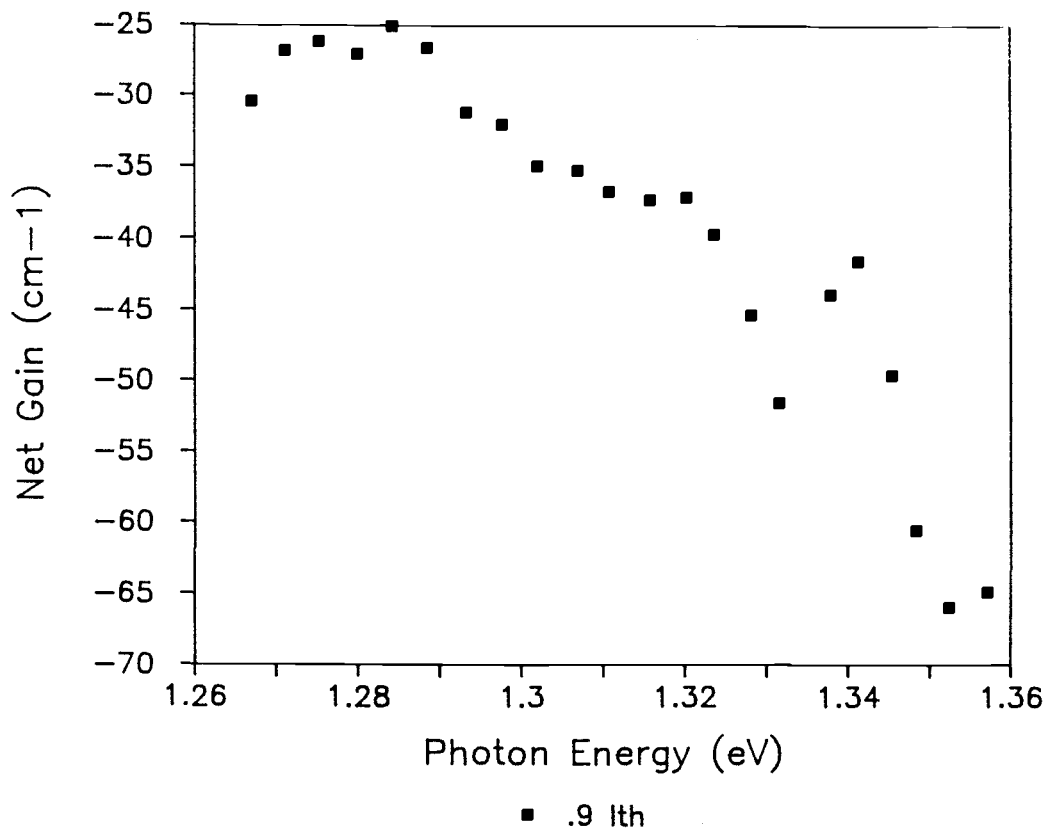


Figure 6.4: Extracted gain spectra as a function of photon energy for the 0.20 indium mole-fraction laser at various forward bias currents.

$$\begin{aligned}
 G_{\text{net}} &= \Gamma G_{\text{mat}} - \alpha_i \\
 &= -(L^{-1}) (\ln(E_{\text{mod}}^{-1}) + \ln(R)) \quad (6.1)
 \end{aligned}$$

where $E_{\text{mod}} = (E_{\text{peak}} - E_{\text{valley}}) / (E_{\text{peak}} + E_{\text{valley}})$

G_{net} : net cavity gain
 G_{mat} : material gain
 Γ : optical confinement factor[66]
 L : cavity length
 α_i : distributed optical losses
 R : facet reflectivity
 E : photon electric field amplitude

The gain spectra for the 0.20 indium mole-fraction device was only extracted at one bias current. This limitation was due to the anomalous modulation, discussed above, which made accurate measurement of the Fabry-Perot resonance and anti-resonance intensities difficult. The majority of the devices at this indium mole-fraction lased at an energy of 1.27 eV, corresponding to the peak at the left of the extracted spectra. One device was observed to lase at 1.34 eV, corresponding to the small peak at the right of the spectra. This behavior was also observed by Sheih, *et. al.*, in their .20 indium mole-fraction single quantum well devices. They attributed the shift to band filling due to the high material gain required to overcome the high lateral loss also observed.

6.c. Comparison of Model to Fabricated Devices

The gain spectra extracted from the spectral output of the lasers is different than that calculated via the procedure outlined in Chapter 5. The relationship between the two is shown in Equation 6.1. The gain modeled is the material gain, G_{mat} , and the gain extracted is

the net cavity gain, G_{net} . The values of the distributed loss and confinement factor are not easily calculated, or measured, so that a detailed comparison of the two gain spectra is difficult. The two types of gain spectra, for the 0.0 mole-fraction indium device, are shown in Figure 6.5. The material gain was calculated at an assumed carrier density such that the peak gain was 75 cm^{-1} and the Lorentzian smoothing used a 100 fs inter-carrier scattering time. The spectra "without shift" is that calculated without the addition of a renormalization of the band gap due to high carrier densities[59]. The spectra "with shift" includes a rigid shift of the band gap to lower energies by an amount given in Equation 6.2. The correct application of band gap renormalization to the specific case of quantum well sub-bands is not clear but these two calculated spectra should represent brackets to the peak gain position.

This comparison, as a function of indium mole-fraction, is shown in Figure 6.6. The shaded area is the region between the

$$\Delta E_g = -3.2 \times 10^{-8} N_{\text{qw}}^{1/3} \quad (6.2)$$

where ΔE_g : shift in the band gap
 N_{qw} : volumetric carrier density

shifted and unshifted calculated peak energy measured at the material transparency carrier density. The diamonds are the peak gain positions of the fabricated lasers at threshold. The error bars are the approximate uncertainty in the indium concentration in the fabricated structures. The peak gain position calculated by the model

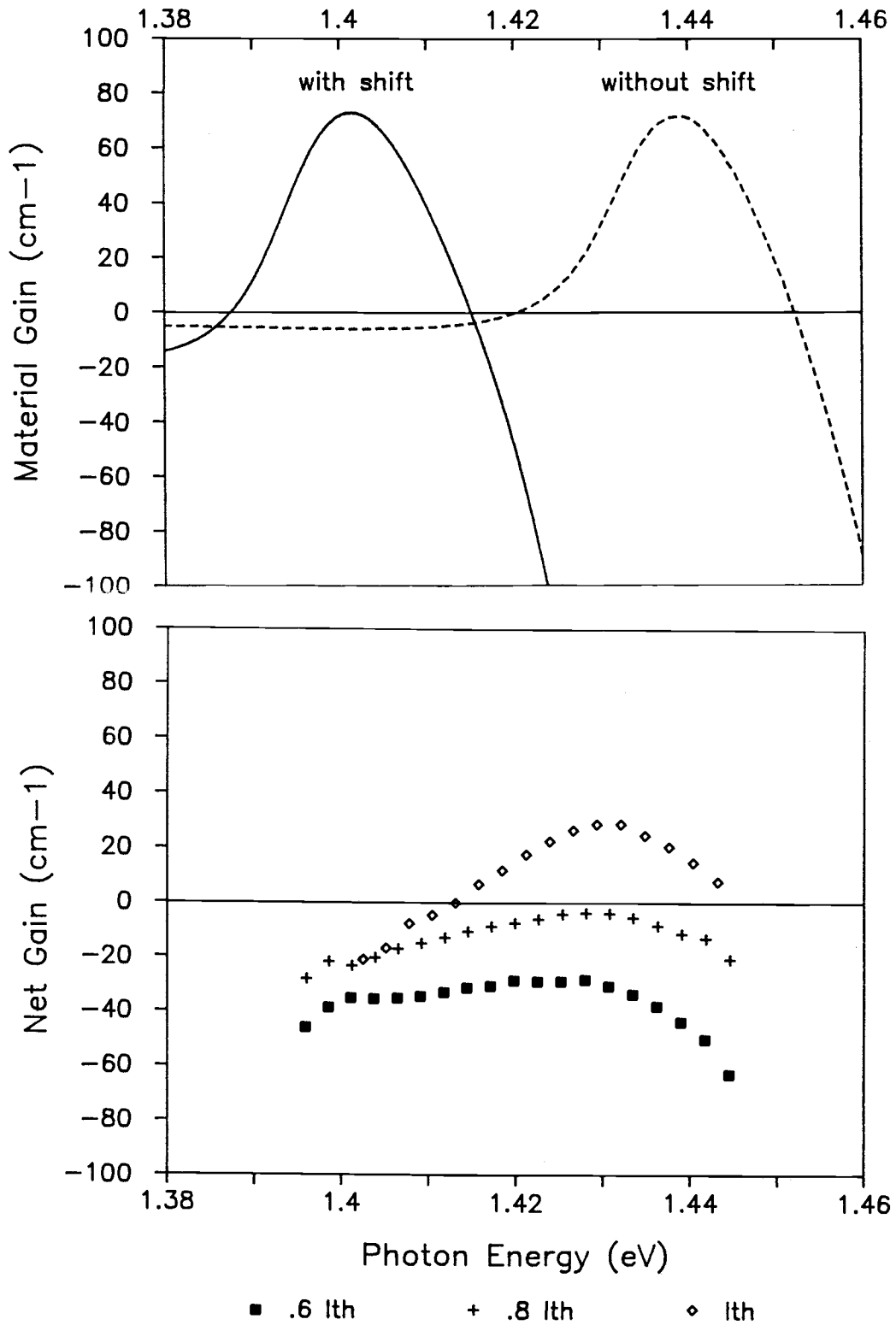


Figure 6.5: Calculated material gain (top) and measured net cavity gain (bottom) for the 0.0 mole-fraction indium laser.

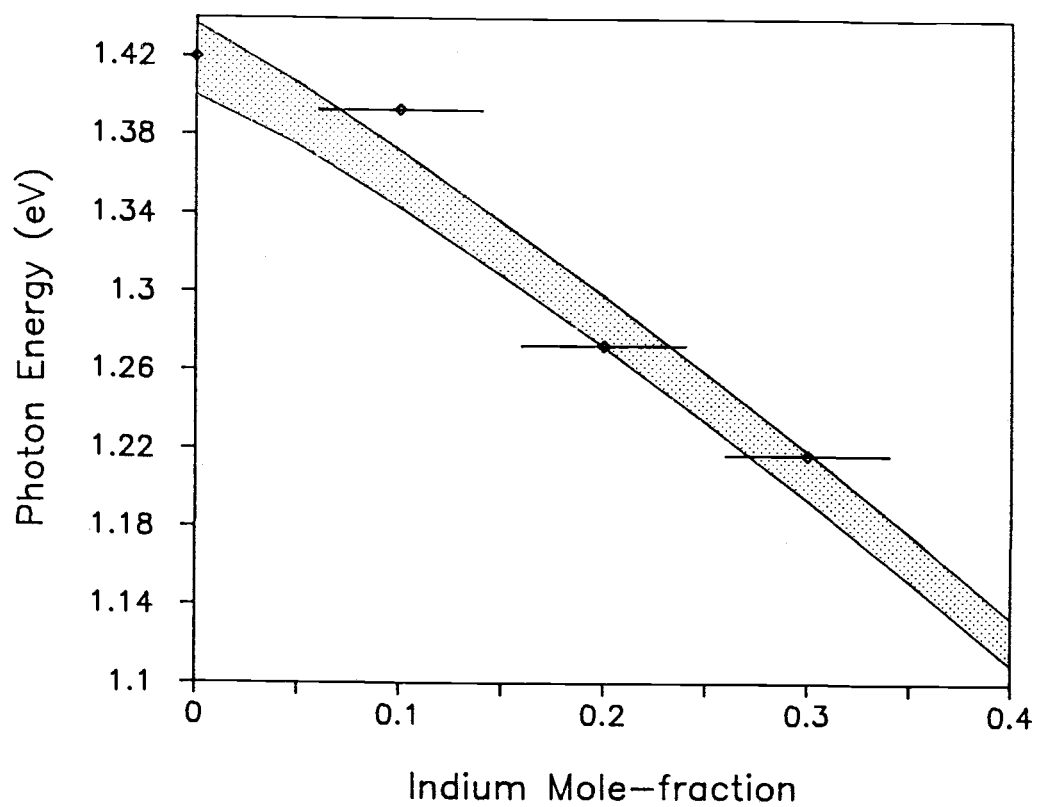


Figure 6.6: Comparison of the calculated material transparency energy and the peak net cavity gain as a function of indium mole-fraction.

is in reasonable agreement with that measured.

The sensitivity of the calculation to various model parameters was tested by running the 0.10 indium mole-fraction case at various carrier densities and quantum well widths. The result of this is shown in Figure 6.7 and Figure 6.8. The shift with carrier density from low values of maximum material gain is small, on the order of 6 meV for material gains between 154 cm^{-1} to 764 cm^{-1} . This shift is small compared to the scale of Figure 6.6 but none the less should be added to the calculated curves as the material gain at threshold is near 1000 cm^{-1} .

The sensitivity of the model to variation in the quantum well width is also weak, as shown in Figure 6.8. If the uncertainty in the indium concentration was the exclusive cause of variation in the quantum well width then possible widths would range from 9.6 to 10.4 nm. The variation in transparency energy associated with widths between 9.0 and 11.0 nm is 5 meV, small in comparison to the scale of Figure 6.6.

Another device parameter which can be extracted from the model is the carrier density required for transparency. The model predicts that the transparency carrier density will decrease with an increase in the indium mole-fraction in the quantum well. If all the carrier and optical losses were invariable as a function of indium mole-fraction, then this reduction would translate into a decrease in the threshold current density. The actual devices showed an significant increase in threshold current with the addition of indium. This trend is supposed to be due to extrinsic effects not dealt with in the model, as discussed at the beginning of this chapter.

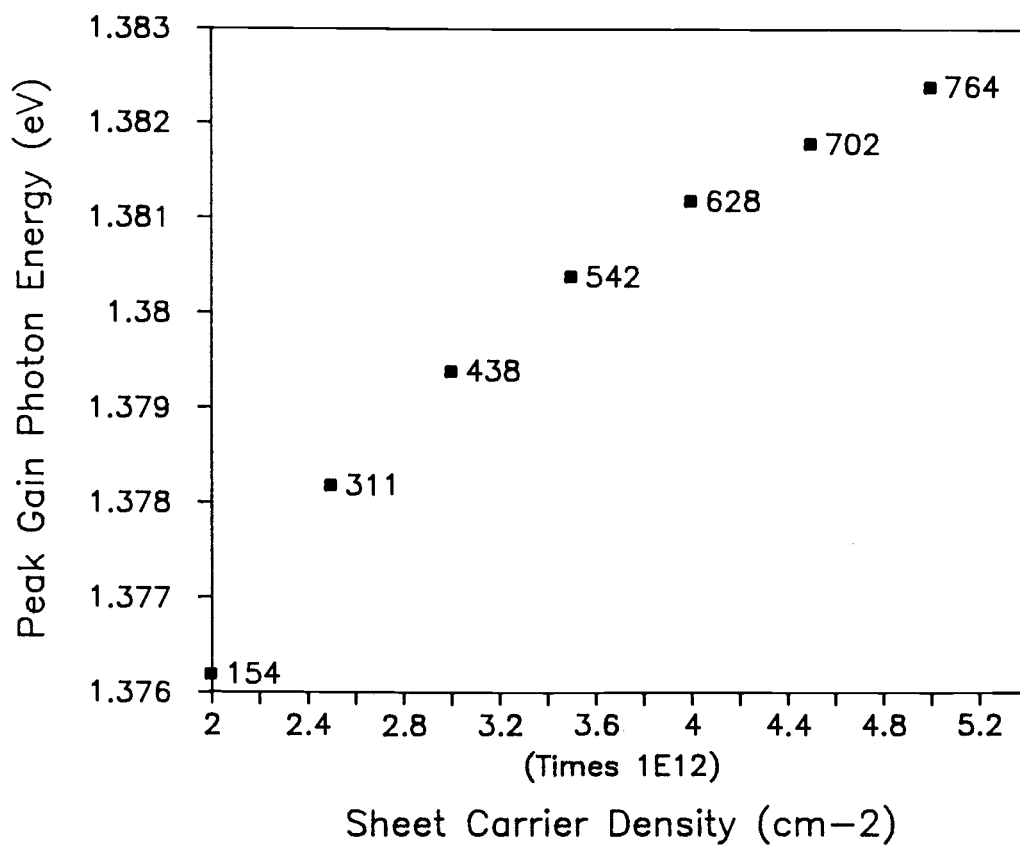


Figure 6.7: Sensitivity of the peak gain photon energy to variation in the carrier density. The peak material gain is listed beside the point.

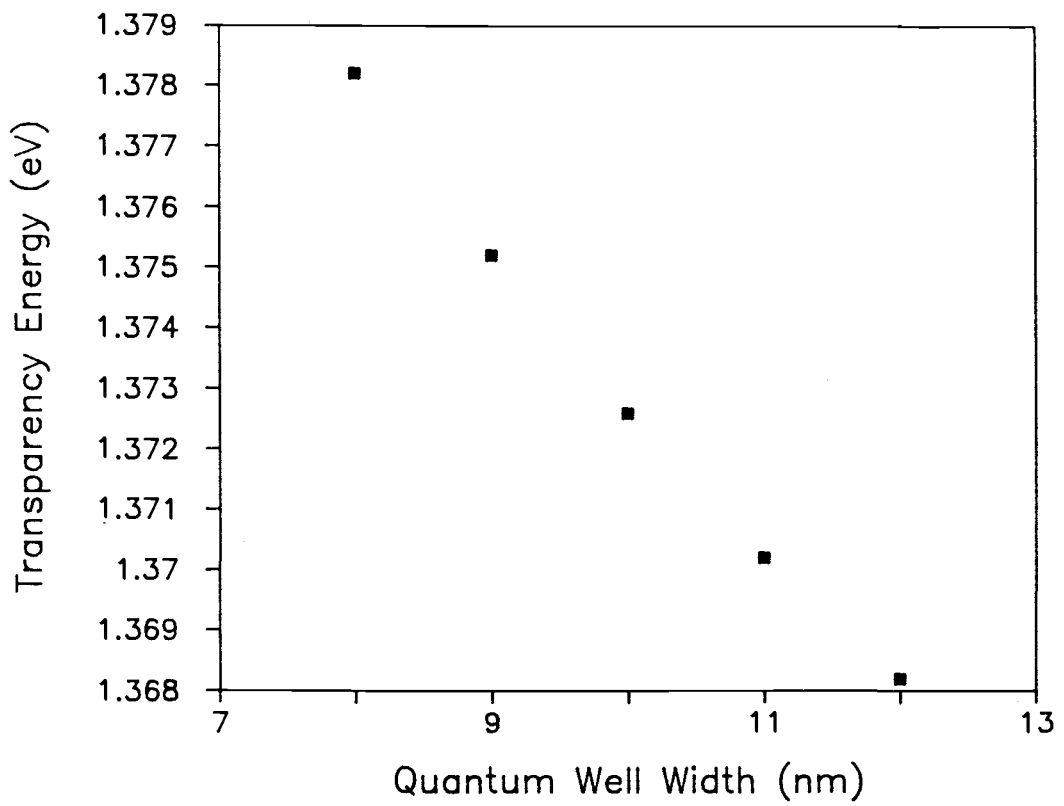


Figure 6.8: Sensitivity of the material transparency energy to variation in the quantum well width.

6.d. Model Predictions

The gain spectra model was used to predict the operating wavelength of GRIN-SCH structures not fabricated in this work. To predict the maximum wavelength obtainable in the pm-InGaAs system a series of device structures have been modeled, the well widths and indium concentrations chosen to lie on the critical thickness curve as given by Matthews and Blakeslee. The points modeled are shown in Figure 6.9. Indium mole-fractions between 0.1 and 1, in steps of 0.1, were chosen. The material transparency wavelength, as a function of indium mole-fraction, is shown in Figure 6.10. In the limit of InAs grown on GaAs the predicted wavelength of operation is greater than 1.3 microns. The transparency wavelength follows the slope of the pm-InGaAs band edge in these high indium concentration simulations due to the fact that the critical thickness is fairly constant as a function of indium mole-fraction. This means that quantum confinement effects, which increase the energy separation of the lowest conduction and valence sub-bands, do not offset the decrease in transition energy due to the smaller band gap of higher indium mole-fraction material.

The carrier density associated with transparency, for the same sequence of structures, is shown in Figure 6.11. The predicted transparency carrier density drops dramatically as indium mole-fraction is increased. This result verifies the qualitative prediction made by Yablonivitch and Kane[38], discussed in Chapter 2. The decrease in transparency carrier density with increase in indium mole-fraction arises from three effects. The first is the reduction in lateral carrier mass in the valence band due to the separation of the heavy and light hole bands[25]. The second effect is that quantum

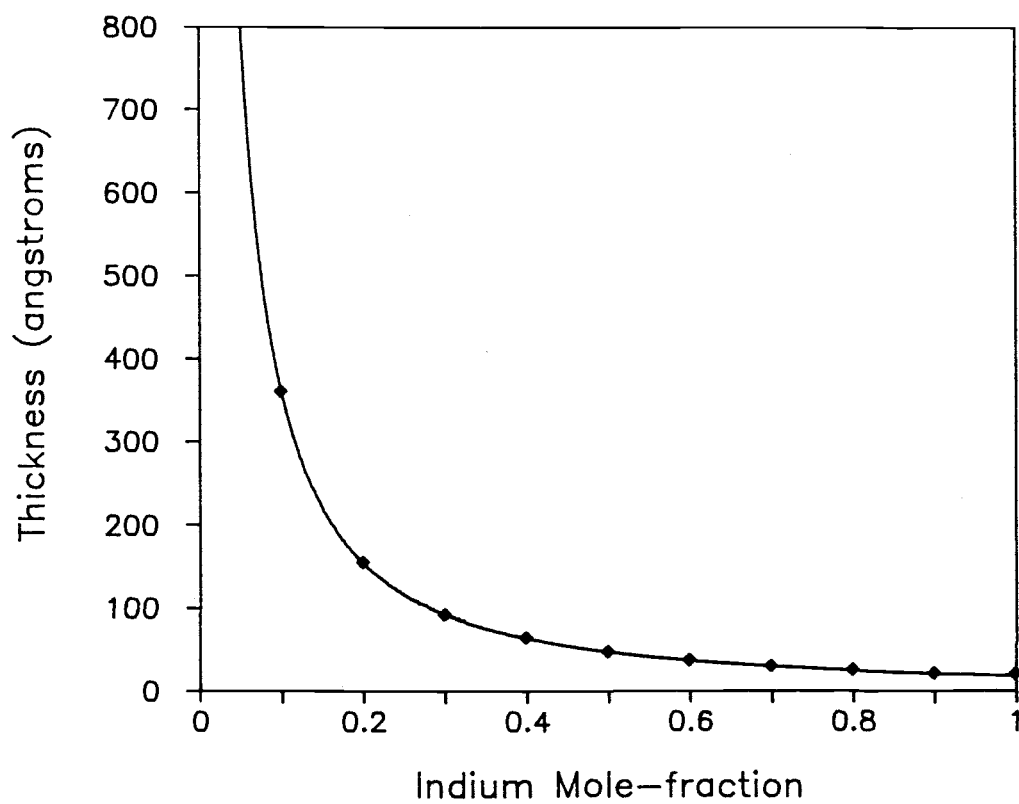


Figure 6.9: The critical thickness curve of Matthews and Blakeslee (solid) with the modeled quantum well values marked (diamonds).

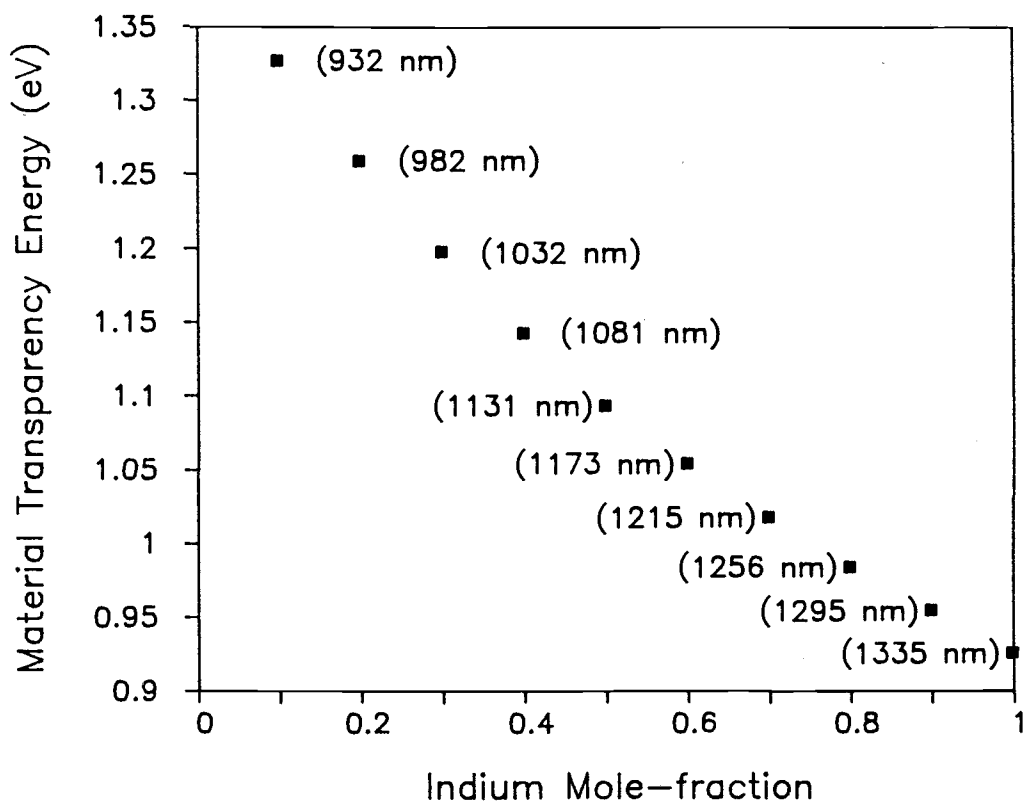


Figure 6.10: Modeled material transparency wavelength for structures along the critical thickness curve.

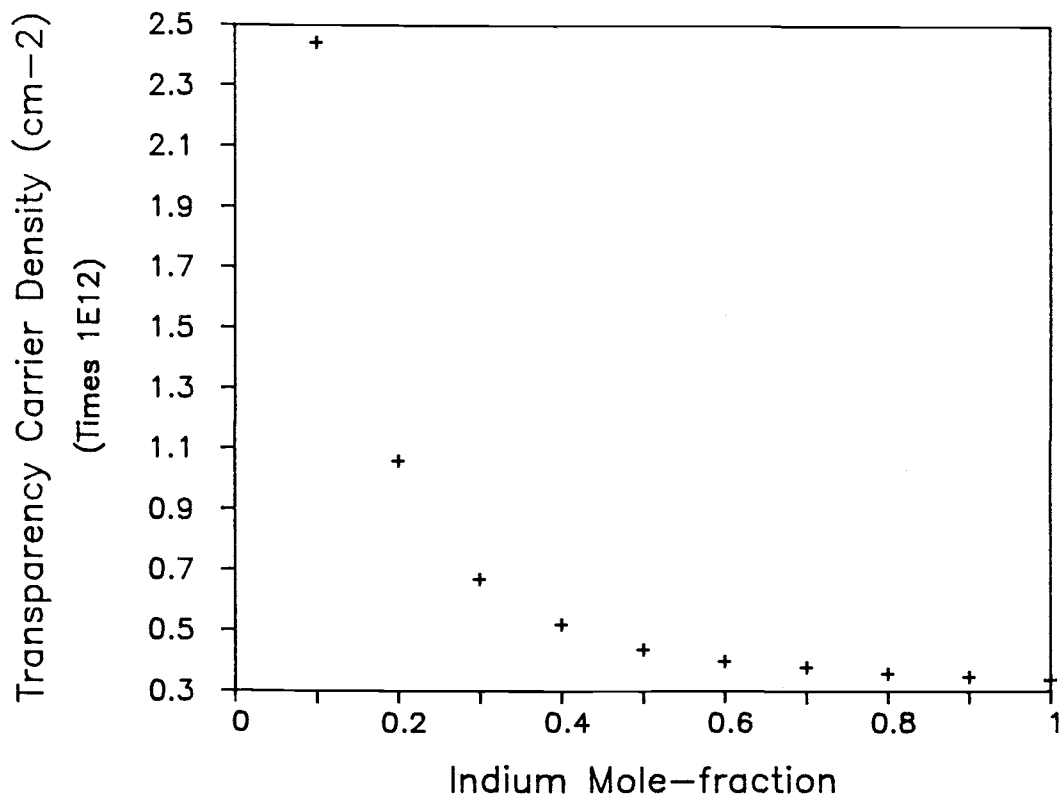


Figure 6.11: Modeled transparency carrier density for structures along the critical thickness curve.

confinement shifts the higher order sub-bands to energies significantly greater than the $n=1$ sub-bands. This fact is particularly true for narrow active region widths. The isolation in energy of the $n=1$ sub-bands is helped by the third effect, which is that the shear strain splits the light hole sub-bands significantly away from the band edge. The result is that at high indium concentrations the valence band edge is comprised of a sub-band with a light lateral mass, isolated in energy from other sub-bands, and therefore the quasi-Fermi levels move quickly in energy with the addition of excess carriers, and thus achieves threshold more easily.

Devices constructed from high indium mole-fraction pm-InGaAs should operate at wavelengths in excess of 1.3 microns and have extremely low threshold current density. The material problems associated with the growth of these highly strained epitaxial layers though, are largely unexplored[60].

7. Summary, Conclusions and Suggestions

7.a. Summary

This thesis reports on the crystal growth, fabrication, modeling and performance of pseudomorphic InGaAs diode lasers. The impetus for this work was to investigate the use of this material system in optical sources at wavelengths between 890 nm and 1300 nm. Probable applications for devices in this wavelength region include gas sensing, spectroscopy and pump sources for long wavelength glass lasers.

MBE grown laser epitaxial layers, at 0.0, 0.10, 0.20, 0.30 and 0.40 mole-fraction indium, were grown. These were processed into laser diodes and the device performance measured. Room temperature lasing was obtained from those devices which contained 0.0, 0.10 and 0.20 mole-fraction indium. The devices which contained 0.30 mole-fraction indium displayed bright spontaneous emission at room temperature but no laser action. The devices which contained 0.40 mole-fraction indium were good diodes but no light emission could be detected. The 0.20 mole-fraction indium lasers displayed an anomalous interference pattern in their spectral emission, as well as a high net gain at both the band edge and a higher energy transition. The spontaneous emission from an operating device was imaged through the substrate and severe inhomogeneity in the emission along the stripe length was observed.

A problem in the growth of the epitaxial layers, associated with the disparate temperature regimes which AlGaAs and InGaAs individually would be grown, was identified. The solution devised to circumvent this problem was the use of a growth interruption in the

active region, after passivation of the surface with a thin GaAs layer.

A model was developed to calculate the material gain of pseudomorphic InGaAs laser diodes as a function of indium mole-fraction and carrier density. This model was designed to deal with the strain perturbations to the band energies and carrier masses, to first order.

7.b. Conclusions

The stop growth procedure utilized to circumvent the growth problems associated with the close proximity of InGaAs and AlGaAs caused an increase in the threshold current density of the devices. This conclusion is supported by the increase in threshold current density measured between the 0.0 and 0.10 mole-fraction indium devices (the 0.0 concentration epitaxial layer was grown without interruption and the 0.10 concentration layer was grown with interruption). The recent work of Offsey, *et. al.*, [42] demonstrated that growth interruption does not necessarily lead to higher threshold current density. The implication being that the competitive non-radiative processes in the devices presented in this thesis are occurring in the AlGaAs, adjacent to the active region, which was grown at low temperature.

The variation in threshold current density with indium concentration is consistent with the theoretical work of Matthews and Blakeslee on the formation of dislocations in strained films. The critical indium concentration for a 10 nm InGaAs film grown on GaAs is 28%. The 0.30 mole-fraction indium laser is slightly over that limit and the devices fabricated from that epitaxial layer failed to lase at

room temperature. The PL spectra from the 0.30 concentration epitaxial layers also displayed the characteristic line width broadening associated with misfit dislocation formation. This is not a confirmation of the Matthews-Blakeslee limit in detail as there is uncertainty in the actual indium concentration, and well width, in the films.

The anomalous beating in the spectra of the 0.20 indium mole-fraction lasers correlated with the existence of severe inhomogeneity in carrier density along the laser stripe, as seen in the spontaneous emission. Devices with 0.10 mole-fraction indium displayed neither the interference pattern nor the inhomogeneous spontaneous emission. The three probable causes for this non-uniformity are: variations in contact resistance along the stripe, damage in the epitaxial layer caused by poor substrate material or the formation of misfit dislocations, even at this low indium concentration. The possibility that the cause is contact resistance variation is unlikely as the stripe is in contact with a thick, highly doped, GaAs cap layer which would smooth out variation in the current flow due to non-uniform contact. If the cause was substrate related, e.g., polish damage, it should have shown up in the 0.10 and 0.0 indium mole-fraction devices as well. This leaves the formation of misfit dislocations as the likely cause, but this is contrary to the conventional wisdom as pseudomorphic films are considered stable up to the critical thickness.

The numerical model developed for calculation of the material gain is found to be in good agreement with the wavelength of peak gain measured from the fabricated devices. The model also clearly

displayed the reduction in threshold carrier density predicted by Yablonivitch and Kane[38]. The threshold current density measured from the fabricated devices displayed the opposite trend than that predicted. This is thought to reflect material problems associated with the crystal growth, rather than the intrinsic performance of the laser epitaxial layer design.

Extension of the model to structures with high indium concentration active regions predicts that devices which operate at wavelengths in excess of 1.3 microns, with extremely low threshold current density, could be fabricated. This would be desirable for fiber optic communications as it would allow operation with lower power dissipation. Reliability of pm-InGaAs lasers has also been found to be similar to those constructed from lattice matched systems[41]. This is important as little is known about the interaction of intrinsic strain with laser degradation mechanisms.

7.c. Suggestions

Experimental verification of the predictions concerning high indium concentration structures is one obvious extension of this work. The problems associated with the growth of pm-InGaAs films with high indium concentration, are severe[61],[62] but probably not insurmountable[60].

The question of misfit formation below the critical indium concentration is also worthy of study. One possible interaction is the effect the substrate mis-orientation has on the critical thickness, as the Matthews-Blakeslee relationship was developed for singular crystal orientations.

The gain spectra model could be modified to more accurately

represent the sub-band structure of the quantum wells. Band-mixing effects have recently been shown to be significant in unstrained quantum well lasers[63], and would also be important in pm-InGaAs devices, especially at low indium mole-fraction. Further development and verification of the model would create a useful tool for the design of laser epitaxial layer structures.

Bibliography

- [1] W. T. Tsang, Semiconductors and Semimetals vol. 22 part A Materials Growth Techniques, (Academic Press, San Francisco, 1985).
- [2] H. C. Casey, Jr and M. B. Panish, Heterostructure Lasers part A Fundamental Principles, (Academic Press, San Francisco, 1978).
- [3] R. D. Burnham, C. Lindstroem, T. L. Paoli, D. R. Scifres, W. Streifer and N. Holonyak, *Appl. Phys. Lett.*, **42**, 937 (1983).
- [4] J. H. van der Merve, *J. Appl. Phys.* **34**, 117 (1963).
- [5] J. W. Matthews and A. E. Blakeslee, *J. of Crystal Growth*, **27**, 118 (1974).
- [6] W. D. Laidig, Y. F. Lin and P. J. Caldwell, *J. Appl. Phys.*, **57**, 33 (1985).
- [7] Y. J. Yang, K. Y. Hseih and R. M. Kolbas, *Appl. Phys. Lett.*, **51**, 215 (1987).
- [8] I. J. Fritz, S. T. Picraux, L. R. Dawson, T. J. Drummond, W. D. Laidig and N. G. Anderson, *Appl. Phys. Lett*, **46**, 967 (1985).
- [9] M. G. A. Bernard and G. Duraffourg, *Phys. Stat. Solidi*, **1**, 699 (1969).
- [10] C. S. Hong, W. I. Wang, L. F. Eastman and C. E. C. Wood, *Inst. Phys. Conf.*, **65**, 297 (1982).
- [11] W. T. Tsang, *J. Appl. Phys.*, **51**, 917 (1980).
- [12] W. T. Tsang, *Appl. Phys. Lett.*, **39**, 134 (1981).
- [13] D. Kameset, C. S. Hong, N. B. Patel and P. D. Dapkus, *Appl. Phys. Lett.*, **41**, 912 (1982).

- [14] P. L. Derry and A. Yariv, *Appl. Phys. Lett.*, **50**, 1773 (1987).
- [15] W. D. Laidig, C. K. Peng and Y. F. Lin, *J. Vac. Sci. Technol.*, B **2**, 181 (1984).
- [16] E. A. Fitzgerald, P. D. Kirchner, G. D. Petit, J. M. Woodall and D. G. Ast, *Mat. Res. Soc. Symp. Proc.*, **104** 633 (1988).
- [17] A. A. Ketterson, W. T. Masselink, J. S. Gedymin, J. Klem, C. K. Peng, W. F. Kopp, H. Morkoc and K. R. Gleason, *IEEE Trans Elec. Dev.*, **33**, 564, (1986).
- [18] G. E. Bulman, D. R. Myers, T. E. Zipperian, L. R. Dawson, J. J. Wiczer and R. M. Biefeld, *Appl. Phys. Lett.*, **47**, 733 (1985).
- [19] G. H. Olsen, C. J. Nuese and R. T. Smith, *J. Appl. Phys.*, **49**, 5523 (1978).
- [20] R. People and J. C. Bean, *Appl. Phys. Lett.*, **47** 322 (1985).
- [21] T. G. Andersson, Z. G. Chen, V. D. Kulakovskii, A. Uddin and J. T. Vallin, *Appl. Phys. Lett.*, **51**, 752 (1987).
- [22] G. Wicks, C. E. C. Wood, O. Ohno, L. F. Eastman, *J. Electron. Mat.*, **11**, 435 (1982).
- [23] J. M. Van Hove and P. Cohen, *Appl. Phys. Lett.*, **47**, 726 (1985).
- [24] J. T. Ebner and J. R. Arthur, *J. Vac. Sci. Technol.*, A **5**, 2007 (1987).
- [25] J. C. Hensel and G. Feher, *Phys. Rev.*, **129**, 1041 (1963).
- [26] H. Hasegawa, *Phys. Rev.*, **129**, 1029 (1963).
- [27] F. H. Pollak and M. Cardona, *Phys. Rev.*, **172**, 816 (1968).

- [28] E. O. Kane, J. Phys. Chem. Solids, 1, 249, (1957).
- [29] H. Asai and K. Oe, J. Appl. Phys., 54, 2052 (1983).
- [30] T. Ikegama, IEEE J. Quantum Elec., QE-8, 470 (1972).
- [31] E. Zielinski, H. Schweizer, S. Hausser, R. Stuber, M. Pilkuhn and G. Weimann, IEEE J. Quantum Elec., QE-23, 969 (1987).
- [32] M. Yamada, S. Ogita, M. Yamagishi, K. Tabata, N. Nakaya, M. Asada and Y. Suematsu, Appl. Phys. Lett. 45, 324 (1984).
- [33] M. Asada, A. Kameyama and Y. Suematsu, IEEE J. Quantum Elec., QE-20, 745 (1984).
- [34] S. R. Chinn, P. S. Zory and A. R. Reisinger, IEEE J. Quantum Elec., QE-24, 2191 (1988).
- [35] F. M. Ryan and R. C. Miller, Appl. Phys. Lett., 3, 162 (1963).
- [36] N. B. Patel, J. E. Ripper and P. Brosson, IEEE J. Quantum Elec., QE-9 (1973).
- [37] N. K. Dutta, J. Appl. Phys., 55, 285 (1984).
- [38] E. Yablonovitch and E. O. Kane, J. Lightwave Tech., LT-4, 504 (1986).
- [39] W. D. Laidig, P. J. Caldwell, Y. F. Lin and C. K. Peng, Appl. Phys. Lett., 44, 653 (1984).
- [40] S. E. Fischer, D. Fekete, G. B. Feak and J. M. Ballantyne, Appl. Phys. Lett., 50, 714 (1987).
- [41] P. K. York, K. J. Beernink, G. E. Fernandez and J. J. Coleman, Proceeding of Quantum Wells for Optics and Optoelectronics, Opt. Soc. Amer. Tech. Dig. Ser., 10, 132 (1989).

- [42] S. D. Offsey, W. J. Schaff, P. J. Tasker, H. Ennen and L. F. Eastman, *Appl. Phys. Lett.*, **54**, 2527 (1989).
- [43] private conversation with J. Coleman.
- [44] M. Asada and Y. Suematsu, *IEEE J. Quantum Elec.*, **QE-21**, 434 (1985).
- [45] C. Kittel, *Introduction of Solid State Physics*, (John Wiley & Sons., Toronto, 1976).
- [46] S. Adachi, *J. Appl. Phys.*, **58**, R1 (1985).
- [47] O Madelung, *Physics of III-V Compounds*, (John Wiley & Sons., Toronto, 1964).
- [48] D. J. Wolford, T. F. Kuech and J. A. Bradley, *J. Vac. Sci. Technol.*, **B 4**, 1043 (1986).
- [49] J. Menendez, A. Pinczuk, D. J. Werder, S. K. Sputz, R. C. Miller, D. L. Silvco and A. Y. Cho, *Phys. Rev. B*, **36**, 8165 (1987).
- [50] T. G. Andersson, Z. G. Chen, V. D. Kulakovskii, A. Uddin and J. T. Vallin, *Phys. Rev. B*, **37**, 4032 (1988).
- [51] S. P. Kowalczyk, W. J. Schaffer, E. A. Kraut and R. W. Grant, *J. Vac. Sci. Technol.*, **20**, 705 (1982).
- [52] P. C. Chow, *Amer. J. Phys.*, **40**, 730 (1972).
- [53] J. H. Neave, B. A. Joyce, P. J. Dobson and N. Norton, *Appl. Phys. A*, **31**, 1 (1983).
- [54] V. Swaminathan, J. L. Zilko, W. T. Tsang and W. R. Wagner, *J. Appl. Phys.*, **53**, 5163 (1982).
- [55] K. Y. Lau and A. Yariv, *IEEE J. Quantum Elec.*, **QE-21**, 121 (1985).

- [56] R. Heckingbottom, *J. Vac. Sci. Technol.*, B 3, 572 (1985).
- [57] C. Sheih, J. Mantz, H. Lee, D. Ackley and R Engelmann, *Appl. Phys. Lett.*, 54, 2521 (1989).
- [58] B. W. Hakki and T. L. Paoli, *J. Appl. Phys.*, 46, 1299 (1975).
- [59] D. A. Kleinman and R. C. Miller, *Phys. Rev. B*, 32, 2266 (1985).
- [60] F. J. Grunthaler, M. Y. Yen, R. Fernandez, T. C. Lee, A. Madhukar and B. F. Lewis, *Appl. Phys. Lett.*, 46, 983 (1985).
- [61] R. A. A. Kubiak, E. H. C. Parker, S. Newstead and J. J. Harris, *Appl. Phys. A*, 35, 61 (1984).
- [62] J. D. Grange, E. H. C. Parker and R. M. King, *J. Phys C: Appl. Phys.*, 12, 1601 (1979).
- [63] S. Colak, R. Eppenga and M. F. H. Schuurmans, *IEEE J. Quantum Elec.*, QE-23, 960 (1987).
- [64] L. C. Andreani, A. Pasquarello and F. Bassani, *Phys. Rev. B*, 36, 5887 (1987).
- [65] W. Poetz and D. K. Ferry, *J. Vac. Sci. Technol.*, B 4, 1006 (1986).
- [66] S. R. Chinn, *Appl. Optics*, 23, 3508 (1984).

APPENDIX

A. Gain Spectra Program

The program to calculate gain spectra was written by Dr. Jenifer Lary and the author. Dr. Lary wrote the first version of the Schroedinger equation solver which was then modified to its present form. Description of the program design is given in Chapter 5. The following is an outline of the information necessary to run the program. The input parameters required are listed below:

'dtemp'	device temperature ($^{\circ}\text{K}$)
'scstar'	starting sheet carrier density (cm^{-2})
'scstep'	sheet carrier density step (cm^{-2})
'numsc'	number of carrier densities
'enstar'	starting energy of spectrum (eV)
'enstep'	spectrum resolution
'numen'	number of energy steps
'numlev'	number of sub-bands simulated
'concin'	indium mole-fraction
'gselec'	initial guess: first electron sub-band
'gshh'	initial guess: first heavy hole sub-band
'gslh'	initial guess: first light hole sub-band
'itte'	maximum iterations on one sub-band
'istep'	number of points to step in on overflow
'tscatter'	scattering time for the smoothing
'shift spectra'	shift the spectra due to carrier density
'read xx.elv'	read the sub-band levels from a file

The device temperature, 'dtemp', is only used to calculate the Fermi functions and does not modify the band gaps of the various materials. The 300°K band edges are assumed. Up to 10 sheet carrier densities can be specified with 'numsc'. Up to 50 sub-band energy levels can be calculated but typically there is only significant carrier density in the lowest five.

The routine which solves Schroedinger's equation, 'psiall', is sensitive to the initial guesses at the energy eigenvalue: 'gselec', 'gshh' and 'gslh'. These need to be chosen judiciously or convergence could be a problem. The parameters 'istep' and 'itte' are also part of

the routine which solves Schroedinger's equation: 'itte' is the maximum number of attempts that will be made to find the solution for one particular energy and sub-band, and 'istep' is the number of points that the program will step in from the edge, if it started the calculation too far from the active region (the solution will become too large, viz. overflow, if the calculation starts too far away from the quantum well). The composition profile for a GRIN-SCH laser, grown as described in Chapter 3, is calculated but the energy level calculation can deal with an arbitrary potential so other structures could be simulated.

The 'shift spectra' input determines whether a rigid shift of the spectra is done according to Equation 6.2. The 'read xx.elv' input allows the energy level values and masses to be read from a file created in a previous run. This saves execution time as the energy level calculation is the most time consuming routine in the program. A typical input deck is shown in Figure A.1.

```
'dtemp '      300.0
'scstar'      5.0e11
'scstep'      1.0e11
'numsc'       9
'enstar'      1.25
'enstep'      .0002
'numen'       750
'numlev'      5
'concin'      .20
'gselec'      .015
'gshh'        .006
'gslh'        .006
'itte'        125
'istep'       75
'tscatter'    .25
'shift spectra' 'n'
'read xx.elv' 'y'
```

Figure A.1: The input deck for the calculation of the gain spectra for a $\text{In}_{.2}\text{Ga}_{.8}\text{As}$ GRIN-SCH laser.

```

$large
c
c Program to calculate the gain spectra of a GRIN-SCH laser structure.
c Main program written by John Ebner, 4-11-89
c Wavefunction solution subroutine written by Jenifer Lary, 4-10-89
c
  Program gainspec
c
c Dimension the necessary variables:
c   concin: indium mole-fraction in the quantum well
c   comp(2,4000): the composition variation with distance
c     comp(1,x) is the aluminum mole fraction
c     comp(2,x) is the indium mole fraction
c   vi(4000): potential under forward bias
c   answer: "Y" or "N" in response to program queries
c   index1: general purpose integer variable
c   index2: general purpose integer variable
c   iproty: profile type
c     1: conduction band
c     2: heavy hole valence band
c     3: light hole valence band
c   idebug: debug output from the wavefunction solver "On" or "Off"
c   etol: convergence energy tolerance
c   itte: maximum number of iterations before quitting
c   istep: initial step size used to find starting point
c   ntot: total number of points in potential profile
c   dx: the profile resolution in cm
c   ietot: total number of conduction band states
c   ilhtot: total number of light hole band states
c   ihhtot: total number of heavy hole band states
c
  dimension psi(4000),vi(4000),xms(2,4000),elev(3,50),flev(2,50)
  dimension psist(6,4000),xymass(3,50),zmass(3,50)
  dimension gain(10,1000)
  dimension comp(2,4000)
  character root*6
  character answ*1
  character label*16
  character shift*1
  character readen*1
  common/constant/pi,hbar,xm0,bcon,dtemp
  common/waves/vi,psi,xms,elev,dx,psist,xymass,zmass,flev
  common/inputs/ntot,ietot,ihhtot,ilhtot,etol,itte,nlev
  common/bugs/idebug
  common/compos/comp
  common/spec/gain
c
c Constants used in the program.
c hbar is actually hbar*c, in ev-cm, and xm0 is electron mass, eV/c**2
c
  pi=3.1415927
  hbar=1.9733e-5
  xm0=0.511e6

```

```

nskip=5
bcon=8.6174e-5
123 mode=0
    etol=1.0e-6
c
    write(*,*)' '
    write(*,*)'Program to generate gain spectra for a GRIN-SCH laser'
c
c Zero the necessary arrays.
c
    do 30 index1=1,3
        do 32 index2=1,50
            elev(index1,index2)=0.0
            xymass(index1,index2)=0.0
            zmass(index1,index2)=0.0
32     continue
30 continue
c
    do 34 index1=1,6
        do 36 index2=1,4000
            psist(index1,index2)=0.0
36     continue
34 continue
c
    do 38 index1=1,2
        do 39 index2=1,50
            flev(index1,index2)=0.0
39     continue
38 continue
c
    do 42 index1=1,10
        do 44 index2=1,1000
            gain(index1,index2)=0.0
44     continue
42 continue
c
    do 46 index1=1,4000
        psi(index1)=0.0
        comp(1,index1)=0.0
        comp(2,index1)=0.0
        vi(index1)=0.0
        xms(1,index1)=0.0
        xms(2,index1)=0.0
46 continue
c
c Ask for the root name for all the output files.
c
    write(*,*)' '
    write(*,*)'Input the root filename for output:'
    read(*,'(a)')root
c
c Ask if running from a file
c

```

```

2 write(*,*)' '
  write(*,*)'Run independently?'
  read(*, '(a)')answ
  if((answ.eq.'N').or.(answ.eq.'n'))go to 4
124  if((answ.eq.'Y').or.(answ.eq.'y'))go to 5
     write(*,*)' '
     write(*,*)'Please answer Y or N'
     go to 2
5 mode=1
4 open(2,file=root//'.dat',status='old')
  read(2,*)label,dtemp
  read(2,*)label,scstar
  read(2,*)label,scstep
  read(2,*)label,numsc
  read(2,*)label,enstar
  read(2,*)label,enstep
  read(2,*)label,numen
  read(2,*)label,numlev
  read(2,*)label,concin
  read(2,*)label,dx
  read(2,*)label,inthk
  read(2,*)label,gselec
  read(2,*)label,gshh
  read(2,*)label,gslh
  read(2,*)label,itte
  read(2,*)label,istep
  read(2,*)label,tsc
  read(2,*)label,shift
  read(2,*)label,readen
  close(unit=2)
c
  if(readen.eq.'n')go to 10
c
  open(2,file=root//'.elv',status='old')
  read(2,*)
  read(2,*)
  read(2,*)
  read(2,*)
  read(2,*)
  read(2,*)
  do 9 index1=1,numlev
    read(2,*)elev(1,index1),elev(2,index1),elev(3,index1)
    read(2,*)xymass(1,index1),xymass(2,index1),xymass(3,index1)
    read(2,*)zmass(1,index1),zmass(2,index1),zmass(3,index1)
  9 continue
  close(unit=2)
  go to 480
c
c Call the subroutine which generates the mole fraction variation
c from the growth data.
c
10 write(*,*)' '
    write(*,*)'Now generating the composition variation'

```

```

        call compgen(concin,ntot,inthk,dx)
c
c Ask if operator wants to store the composition variation.
c
12 write(*,*)' '
   write(*,*)'Store the composition variation? Y or N'
125
   if(mode.eq.1)write(*,*)'y'
   if(mode.eq.1)go to 20
   read(*,'(a)')answ
   if((answ.eq.'N').or.(answ.eq.'n'))go to 15
   if((answ.eq.'Y').or.(answ.eq.'y'))go to 20
   write(*,*)' '
   write(*,*)'Please answer Y or N'
   go to 12
20 write(*,*)' '
   write(*,*)'The composition file is:',root,'.com'
   open(2,file=root//'.com',status='unknown')
   write(2,*)'Composition variation with distance:'
   write(2,*)'Position, A1 mole fraction, In mole fraction'
   do 25 index1=1,ntot,nskip
      write(2,*)(dx*(index1-1)),comp(1,index1),comp(2,index1)
25 continue
   close(unit=2)
15 continue
   write(*,*)' '
   write(*,*)'Total number of points is:',ntot
c
c Call the subroutine to generate the conduction band potentials from
c the composition.
c
   write(*,*)' '
   write(*,*)'Now generating the conduction band potential'
   iproty=1
   call profgen(iproty,ntot)
c
40 write(*,*)' '
   write(*,*)'Store the conduction potential variation? Y or N'
   if(mode.eq.1)write(*,*)'y'
   if(mode.eq.1)go to 50
   read(*,'(a)')answ
   if((answ.eq.'N').or.(answ.eq.'n'))go to 60
   if((answ.eq.'Y').or.(answ.eq.'y'))go to 50
   write(*,*)' '
   write(*,*)'Please answer Y or N'
   go to 40
50 write(*,*)' '
   write(*,*)'The conduction band potential file is:',root,'.ept'
   open(2,file=root//'.ept',status='unknown')
   write(2,*)'Electron potential variation with distance:'
   write(2,*)'Position, Potential, z mass, xy mass'
   do 70 index1=1,ntot,nskip
      write(2,*)(dx*(index1-1)),vi(index1),xms(1,index1),
+ xms(2,index1)

```

```

70 continue
   close(unit=2)
60 continue
c
c Calculate the conduction band wavefunctions.
c
c Call the subroutine to extract the energy levels from the conduction
c band potential.
c
c Variable elev(n,1) is the initial energy guess, subsequent energy
c levels will use the previous energy level value as the initial guess.
c
   write(*,*)' '
   write(*,*)'Now calculating the conduction band energies'
80 write(*,*)'Do you want debug on? Y or N'
   if(mode.eq.1)write(*,*)'n'
   if(mode.eq.1)go to 86
   read(*,'(a)')answ
   if((answ.eq.'Y').or.(answ.eq.'y'))go to 84
   if((answ.eq.'N').or.(answ.eq.'n'))go to 86
   write(*,*)' '
   write(*,*)'Please answer Y or N'
   go to 80
84 idebug=1
   go to 90
86 idebug=0
c
90 elev(1,1)=gselec
   call psiall(iproty,istep,nbadel,numlev)
   ietot=nlev-1
c
c Call the subroutine to generate the heavy hole valence band potential
c from the composition.
c
   write(*,*)' '
   write(*,*)'Now generating the heavy hole band potential'
   iproty=2
   call profgen(iproty,ntot)
c
140 write(*,*)' '
   write(*,*)'Store the heavy hole potential variation? Y or N'
   if(mode.eq.1)write(*,*)'y'
   if(mode.eq.1)go to 150
   read(*,'(a)')answ
   if((answ.eq.'N').or.(answ.eq.'n'))go to 160
   if((answ.eq.'Y').or.(answ.eq.'y'))go to 150
   write(*,*)' '
   write(*,*)'Please answer Y or N'
   go to 140
150 write(*,*)' '
   write(*,*)'The heavy hole potential file is:',root,'.hpt'
   open(2,file=root//'.hpt',status='unknown')
   write(2,*)'Heavy hole potential variation with distance:'
   write(2,*)'Position, Potential, z mass, xy mass'

```

```

        do 170 index1=1,ntot,nskip
          write(2,*)(dx*(index1-1)),vi(index1),xms(1,index1),
+ xms(2,index1)
170 continue
      close(unit=2)
160 continue
c
c Call the subroutine to extract the energy levels from the heavy hole
c band potential.
c
c Variable elev(n,1) is the initial energy guess, subsequent energy
c levels will use the previous energy level value as the initial guess.
c
      write(*,*)' '
      write(*,*)'Now calculating the heavy hole band energies'
180 write(*,*)'Do you want debug on? Y or N'
      if(mode.eq.1)write(*,*)'n'
      if(mode.eq.1)go to 186
      read(*,'(a)')answ
      if((answ.eq.'Y').or.(answ.eq.'y'))go to 184
      if((answ.eq.'N').or.(answ.eq.'n'))go to 186
      write(*,*)' '
      write(*,*)'Please answer Y or N'
      go to 180
184 idebug=1
      go to 190
186 idebug=0
c
190 elev(2,1)=gshh
      call psiall(iproty,istep,nbadhh,numlev)
      ihhtot=nlev-1
c
c Call the subroutine to generate the light hole valence band potential
c from the composition.
c
      write(*,*)' '
      write(*,*)'Now generating the light hole band potential'
      iproty=3
      call profgen(iproty,ntot)
c
240 write(*,*)' '
      write(*,*)'Store the light hole potential variation? Y or N'
      if(mode.eq.1)write(*,*)'y'
      if(mode.eq.1)go to 250
      read(*,'(a)')answ
      if((answ.eq.'N').or.(answ.eq.'n'))go to 260
      if((answ.eq.'Y').or.(answ.eq.'y'))go to 250
      write(*,*)' '
      write(*,*)'Please answer Y or N'
      go to 240
250 write(*,*)' '
      write(*,*)'The light hole potential file is:',root,'.lpt'
      open(2,file=root//'.lpt',status='unknown')
      write(2,*)'Light hole potential variation with distance:'

```

```

        write(2,*)'Position, Potential, z mass, xy mass'
        do 270 index1=1,ntot,nskip
            write(2,*)(dx*(index1-1)),vi(index1),xms(1,index1),
+ xms(2,index1)
270 continue
        close(unit=2)
260 continue
c
c Call the subroutine to extract the energy levels from the light hole
c band potential.
c
c Variable elev(n,1) is the initial energy guess, subsequent energy
c levels will use the previous energy level value as the initial guess.
c
        write(*,*)' '
        write(*,*)'Now calculating the light hole band energies'
280 write(*,*)'Do you want debug on? Y or N'
        if(mode.eq.1)write(*,*)'n'
        if(mode.eq.1)go to 286
        read(*,'(a)')answ
        if((answ.eq.'Y').or.(answ.eq.'y'))go to 284
        if((answ.eq.'N').or.(answ.eq.'n'))go to 286
        write(*,*)' '
        write(*,*)'Please answer Y or N'
        go to 280
284 idebug=1
        go to 290
286 idebug=0
c
290 elev(3,1)=gslh
        call psiall(iproty,istep,nbadlh,numlev)
        ilhtot=nlev-1
c
c Ask the operator if wants to store the energy level values.
c
        write(*,*)' '
        write(*,*)'Number of energy levels in potentials:'
        write(*,*)ietot,' electron, ',ihhtot,' heavy hole, ',
+ ilhtot,' light hole'
        write(*,*)' '
        write(*,*)'Number of bad convergences'
        write(*,*)nbade1,' electron, ',nbadhh,' heavy hole, ',
+ nbadlh,' light hole'
340 write(*,*)' '
        write(*,*)'Store the energy levels? Y or N'
        if(mode.eq.1)write(*,*)'y'
        if(mode.eq.1)go to 350
        read(*,'(a)')answ
        if((answ.eq.'N').or.(answ.eq.'n'))go to 360
        if((answ.eq.'Y').or.(answ.eq.'y'))go to 350
        write(*,*)' '
        write(*,*)'Please answer Y or N'
        go to 340
350 write(*,*)' '

```

```

write(*,*)'The energy level file is:',root,'.elv'
open(2,file=root//'.elv',status='unknown')
write(2,*)'Number of energy levels in potentials:'
write(2,*)ietot,' electron, ',ihhtot,' heavy hole, ',
+ ilhtot,' light hole'
write(2,*)' '
write(2,*)'Number of bad convergences'
write(2,*)nbadel,' electron, ',nbadhh,' heavy hole, ',
+ nbadlh,' light hole'
write(2,*)'elec, hhole, lhole, elmass, hhmass, lhmass'
imax=ilhtot
if((ietot.ge.ihhtot).and.(ietot.ge.ilhtot))imax=ietot
if((ihhtot.ge.ietot).and.(ihhtot.ge.ilhtot))imax=ihhtot
do 370 index1=1,imax
  write(2,*)elev(1,index1),elev(2,index1),elev(3,index1)
  write(2,*)xymass(1,index1),xymass(2,index1),xymass(3,index1)
  write(2,*)zmass(1,index1),zmass(2,index1),zmass(3,index1)
370 continue
  close(unit=2)
360 continue
c
c Ask the operator if wants to store the saved wavefunctions.
c
440 write(*,*)' '
write(*,*)'Store the n= 1 & 2 state wavefunctions? Y or N'
if(mode.eq.1)write(*,*)'y'
if(mode.eq.1)go to 450
read(*,'(a)')answ
if((answ.eq.'N').or.(answ.eq.'n'))go to 460
if((answ.eq.'Y').or.(answ.eq.'y'))go to 450
write(*,*)' '
write(*,*)'Please answer Y or N'
go to 440
450 write(*,*)' '
write(*,*)'The wave function file is:',root,'.wve'
open(2,file=root//'.wve',status='unknown')
write(2,*)'Wavefunctions:'
write(2,*)'elec(1), elec(2), hhole(1), hhole(2), lhole(1),'
+ ' lhole(2)'
  do 470 index1=1,ntot,nskip
  write(2,99)(dx*(index1-1)),(psist(index2,index1),index2=1,6)
99  format(1x,7e12.6)
470 continue
  close(unit=2)
460 continue
c
c Calculate the quasi-Fermi level positions.
c
480 write(*,*)' '
write(*,*)'Now calculating the quasi-Fermi levels'
c
c The heavy hole-light hole splitting is obtained from the indium
c concentration terms returned from the profgen subroutine.
c

```

```

        call ferlev(scstar,scstep,numsc,numlev,concin)
c
c Ask the operator to store the quasi-Fermi levels.
c
540 write(*,*)' '
    write(*,*)'Store the quasi-Fermi levels? Y or N'
    if(mode.eq.1)write(*,*)'y'
    if(mode.eq.1)go to 550
    read(*,'(a)')answ
    if((answ.eq.'N').or.(answ.eq.'n'))go to 560
    if((answ.eq.'Y').or.(answ.eq.'y'))go to 550
    write(*,*)' '
    write(*,*)'Please answer Y or N'
    go to 540
550 write(*,*)' '
    write(*,*)'The quasi-Fermi level file is:',root,'.qfl'
    open(2,file=root//'.qfl',status='unknown')
    write(2,*)'quasi-Fermi levels:'
    write(2,*)'sheet density, conduction, valence'
        do 570 index1=1,numsc
            write(2,*)(scstar+((index1-1)*scstep),flev(1,index1),
+            flev(2,index1))
570    continue
    close(unit=2)
560 continue
c
c Calculate the gain spectra at the various Fermi levels.
c
    write(*,*)' '
    write(*,*)'Now calculating the gain spectrum'
    call gsp(enstar,enstep,numen,concin,scstar,scstep,numsc,numlev,
+ shift)
    if(tsc.eq.0.0)go to 640
    call conv(etran,enstar,enstep,numen,numsc,tsc)
c
c Ask the operator to store the gain spectrum.
c
640 write(*,*)' '
    write(*,*)'Store the gain spectra? Y or N'
    if(mode.eq.1)write(*,*)'y'
    if(mode.eq.1)go to 650
    read(*,'(a)')answ
    if((answ.eq.'N').or.(answ.eq.'n'))go to 660
    if((answ.eq.'Y').or.(answ.eq.'y'))go to 650
    write(*,*)' '
    write(*,*)'Please answer Y or N'
    go to 640
650 write(*,*)' '
    write(*,*)'The gain spectra file is:',root,'.gns'
    open(2,file=root//'.gns',status='unknown')
    write(2,*)'gain spectra'
    write(2,*)'energy, gain'
        do 670 index1=1,numen
            write(2,699)enstar+((index1-1)*enstep),

```

```

+      (gain(index2,index1),index2=1,numsc)
699      format(1x,11e12.6)
670      continue
      close(unit=2)
660      continue

c
900      continue
      stop
      end

c
c *****
c
      subroutine compgen(concin,ntot,inthk,dx)
c
c Subroutine to generate the potential profiles from the growth data.
c
c Dimension the required variables:
c   index1: position index in array
c   time: time in on segment of the MBE system oven controller
c   tga: gallium oven temperature
c   tal: aluminum oven temperature
c   tgai: inverse gallium oven temperature * 1000
c   tali: inverse aluminum oven temperature * 1000
c   gr: crystal growth rate (dynamic when grading composition)
c   dtime: time step required to grow .2 nm of material
c
      dimension comp(2,4000)
      dimension tcomp(2,20000)
      common/compos/comp
c
c This is not general but rather only valid for the following:
c   layer 1: 50% Al AlGaAs
c   layer 2: Graded AlGaAs grown by linearly changing both Al and
c   Ga oven temperatures. See growth 1-6-8-88.
c   layer 3: 7.5 nm GaAs
c   layer 4: 10 nm InGaAs
c   layer 5: 7.5 nm GaAs
c   layer 6: Graded AlGaAs, opposite to layer 2.
c   layer 7: 50 % Al AlGaAs
c
c The spatial resolution is variable.
c
c Section 1 of the structure is 100 nm of 50% Al AlGaAs
c
      do 5 index1=1,(100/(dx*1.0e8))
          tcomp(1,index1)=.5
      5 continue
c
c Section 2 is graded AlGaAs
c
      time=0.0
      tga=1025.0
      tal=1181.0

```

```

    tgai=(1.0/(tga+273.7))*1000
    tali=(1.0/(tal+273.7))*1000
    fga=10**((-12.42878*tgai)+9.34101)
    fal=10**((-16.32484*tali)+10.92115)
10  gr=(.85*fga*2.82665)+(fal*2.83025)
    dtime=dx*1.0e8*(1.0/gr)
    tga=tga+(dtime*.0339)
    tal=tal-(dtime*.05367)
    tgai=(1.0/(tga+273.7))*1000.0
    tali=(1.0/(tal+273.7))*1000.0
    fga=10**((-12.42878*tgai)+9.34101)
    fal=10**((-16.32484*tali)+10.92115)
    tcomp(1,index1)=fal/(fal+(.85*fga))
    index1=index1+1
    time=time+dtime
    if(time.lt.708.0)go to 10
C
C Section 3 is 7.5 nm GaAs
C
    do 15 index1=index1,(index1+(75/(dx*1.0e8)))
        tcomp(1,index1)=0
    15 continue
C
C Section 4 is a variable nm of InGaAs
C
    do 20 index1=index1,(index1+(inthk/(dx*1.0e8)))
        tcomp(1,index1)=0.0
        tcomp(2,index1)=concin
    20 continue
C
C Section 5 is 7.5 nm of GaAs
C
    do 25 index1=index1,(index1+(75/(dx*1.0e8)))
        tcomp(1,index1)=0.0
    25 continue
C
C Section 6 is graded AlGaAs
C
    time=0.0
    tga=1049.0
    tal=1143.0
    tgai=(1.0/(tga+273.7))*1000.0
    tali=(1.0/(tal+273.7))*1000.0
    fga=10**((-12.42878*tgai)+9.34101)
    fal=10**((-16.32484*tali)+10.92115)
30  gr=(.85*fga*2.82665)+(fal*2.83025)
    dtime=dx*1.0e8*(1.0/gr)
    tga=tga-(dtime*.0339)
    tal=tal+(dtime*.05367)
    tgai=(1.0/(tga+273.7))*1000.0
    tali=(1.0/(tal+273.7))*1000.0
    fga=10**((-12.42878*tgai)+9.34101)
    fal=10**((-16.32484*tali)+10.92115)
    tcomp(1,index1)=fal/(fal+(.85*fga))

```

```

        index1=index1+1
        time=time+dttime
        if(time.lt.708.0)go to 30
c
c Section 7 is 100 nm of 50% Al AlGaAs
c
        do 35 index1=index1,(index1+(100/(dx*1.0e8)))
            tcomp(1,index1)=.5
        35 continue
c
c Extract the center 4000 points for the calculation of the energy
c levels.
c
        ioff=0
        if((index1-1).le.4000)iend=index1-1
        if((index1-1).le.4000)go to 40
        ioff=((index1-1)-4000)/2
        iend=4000
    40 do 50 index1=1,iend
        comp(1,index1)=tcomp(1,(index1+ioff))
        comp(2,index1)=tcomp(2,(index1+ioff))
    50 continue
c
        ntot=index1-1
        return
        end
c
c *****
c
        subroutine profgen(iproty,ntot)
c
c Subroutine to generate the potentials from the composition variation.
c
        dimension psi(4000),vi(4000),xms(2,4000),elev(3,50),flev(2,50)
        dimension psist(6,4000),xymass(3,50),zmass(3,50)
        dimension comp(2,4000)
        common/bugs/idebug
        common/waves/vi,psi,xms,elev,dx,psist,xymass,zmass,flev
        common/compos/comp
c
c Generate the potential from the composition variation.
c
c Test if iproty=1; if so then generate the conduction band potential.
c
        vsmall=1.247
        if((iproty.eq.2).or.(iproty.eq.3))go to 200
c
c Generate the conduction band potential and mass variation.
c
        do 100 index1=1,ntot
            if(comp(2,index1).ne.0.0)go to 20
c
c If here then AlGaAs or GaAs.
c

```

```

vi(index1)=.67*(1.247*comp(1,index1))
xms(1,index1)=.067+(.083*comp(1,index1))
xms(2,index1)=xms(1,index1)
go to 90
C
c If here then InGaAs. The InGaAs is assumed to be surrounded by
c GaAs. The conduction band offset is assumed to be .40 x d(Eg,h).
C
20 c11=12.11-(comp(2,index1)*3.569)
c12=5.48-(comp(2,index1)*.82)
a=-7.1+(comp(2,index1)*1.7)
b=-1.7-(comp(2,index1)*.1)
e=(comp(2,index1)*.40515)/(5.65325+(comp(2,index1)*.40515))
egnat=1.424-(comp(2,index1)*1.064)
egh=egnat+((-2.0*a*((c11-c12)/c11))+b*((c11+(2*c12))/c11))*e
vi(index1)=-.40*(1.424-egh)
xms(1,index1)=.067-(comp(2,index1)*.044)
xms(2,index1)=xms(1,index1)
C
c Calculate the minimum of the potential.
C
90 if(vi(index1).lt.vsmall)vsmall=vi(index1)
C
100 continue
go to 400
C
c Test if iproty=2; if so then generate the heavy hole potential.
C
200 if(iproty.eq.3)go to 300
C
c Generate the heavy hole potential and mass variation.
C
do 250 index1=1,ntot
if(comp(2,index1).ne.0.0)go to 275
C
c If here then AlGaAs or GaAs.
C
vi(index1)=.33*(1.247*comp(1,index1))
xms(1,index1)=.62+(.14*comp(1,index1))
xms(2,index1)=xms(1,index1)
go to 240
C
c If here then InGaAs. The InGaAs is assumed to be surrounded by
c GaAs. The conduction band offset is assumed to be .4xd(Eg,h) and
c both the strain terms perturb the valence band alignment.
C
275 c11=12.11-(comp(2,index1)*3.569)
c12=5.48-(comp(2,index1)*.82)
a=-7.1+(comp(2,index1)*1.7)
b=-1.7-(comp(2,index1)*.1)
e=(comp(2,index1)*.40515)/(5.65325+(comp(2,index1)*.40515))
egnat=1.424-(comp(2,index1)*1.064)
egh=egnat+((-2.0*a*((c11-c12)/c11))+b*((c11+(2.0*c12))
+ /c11))*e

```

```

vi(index1)=-.60*(1.424-egh)
capa=6.98+(comp(2,index1)*12.72)
capb=4.5+(comp(2,index1)*12.8)
xms(1,index1)=1.0/(capa-capb)
xms(2,index1)=1.0/(capa+(.5*capb))
c
c Calculate the minimum of the potential.
c
240 if(vi(index1).lt.vsmall)vsmall=vi(index1)
c
250 continue
go to 400
c
c Generate the light hole potential and mass variation.
c
300 continue
do 350 index1=1,ntot
if(comp(2,index1).ne.0.0)go to 375
c
c If here then AlGaAs or GaAs
c
vi(index1)=.33*(1.247*comp(1,index1))
xms(1,index1)=.087+(.063*comp(1,index1))
xms(2,index1)=xms(1,index1)
go to 340
c
c If here then InGaAs. The InGaAs is assumed to be surrounded by
c GaAs. The conduction band offset is assumed to be .4xd(Eg,h) and
c both the strain terms perturb the valence band alignment.
c
375 c11=12.11-(comp(2,index1)*3.569)
c12=5.48-(comp(2,index1)*.82)
a=-7.1+(comp(2,index1)*1.7)
b=-1.7-(comp(2,index1)*.1)
e=(comp(2,index1)*.40515)/(5.65325+(comp(2,index1)*.40515))
egnat=1.424-(comp(2,index1)*1.064)
egh=egnat+((-2.0*a*((c11-c12)/c11))+(b*((c11+(2.0*c12))
+ /c11)))*e
vi(index1)=-(.60*(1.424-egh)+(2*b*((c11+(2.0*c12))/c11)
+ *e))
capa=6.98+(comp(2,index1)*12.72)
capb=4.5+(comp(2,index1)*12.8)
xms(1,index1)=1.0/(capa+capb)
xms(2,index1)=1.0/(capa-(.5*capb))
c
c Calculate the minimum of the potential.
c
340 if(vi(index1).lt.vsmall)vsmall=vi(index1)
c
350 continue
c
400 continue
c
c Offset the potential so that the lowest energy is zero.

```

```

c
c   if(vsmall.eq.0.0)go to 600
c   do 500 indexl=1,ntot
c       vi(indexl)=vi(indexl)-vsmall
500 continue
c
c 600 continue
c   return
c   end

c
c *****
c
c   subroutine psiall(iproty,istep,nbad,numlev)
c
c Subroutine to calculate the all the energy levels in any of the three
c possible bands.
c
c   vmax: maximum energy guess, assumed at last point in profile
c   vmin: minimum energy guess, set to the energy tolerance
c   istdyn: dynamic step variable initially set to istep
c   ierr2: flag to when there are no more levels in the well
c
c   dimension psi(4000),vi(4000),xms(2,4000),elev(3,50),flev(2,50)
c   dimension psist(6,4000),xymass(3,50),zmass(3,50)
c   common/constant/pi,hbar,xm0,bcon,dtemp
c   common/waves/vi,psi,xms,elev,dx,psist,xymass,zmass,flev
c   common/inputs/ntot,ietot,ihhtot,ilhtot,etol,itte,nlev
c   common/bugs/idebug
c
c Set up the main loop to calculate the energy levels.
c
c   nbad=0
c   anew=elev(iproty,1)
c   il=1
c   ir=ntot
c   ierr2=0
c   do 10 nlev=1,numlev
c       istdyn=istep
c       vmin=etol
c       vmax=vi(ntot)
c
c Solve for the next wavefunction and energy.
c
c       call numerov(vmax,vmin,istdyn,il,ir,ierr2,iproty,anew,nbad)
c
c Break out of loop if err2=1. This means that there are no more
c energy levels in the structure.
c
c       if(ierr2.eq.1)go to 20
c
c Store the energy in elev(n,m)
c
c       elev(iproty,nlev)=anew
c

```

```

c Nomalize the wavefuncton.
c
      call normal(ntot, xycms, zcms)
      xymass(iproty, nlev) = xycms
      zmass(iproty, nlev) = zcms
c
c Store the wavefunction if it is the n=1 or n=2 level.
c
      if (nlev.gt.2) go to 10
      do 30 index1=1, ntot
        psist(((iproty-1)*2)+(nlev), index1) = psi(index1)
30    continue
10  continue
20  continue
      return
      end
c
c *****
c
      subroutine numerov(vmax, vmin, istory, il, ir, ierr2, iproty, enew, nbad)
c
c Numerov method for the calculation of wavefunction and energy
c eigenvalues for an arbitrary level in an arbitrary potential.
c Last modified on 4-2-89 by Jenifer Lary.
c
      dimension psi(4000), vi(4000), xms(2, 4000), elev(3, 50), flev(2, 50)
      dimension psist(6, 4000), xymass(3, 50), zmass(3, 50)
      common/constant/pi, hbar, xm0, bcon, dtemp
      common/waves/vi, psi, xms, elev, dx, psist, xymass, zmass, flev
      common/inputs/ntot, ietot, ihhtot, ilhtot, etol, itte, nlev
      common/bugs/idebug
c
      enew = elev(iproty, nlev)
      emax = vmax
      emin = vmin
      if (nlev.gt.1) emin = elev(iproty, nlev-1)
      if (enew.lt.emin) enew = emin
      if (enew.gt.emax) enew = (emax+emin)/2.
      iterr = 0
c
      do 2 iter=1, itte
        de = 1.0
        if (idebug.eq.1) write(*, 35)
35      format(1x, 'nlev, iter, iterr, emin, enew, emax')
        if (idebug.eq.1)
+      write(*, 36) nlev, iter, iterr, emin, enew, emax
36      format(3I5, 3f10.7)
c
c Set up starting points from left and right
c
      nstep = 0
40      if (il.lt.1) il = 1
          if (ir.gt.ntot) ir = ntot
          call start(il, ir, ntot, enew, istory, istr, iwell)

```

```

        if(iwell.gt.1)go to 11
        if(nstep.gt.(2*ntot/istdyn+1))go to 515
        il=il-istdyn
        ir=ir+istdyn
        if(nstep.eq.0)istdyn=istdyn/2
        nstep=nstep+1
        if(idebug.eq.1)write(*,41)nstep,il,ir,istl,istr,istdyn
41    format(lx,'nstep,il,ir,istl,istr,istdyn ',6I5)
        go to 40
c
c If istl ne 1 and istr ne ntot,
c these are okay starting points.
c else, lower energy and try again.
c Get to 10 if having trouble finding a well for a guess at energy...
c lower energy and try again, as long as not through more than 10 itts
c
    11    continue
c
c Now figure wave from the right hand side...find first peak
c
        icount=0
        ijoin=0
c
105    continue
        icount=icount+1
        idir=-1
        call calcpai(ijoin,istr,istl,idir,psir,dpsir,
+    ierrl,sumr,izero,nizero,enew)
c
c If ierrl=0, no problems, continue on
c
        if(idebug.eq.1)
+    write(*,*)ierrl,idir,psir,dpsir,sumr,istl,ijoin,istr
        if(ierrl.eq.0)go to 4
c
c If ierrl=-1, couldn't find peak. Increase e and try again.
c
        if(ierrl.eq.-1)enew=(enew+emax)/2.
c
c If ierrl=-2, getting close to overflow. Move in further on right.
c
        if(ierrl.eq.-2)ir=istr-istdyn
        go to 2
c
c Get to 4 if everything hunky-dory with wave from right...
c
    4    idir=1
        call calcpai(ijoin,istr,istl,idir,psil,dpsil,
+    ierrl,suml,izero,nizero,enew)
        if(idebug.eq.1)
+    write(*,*)ierrl,idir,psil,dpsil,suml,istl,ijoin,istr
c
c If psil too close to 0 de will blow up...move joining point over
c If ierrl=-2, getting close to overflow. Move in further on left

```

```

c
    if(ierr1.eq.-2)il=istl+istdyn
    if(idebug.eq.1)write(*,*)'ijoin ',ijoin
    if((icount.le.3).and.(ierr1.eq.0).and.(abs(psil).lt.1))
+   ijoin=ijoin+1
    if((icount.le.3).and.(ierr1.eq.0).and.(abs(psil).lt.1))
+   go to 105
    if((icount.eq.1).and.(ierr1.eq.0).and.(abs(de-deold).lt.etol))
+   ijoin=ijoin+1
    if((icount.eq.1).and.(ierr1.eq.0).and.(abs(de-deold).lt.etol))
+   go to 105
c
c If ierr1=0, no problems, continue on
c
    if (ierr1.eq.0)go to 14
    go to 2
c
c Get to 14 if no prob with wave from left or right
c Check number of zero crossings.
c
    14  if(abs(enew-vmax).lt.(etol*100.))go to 505
c
c If position of last zero crossing too close to joining point
c
    if(izero.eq.(nlev-1))go to 15
    if((izero.gt.(nlev-1)).and.(enew.lt.emax))
+   emax=enew
    if((izero.lt.(nlev-1)).and.(enew.gt.emin))
+   emin=enew
    if(izero.gt.(nlev-1))enew=
+   (enew+emin)/2.
    if(izero.lt.(nlev-1))enew=
+   (enew+emax)/2.
    if(emin.eq.emax)emax=vmax
    go to 22
c
c Get to 15 if right number of zero crossings
c
    15  continue
c
c Now calculate energy error, etcetera
c
    iterr=iterr+1
c
c If first time had right number of zero crossings, iterr=1 now
c
    if(iterr.eq.1)deold=10.
    de=suml/(psil**2)+sumr/(psir**2)
    de=(dpsir/psir-dpsil/psil)/de
    de=abs(de)*(hbar**2)/(2.*dx*xm0*xms(1,ijoin))
    ratio=(dpsir/psir)/(dpsil/psil)
    if(idebug.eq.1)write(*,100)de,deold,ratio
100  format(1x,'de,deold,ratio ',3e12.4)
    if((ratio.lt.1.01).and.(ratio.gt.0.99).and.

```

```

+   (de.lt.etol))go to 700
    if(abs(de-deold).lt.etol)enew=enew+fway*etol
    if(iterr.eq.1)fway=1
    if(iterr.eq.1)enew=enew+fway*etol
    if(iterr.eq.1)deold=de
    if(iterr.eq.1)go to 2
    if(de.gt.deold)fway=-1.*fway
    if(de.gt.deold)de=deold*2.
    enew=enew+fway*de/2.
    if(enew.ge.emax)enew=
+   (enew-abs(fway*de/2.)+emax)/2.
    if(enew.le.emin)enew=
+   (enew+abs(fway*de/2.)+emin)/2.
    deold=de
    go to 2
22  iterr=0
2   continue
c
c Get to 700 if found a right energy level!
c
700 continue
    do 701 jk=1,istl-1
        psi(jk)=0.
701 continue
    do 702 jk=ntot,istr+1,-1
        psi(jk)=0.
702 continue
    do 703 jk=istl,ijoin+1
        psi(jk)=psi(jk)*psir/psil
703 continue
    suml=suml*psir/psil
    do 704 jk=istl,istr
        psi(jk)=psi(jk)/(suml+sumr)
704 continue
c
    if(iter.ge.itte)nbad=nbad+1
    1 continue
    go to 550
c
c Reach 515 if only one point in well
c
515 write(*,516)iwell,nstep
516 format(1x,'not enough pnts in well..iwell,nstep ',2I5)
    go to 550
c
c Reach 505 if level not contained
c
505 continue
    ierr2=2
    go to 550
c
c Reach 500 if cant find well....
c
500 continue

```

```

        write(*,*)'500 can not find well'
550  continue
        return
        end
C
C *****
C
        subroutine calcpsi(ij,istr,istl,idir,psij,dpsi,
+ ierrl,sum,izero,nizero,enew)
        dimension psi(4000),vi(4000),xms(2,4000),elev(3,50),flev(2,50)
        dimension psist(6,4000),xymass(3,50),zmass(3,50)
        common/constant/pi,hbar,xm0,bcon,dtemp
        common/waves/vi,psi,xms,elev,dx,psist,xymass,zmass,flev
        common/inputs/ntot,ietot,ihhtot,ilhtot,etol,itte,nlev
        common/bugs/idebug
C
        izero=0
        nizero=0
        dxsq=dx**2
        dummy=2.0*xm0/hbar**2
        ierrl=0
        ist=istr
        nj=ij
        iend=ij
        if(ij.eq.0)iend=istl
        if(idir.eq.1)ist=istl
        sum=0.0
C
C Set psi at +/-1.0, figure next as exponential
C If from left(idir=1) ifd is 1
C If from right ifd is 1 for nlev odd, -1 for nlev even
C
        ifd=1
        if(mod(nlev,2).ne.1)ifd=idir*ifd
        psi(ist-idir)=0.0
        psi(ist)=ifd*1.0
        sum=sum+dx*(psi(ist)**2)/2.0
        dummy2=(vi(ist)-enew)**0.5+
+ (vi(ist+idir)-enew)**0.5
        psi(ist+idir)=psi(ist)*
+ exp(dx*((dummy*xms(1,ist))**0.5)*dummy2/2.0)
        sum=sum+dx*((psi(ist+idir)**2)+
+ (psi(ist)**2))/2.0
C
C Now calculate psi till reach first peak if idir=-1 (from right)
C or till reach ij if idir=1 (from left)
C
        npeak=0
        peak=0.0
        do 1 j=(ist+idir),iend,idir
            njoin=j
            inext=j+idir
            ilast=j-idir
            fl=dummy*xms(1,inext)*(vi(inext)-enew)

```

```

f2=dummy*xms(1,j)*(vi(j)-enew)
f3=dummy*xms(1,ilast)*(vi(ilast)-enew)
psi(inext)=((dxsq*f3/12.0-1.0)*psi(ilast)+
+ (2.0+5.0*dxsq*f2/6.0)*psi(j))/(1.0-dxsq*f1/12.0)
c
c If psi is getting too big (magnitude) send back err=-2
c trying to avoid overflow.....
c
    if(abs(psi(inext)).ge.1.0e18)ierr1=-2
    if (ierr1.eq.-2)go to 100
    sum=sum+dx*((psi(inext)**2)+
+ (psi(j)**2))/2.
    dpsi=psi(inext)*(1.-dxsq/6.*f1)
+ -psi(ilast)*(1.-dxsq/6.*f3)
    dpsi=idir*dpsi*0.5
c
c Look for zero crossing if coming from the left
c
    if (idir.eq.-1)go to 4
    if((psi(inext).gt.0).and.(psi(j).le.0))
+ izero=izero+1
    if((psi(inext).le.0).and.(psi(j).gt.0))
+ izero=izero+1
    if((psi(inext).gt.0).and.(psi(j).le.0))
+ nizero=j
    if((psi(inext).le.0).and.(psi(j).gt.0))
+ nizero=j
    go to 1
c
c Look to see if it was a peak if coming from the right(idir=-1)
c
    4 continue
c
c If coming from right and looking for peak, nj is zero
c and if past peak make sure at least 5 points past it
c
    if(nj.ne.0)go to 1
c
c If magnitude positive from right
c
    if((ifd.eq.1).and.(dpsi.gt.0)
+ .and.(psi(j).gt.peak))peak=psi(j)
c
c Reset counter if new peak
c
    if((ifd.eq.1).and.(dpsi.gt.0)
+ .and.(psi(j).eq.peak))npeak=0
    if((ifd.eq.1).and.(dpsi.gt.0)
+ .and.(psi(j).lt.peak))npeak=npeak+1
c
c If magnitude is negative from right
c
    if((ifd.eq.-1).and.(dpsi.lt.0)
+ .and.(-1.*psi(j).gt.-1.*peak))peak=psi(j)

```

```

        if((ifd.eq.-1).and.(dpsi.lt.0)
+       .and.(psi(j).eq.peak))npeak=0
        if((ifd.eq.-1).and.(dpsi.lt.0)
+       .and.(-1.*psi(j).lt.-1.*peak))npeak=npeak+1
        if((idebug.eq.1).and.(npeak.ne.0))write(*,*)
+       'peak,npeak,j ',peak,npeak,j
        if(npeak.ge.5)go to 10
1 continue
c
c If here and idir=-1, couldn't find peak...send back ierr1=-1
c unless wasn't looking for one (nj ne 0)
c
        if(nj.ne.0)go to 10
        if(idir.eq.-1)ierr1=-1
        if(idir.eq.-1)go to 100
        psij=psi(ij)
        go to 100
c
c Get to 10 if idir=-1 and found peak
c
10 ij=j
        if((nj.ne.0).and.(idir.eq.-1))ij=j+1
        if(idir.eq.1)ij=iend
        psij=psi(ij)
100 return
        end
c
c*****
c
        subroutine start(il,ir,n,enew,istl,istr,iwell)
c
        dimension psi(4000),vi(4000),xms(2,4000),elev(3,50),flev(2,50)
        dimension psist(6,4000),xymass(3,50),zmass(3,50)
        common/waves/vi,psi,xms,elev,dx,psist,xymass,zmass,flev
        common/bugs/idebug
c
c Make sure at least 10 points in a row with v gt e on both sides
c il and ir are starting guesses of left and right
c istl and istr are values to start at that are okay (ten points)
c
        ilold=il
        irold=ir
        itm=25
        do 3 i=1,itm
c
c Find first point where v>e
        ist=1
        do 1 in=il,n
            if (vi(in).gt.enew)ist=in
            if (ist.ne.il) go to 2
1 continue
2 continue
        do 4 j=ist,ist+9
            if (vi(j).le.enew)il=j

```

```

        if (vi(j).le.enu)go to 3
4      continue
C
C If make it to here, have 10 in a row.....
C
        istl=ist
        go to 5
3      continue
C
C Now same thing from the right hand side
C
        5 continue
        do 13 i=1,itm
C
C Find first point where v>e
C
        ist=n
        do 11 in=ir,1,-1
            if (vi(in).gt.enu)ist=in
            if (ist.ne.ir) go to 12
11     continue
12     ncount=0
        do 14 j=ist,ist-9,-1
            if (vi(j).le.enu)ir=j
            if (vi(j).le.enu)go to 13
14     continue
C
C If make it to here, have 10 in a row.....
C
        istr=ist
        go to 15
13     continue
15     continue
        ic=0
        do 30 i=istl,istr
            if (vi(i).lt.enu)ic=ic+1
30     continue
        iwll=ic
        if(istl.ge.istr)iwll=0
        if(istl.ge.istr)il=ilold
        if(istl.ge.istr)ir=irold
        if((idebug.eq.1).and.(iwll.le.1))write(*,*)istl,istr,iwll
20     format(1x,'istl,istr,iwll ',3I5)
        return
        end
C
C *****
C
        subroutine normal(ntot,xcms,zcms)
C
        dimension psi(4000),vi(4000),xms(2,4000),elev(3,50),flev(2,50)
        dimension psist(6,4000),xymass(3,50),zmass(3,50)
        common/waves/vi,psi,xms,elev,dx,psist,xymass,zmass,flev
C

```

```

c Simpson approximation to calculate the normalized
c wavefunction. The lateral mass is also calculated.
c
  area=0.0
  do 10 index1=1,ntot-1
    y1=(abs(psi(index1)))**2
    y2=(abs(psi(index1+1)))**2
    area=area+(y1+y2)/2.0
  10 continue
c
  do 20 index1=1,ntot
    psi(index1)=psi(index1)/((dx*area)**0.5)
  20 continue
c
  cmsz=0.0
  cmsxy=0.0
  do 30 index1=2,ntot-1
    y1=(abs(psi(index1)))**2
    y2=(abs(psi(index1+1)))**2
    cmsz=cmsz+(dx*(y1+y2)/(2.0*xms(1,index1)))
    cmsxy=cmsxy+(dx*(y1+y2)/(2.0*xms(2,index1)))
  30 continue
c
  zcms=1.0/(cmsz)
  xycms=1.0/(cmsxy)
  return
  end
c
c *****
c
  subroutine ferlev(scstar,scstep,numsc,numlev,concin)
c
c Subroutine to calculate the quasi-Fermi energy levels for various
c sheet carrier densities.
c
  dimension psi(4000),vi(4000),xms(2,4000),elev(3,50),flev(2,50)
  dimension psist(6,4000),xymass(3,50),zmass(3,50)
  common/constant/pi,hbar,xm0,bcon,dtemp
  common/waves/vi,psi,xms,elev,dx,psist,xymass,zmass,flev
c
c Calculate the strain induced valence band splitting of the
c strained ternary from the input indium concentration.
c
  c11=12.11-(concin*3.569)
  c12=5.48-(concin*.82)
  a=-7.1+(concin*1.7)
  b=-1.7-(concin*.1)
  e=(concin*.40515)/(5.65325+(concin*.40515))
  eshr=(b*((c11+(2*c12))/c11))*e
c
c Calculate the quasi-Fermi level in the conduction band,
c
  do 560 index1=1,numsc

```

```

idir=-1
istat=0
dqferm=0.025
ferm=((bcon*dtemp)*log(exp(((scstar+((index1-1)*scstep))
+ *pi*hbar**2)/(bcon*dtemp*xymass(1,1)*xm0))-1.0)+elev(1,index1))
c
565 elect=0.0
do 570 index2=1,numlev
  elec1=((bcon*dtemp*xymass(1,index2)*xm0)/(pi*(hbar**2)))*
+   log(1+exp((ferm-elev(1,index2))/(bcon*dtemp)))
  elect=elect+elec1
570 continue
c
  if((elect.gt.((scstar+((index1-1)*scstep))-1.0e9)).and.
+   (elect.lt.((scstar+((index1-1)*scstep))+1.0e9)))go to 580
  if(elect.gt.((scstar+((index1-1)*scstep))))idnew=-1
  if(elect.lt.((scstar+((index1-1)*scstep))))idnew=1
  if(idnew.eq.1)istat=1
  if(istat.eq.0)ferm=ferm-dqferm/2.0
  if(idnew.eq.-1)ferm=ferm-dqferm/2.0
  if(idnew.eq.1)ferm=ferm+dqferm/2.0
  if(istat.eq.1)dqferm=dqferm/2.0
  idir=idnew
  go to 565
580 continue
  flev(1,index1)=ferm
560 continue
c
c Now calculate the quasi-Fermi level in the valence band.
c
do 660 index1=1,numsc
  idir=-1
  istat=0
  dqferm=0.025
  ferm=((bcon*dtemp)*log(exp(((scstar+((index1-1)*scstep))
+ *pi*hbar**2)/(bcon*dtemp*xymass(2,1)*xm0))-1.0)+elev(2,index1))
c
665 elect=0.0
do 670 index2=1,numlev
  elec1=((bcon*dtemp*xymass(2,index2)*xm0)/(pi*(hbar**2)))*
+   log(1+exp((ferm-elev(2,index2))/(bcon*dtemp)))
  elec2=((bcon*dtemp*xymass(3,index2)*xm0)/(pi*(hbar**2)))*
+   log(1+exp((ferm+(2.0*eshr)-elev(3,index2))/(bcon*dtemp)))
  elect=elect+elec1+elec2
670 continue
c
  if((elect.gt.((scstar+((index1-1)*scstep))-1e9)).and.
+   (elect.lt.((scstar+((index1-1)*scstep))+1e9)))go to 680
  if(elect.gt.((scstar+((index1-1)*scstep))))idnew=-1
  if(elect.lt.((scstar+((index1-1)*scstep))))idnew=1
  if(idnew.eq.1)istat=1
  if(istat.eq.0)ferm=ferm-dqferm/2
  if(idnew.eq.-1)ferm=ferm-dqferm/2
  if(idnew.eq.1)ferm=ferm+dqferm/2

```

```

        if(istat.eq.1)dqferm=dqferm/2
        idir=idnew
        go to 665
680    continue
        flev(2,index1)=ferm
660    continue
c
c 900    return
        end
c
c *****
c
        subroutine gsp(enstar,enstep,numen,concin,scstar,scstep,numsc,
+ numlev,shift)
c
c Subroutine to calculate the gain spectrum of the structure from the
c quasi-Fermi level and energy level positions.
c
        dimension psi(4000),vi(4000),xms(2,4000),elev(3,50),flev(2,50)
        dimension psist(6,4000),xymass(3,50),zmass(3,50)
        dimension gain(10,1000)
        common/constant/pi,hbar,xm0,bcon,dtemp
        common/waves/vi,psi,xms,elev,dx,psist,xymass,zmass,flev
        common/inputs/ntot,ietot,ihhtot,ilhtot,etol,itte,nlev
        common/bugs/idebug
        common/spec/gain
        real msq,ksq,leff
        character shift*1
c
c Calculate the band properties of the strained ternary from the
c input indium concentration.
c
        c11=12.11-(concin*3.569)
        c12=5.48-(concin*.82)
        a=-7.1+(concin*1.7)
        b=-1.7-(concin*.1)
        e=(concin*.40515)/(5.65325+(concin*.40515))
        egnat=1.424-(concin*1.064)
        ehyd=(-2.0*a*((c11-c12)/c11))*e
        eshr=(b*((c11+(2*c12))/c11))*e
        egh=egnat+ehyd+eshr
        egl=egnat+ehyd-eshr
        delta=.340+(concin*.03)
        elmass=.067-(concin*.044)
c
c Calculate the matrix element squared for the transition
c
        msq=(egnat*(egnat+delta))/(4.0*elmass*(egnat+((2.0/3.0)*delta)))
c
c Set-up the loop to iterate through the various valence bands.
c
        egap=egh
        do 10 index3=2,3
c

```

```

c Check for type I versus type II light hole structure and reference
c the light hole band accordingly.
c
    if(index3.eq.2)go to 20
    if((egl+(.4*(1.424-egh))).lt.1.424)egap=egl
    if((egl+(.4*(1.424-egh))).ge.1.424)egap=1.424-(.4*(1.424-egh))
c
c Set-up the loop to iterate through the various energy levels.
c
    20  write(*,*)'egap: ',egap
c
    do 25 index4=1,numlev-1
        temp1=egap+elev(1,index4)+elev(index3,index4)
        temp2=enstar+((numen-1)*enstep)
        if(temp1.gt.temp2)go to 25
c
c The (delta n)=0 selection rule is assumed.
c
c Calculate the effective well width from the transition energies.
c
    temp1=sqrt((2.0*zmass(1,(index4+1))*xm0*
+     elev(1,(index4+1)))/(hbar**2))
    if(index4.eq.1)temp2=0.0
    if(index4.eq.1)go to 36
    temp2=sqrt((2.0*zmass(1,(index4-1))*xm0*
+     elev(1,(index4-1)))/(hbar**2))
    36  leff=(2.0*pi)/(temp1-temp2)
        write(*,*)'effective well width: ',leff
c
c Set-up the loop to iterate through the various carrier densities.
c
    do 50 index1=1,numsc
c
c Calculate the band renormalization offset to the spectra.
c
    off=((3.2e-8)*(((scstar+((index1-1)*scstep))/leff)
+     **(1.0/3.0)))/enstep
    ioff=int(off)
    if(shift.eq.'n')ioff=0
c
c Calculate the reduced mass for the transition.
c
    rmass=(xymass(1,index4)*xymass(index3,index4))/
+     (xymass(1,index4)+xymass(index3,index4))
c
c Set-up the loop in energy over which the gain spectrum will be
c calculated.
c
    do 100 index2=1,(numen+ioff)
c
    etran=enstar+((index2-1)*enstep)
+     if(etran.lt.(egap+elev(1,index4)+
        elev(index3,index4)))go to 100
c

```

```

c Calculate the k associated with a vertical transition at the
c etran energy.
c
      ksq=2.0*rmass*xm0*(etran-(egap+elev(1,index4)+
+      elev(index3,index4)))/(hbar**2)
c
c Calculate the energy up the 2 dimensional bands.
c
      ec=((hbar**2)*ksq)/(2.0*xymass(1,index4)*xm0)
      ev=((hbar**2)*ksq)/(2.0*xymass(index3,index4)*xm0)
c
c Calculate the Fermi functions for the specific transition energy.
c
      fc=1.0/(1.0+(exp((elev(1,index4)+ec-flev(1,index1))/
+      (bcon*dtemp))))
c
      if(index3.eq.3)go to 40
      fv=1.0/(1.0+(exp((-1.0*(elev(index3,index4)+ev-
+      flev(2,index1)))/(bcon*dtemp))))
      go to 44
c
40      fv=1.0/(1.0+(exp((-1.0*(elev(index3,index4)-(2.0*eshr)
+      +ev-flev(2,index1)))/(bcon*dtemp))))
c
c Calculate the anisotropy associated with the dipole average in K
c for TE modes.
c
44      temp1=sqrt((2.0*xymass(1,index4)*xm0*ec)/(hbar**2))
      temp2=sqrt((2.0*zmass(1,index4)*xm0*elev(1,index4))/
+      (hbar**2))
      theta=atan(temp1/temp2)
      if(index3.eq.3)go to 46
      an=(.5)*(1.0+((cos(theta))**2))
      go to 48
c
46      an=(1.0/6.0)*((4.0*sin(theta)*cos(theta))+5.0-(3.0*
+      ((cos(theta))**2)))
c
c Calculate the gain at the specific transition energy.
c
48      if((index2-ioff).lt.1)go to 100
      gain(index1,(index2-ioff))=gain(index1,(index2-ioff))+
+      (((2.6184e-2)*msq)/(leff*etran))*rmass*an*(fc-fv)
c
100      continue
c
50      continue
c
25      continue
c
10      continue
c
      return
      end

```

```

C
C *****
C
C      subroutine conv(etran,enstar,enstep,numen,numsc,tsc)
C
C Subroutine to smooth the gain spectrum with the lorentzian function
C defined by tsc.
C
C      dimension gain(10,1000)
C      dimension smogn(1000)
C      common/constant/pi,hbar, xm0,bcon,dtemp
C      common/spec/gain
C      real lor1,lor2
C
C Set-up the loop through the different carrier densities.
C
C      do 25 index1=1,numsc
C
C Zero the smoothed spectra array.
C
C      do 50 index2=1,1000
C          smogn(index2)=0.0
C      50 continue
C
C Set-up the loop in energy over which the gain spectrum will be
C convoluted.
C
C      do 75 index2=1,numen
C          etran=enstar+((index2-1)*enstep)
C          engl=enstar
C          lor1=((6.5822e-4)/tsc)/(((4.3325e-7)/(tsc**2))+
C      + (engl-etran)**2)
C
C          do 100 index3=1,numen-1
C              eng2=engl+enstep
C
C Calculate the lorentzian on the right side of the area element.
C
C          lor2=((6.5822e-4)/tsc)/(((4.3325e-7)/(tsc**2))+
C      + (eng2-etran)**2)
C
C Calculate the smoothed gain adding into the transition energy.
C
C          smogn(index2)=smogn(index2)+(.5/pi)*((lor1*
C      + gain(index1,index3))+lor2*gain(index1,(index3+1))))
C      + *enstep
C
C The right side of the next area element = the left side of the
C current.
C
C          engl=eng2
C          lor1=lor2
C
C      100 continue

```

```
c
  75  continue
c
c Store the smoothed spectra back in the original array.
c
      do 125 index2=1,numen
        gain(index1,index2)=smogn(index2)
125  continue
c
      25 continue
c
      return
      end
```